Generation and characterization of shaped femtosecond pulses and their application in spatio-temporal control of speckle pattern

Ayhan Tajalli

THÈSE

En vue de l'obtention du

DOCTORAT DE L'UNIVERSITÉ DE TOULOUSE

Délivré par *l'Université Toulouse III - Paul Sabatier*
Discipline ou spécialité : *Physique*

Présentée et soutenue par *Ayhan Tajalli*
Le *19 Octobre 2012*

Titre : *Génération et caractérisation d'impulsions façonnées - Application au contrôle spatio-temporel de la lumière diffusée*

JURY
Véronique Boutou (rapporteur)
Sophie Brasselet (rapporteur)
Daniel Braun
Béatrice Chatel (Directrice de thèse)
Patrick Georges

Ecole doctorale : *Sciences de la Matière (SDM)*
Unité de recherche : *LCAR-IRSAMC UMR5589*
Directeur(s) de Thèse : *Béatrice Chatel*
Rapporteurs : *Véronique Boutou, Sophie Brasselet*

Acknowledgments

I would like to express my heartfelt gratitude to all the people who have contributed to the culmination of this work, with their encouragement and support.
My deepest regard to Dr. Béatrice Chatel for the opportunity she provided in accommodating me in her workgroup and for her meticulous supervision, advice, and guidance from the very early stage of this research. It was a pleasure and honor to work with her and I am indebted to her more than she perceives.
My gratitude also extends to Dr. David McCabe and Dr. Sébastien Weber who was former PhD student of the FemtoControl group. David has the largest contribution to the experimental knowhow that I acquired over the course of my PhD studies. I am indebted to him for his valuable advice in scientific discussions, MATLAB programming and furthermore, for his precious time to read this manuscript and to give his critical comments about it. I am indebted to Sébastien for being so welcoming upon my arrival and spending his valuable time teaching me how to work with DAZZLER.
I would acknowledge the support that the members of jury committee have provided, spending their valuable time for evaluation. Special thanks go to Dr. Véronique Boutou and Dr. Sophie Braselet for carefully reading of manuscript and for their insightful comments. Prof. Daniel Braun and Dr. Patrick Georges have been very kind in their acceptance to be in the jury committee.
I would like to thank Prof. Ian Walmsley and Dane Austin, our collaborators from Oxford University, for their constant contribution and assistance in the projects during my thesis. Dane's visits were always accompanied with enormous progress in our experimental setups which was due to his particular skill in handling precisely the delicate metrology experiments. Many thanks to Dr. Sylvain Gigan, our other collaborator from Institut Langevin, for his large contribution in the speckle experiments. Without his scattering samples and his expertise in scattering process this thesis would not have been possible. I am also very grateful to our collaborators Dr. Brian Smith and his PhD student Merlin Cooper from Oxford University for allowing

us to use their lab in order to study the behavior of the entangled photons in the multiply scattering medium. Thanks for being a great host and making my stay in Oxford so enjoying and unforgettable.
Many thanks go to Elsa Baynard et Stéphane Faure for their technical support and instantaneous help during experiments.
I would like to acknowledge the cooperation of Dr. Benoit Chalopin, member of our group and also later my office-mate, for his helps and comments about writing this dissertation. Because of him our office were completely renewed after few decades.
I would also like to thank Dr. Valérie Blanchet, for always having time for answering my abrupt questions and solving the most of the occurring problems in the lab.
I am also thankful for all other members of LCAR: Marie-France Rolland, Agnès Georges, Sylvie Boukhari and Christine Soucasse, our administration staff, for taking on the burden of frustrating administrative work; Laurent Polizzi, Gerard Trenec, Roland Lagarrigue and Emmanuelle Kierbel, our technical staff, for their technical support; Prof. Aziz Bouchene, Prof. Chirstoph Meier, Prof. Bertrand Gigard, Prof. Jacques Vigué and other members of LCAR for being kind to me at all the times.
My gratitude must extend to Catherine Stasiulis, responsible of Service des Relations Internationales, who has known the answer to every question I have ever asked her regarding visa and my staying issues in France. She was one of the first friendly faces to greet me when I began this doctoral program and has always been a tremendous help in every circumstance. I could not have completed all the required administrative paperwork without her countless help.

I wish to express my appreciation and gratitude to my friends for their friendship, support and for providing me with numerous moments of joy and regale.
To Nicolas Thiré, my office-mate from Brittany, I would especially like to give my heartfelt thanks for being a kind and warm friend. He and his partner Amélie have helped me a lot to learn about beautiful and rich French culture and language, especially the finer and intricate details French people are known for. Thanks for being patient with me and my poor French. I should admit that my proficiency in French has been declined after your departure to Canada.
To David Staedter, my German colleague and next-door neighbor both in the lab and office, I express my most sincere gratitude for being such a nice and perfect friend with a warm and friendly heart. He was always eager to lend me a hand and the best one that one can count on. Those discussions in the coffee breaks were really relieving.

I deeply appreciate everything he has done for me and hope to have the chance of working alongside him again. One regret - he have never taught me his recipes!
To Arunangshu Denath, a friend from India (and my office-mate of early PhD days!), I must express my appreciation not only for the nice long discussions we had about everything during the course of stroll around Toulouse but also for being a constant source of encouragement. He has helped me a lot with writing of official emails. Arun, thank you very much!
For each of the following people, I give thank for their friendship, expressed in various ways, during the course of my life as well as during the work for this dissertation: Wesley, Mina, Marina, Caroline, Stefan, Marie, Charlotte, Cyril, Alberto, Yasir and Anil. Hope these friendships will continue to evolve.
Many thanks and appreciation to Omid for his confirmed friendship and support throughout all these years and sticking with me through my many annoyances.

I would like to thank my family for their support. My parents, as always have extended their unwavering support and prayers, unconditionally. My father is the person who introduced me to the world of science and the fascination still continues. My mother is the one who always encouraged me to develop my intellect. Words will fall short to express my feelings and gratitude to them. I have deepest regard and sinceremost love for them, for teaching me the art of weathering through the dark hours of life with patient and courage.
My brother Payman have always been close to me, making me feel safer. He is the first person taught me the pleasure of performing 'low-cost' and 'non-safe' scientific experiments at home with the inevitable results of burning, damaging and destroying some property.
I would also like to thank my parents-in-law for all their love and encouragements. I will never forget the trips that we had together.
Last but not the least, I would like to acknowledge the most important person in my life - my wife Neda. She has been a constant source of strength and inspiration standing by my side throughout this PhD tenure, making every single moment worthy of living. Without her, I would not have had the courage to embark on this journey in the first place.

Contents

Introduction

The main developments which led to our understanding of light and of optical phenomena, occurred a long time ago. Before the discovery of laser, it seemed unlikely that any dramatic changes would occur and in some senses the field became an unfashionable one. The arrival of the laser marked a new beginning, the extent of which can be judged from the enormous effort which was developed to its study. The publishing of over 5000 papers within the first ten years after its discovery was a proof to its revolutionary effect on the fundamental science. Apart from their applications in fundamental research, lasers are nowadays present everywhere in our life and it seems that the growth of their applications will never stop. What makes the laser source so unique is its coherence, directionality and monochromacity (or alternatively short duration).

The short duration (equivalently broad spectral bandwidth) which is the main property of femtosecond lasers has opened up very important new frontiers in both basic research and for applications. For example, due to their ultrashort duration, femtosecond laser is considered as the main candidate to study the electronic dynamics of the molecules by using of so called pump-probe techniques [1]. Furthermore, the mentioned short duration property resulted in application of the femtosecond sources in coherent control experiments [2]. Their broad spectral bandwidth is also highly applicable in high precision optical frequency metrology which brought the Nobel prize in physics for J. L. Hall and T.W. Hansch [3–7]. Concentration of modest laser energy in time (femtosecond) and space (micrometer) delivers extreme peak intensities that also caused a revolution in light-matter interactions. However, one challenging task is the characterization of femtosecond pulses. This is because their measurement requires electronic devices that are considerably faster than their duration while the existing detectors have at best time response of few picoseconds. Since there is no shorter event available to measure ultrashort pulses, the shortest possible event that can be used is the pulse itself. Along with the advances in generation of femtosecond

sources, ultrafast metrology witnessed tremendous improvements in recent years. The examples include SPIDER [8] and FROG [9] techniques which are now commercially available in various spectral domains.
Typically, all pulse characterization methods reconstruct the overall temporal electric field or intensity of the pulses (averaged over spatial profile) without providing any information about their spatial characteristics. The reconstructed electric field is valid only in the absence of space-time couplings or in other words, when temporal properties of the pulse is same for every spatial position along the beam. When space-time coupling effects are present, each spatial position along the pulse wavefront will have its own specific temporal properties. These couplings, which are due to the broad spectral bandwidth of the ultrashort pulses, are introduced from their propagation in optical elements such as gratings, prisms and air. These couplings often blur temporal resolution, reduce intensity and cause other problems. Nevertheless, space time couplings can be exploited for specific purposes such as increasing the spectral bandwidth of the nonlinear optical conversions [10]. Therefore, in order to properly understand and control them, a systematic studying and characterization of couplings and their sources is required. This is done either by extension of conventional temporal characterization techniques to the spatial domain or invention of novel independent instruments. Among all developed techniques for characterization of such couplings e.g. SEA SPIDER and SEA-TADPOLE, we have used Fourier Transform Spatio-Spectral Interferometry (FTSSI) due to its numerous advantages that will be detailed in this manuscript [11].

On a femtosecond time scale, many interactions depend on the particular temporal shape of the waveform being applied. For many applications such as coherent control of quantum mechanical processes [12–15], pulse compression [16], multidimensional nonlinear microscopy [17], optical communications [18] and factorization of numbers [19–21] it is desirable and necessary to modify the pulses from the source in a well-defined manner. While shaping of nanosecond and picosecond pulses can be achieved by electronically driven pulse shapers, such as electro-optic modulators, all-optical techniques have to be applied for femtosecond pulse shaping. Pulse shapers are also main sources of space time couplings. Therefore, studying their relevant couplings are highly desired. Extensive studies of the pulse shapers based on 4f-line configuration are undertaken [11, 22–26]. However, no complete studying of Acousto-Optic Programmable Dispersive Filter pulse shapers (AOPDF), which are highly desired in

the community mainly because of their wide range of tunablity, has been reported. One direction of our studies is the full spatio-temporal characterization of the UV-AOPDF pulse shaper by means of FTSSI technique.

As mentioned, it is the ultrashort duration and the spatial shape of the femtosecond pulses that make them so useful for different applications. Unfortunately, implementing such applications in biomedical samples is elusive due to their inhomogeneous refractive index. In other words, they strongly distort the spatial and temporal form of the incident pulse as it propagates through the sample and hence snatch those properties of the pulses on which their applications are based on. Different techniques has been developed to correct the spatial distortions of the continuous-wave lasers both in thin [27, 28] and thick [29] scattering media.
In the pulsed regime, the control or in other word the correction of the spatial and temporal shape is already done in acoustic and MHz regime using time reversal experiments [30–33]. However, because of the difficulty of measuring the complex electric field at optical frequencies, the task of spatio-temporal distortion correction remained elusive until our work in which we measured and consequently performed time reversal experiments in the appropriate optical frequency regime [34, 35]. Since the scattering medium couples the spatial and temporal domains, we obtained both spatial and temporal focusing only by shaping the spectral phase of the input pulses. This is the subject of the third chapter of the manuscript.

This manuscript is organized as follows:

-First chapter (Experimental devices) presents briefly the laser source and the experimental devices including femtosecond pulse measurement and shaping techniques that I have frequently used during my PhD period in LCAR.

-Second chapter (space-time coupling) is devoted to complete characterization of the spacetime coupling effects produced by the UV-AOPDF pulse shaper. First it starts with a mathematical description of the space-time couplings. Then it reviews the present state of art in space-time characterization techniques. Finally, it presents the experimental results concerning the full spatio-temporal characterization of the UV-AOPDF pulse shaper and the physical origin of the produced space-time couplings.

-Third chapter is about spatio-temporal characterization and controlling of the femtosecond pulses transmitted through a multiply scattering medium. Therefore,

first it presents the current state of control of the spatio-temporal speckles. Then, it presents the analytical and numerical description of such control via spectral shaping of the input pulses. Then, it describes the experimental setup that we have used to study and control the transmitted light. Finally, it shows the experimental results including spatio-temporal characterization of the transmitted pulses and more importantly, spatio-temporal control of such transmitted pulses behind the scattering medium.

Chapter 1

Experimental devices

This chapter presents briefly the laser source and experimental techniques and tools that I have regularly used during my PhD period in LCAR. It is organized as follows: section 1.1 introduces the general characteristics of our laser source. Section 1.2 presents the mathematical description of the optical pulses which is used throughout this thesis. Section 1.3 gives an overview about the techniques of generation of ultrashort pulses in Ultraviolet (UV) region. In addition, it describes our experimental configuration that we have used for the generation of ultrashort UV pulses. Section 1.4 is an overview of the conventional ultrashort pulse shaping techniques–specifically those we have used in our lab. Finally, pulse measurement methods that have applied in our studies are described in section 1.5.

1.1 Laser source

The frequent laser source that has been used during my thesis is a commercial Ti-Sapphire oscillator (*FEMTOLASERS Produktions*). It is pumped by a 4.4 W continuous-wave (CW) laser operating at 579 nm and delivers pulse sequences with duration of 20 fs at Full Width at Half Maximum (FWHM) with repetition rate of 76 MHz. It is operating at 800 nm with spectral bandwidth of 70 nm at FWHM [see Fig. 1.1(a)]. The output pulse energy is about 5.2 nJ/pulse.
A Chirped Pulse Amplification system (CPA) that is the most common method of pulse amplification is added to our oscillator in order to increase the single pulse energy [36, 37]. Our CPA system which is made by *Amplitude technologies* consists of three main parts: pulse stretching, two steps of amplification and finally pulse compression.

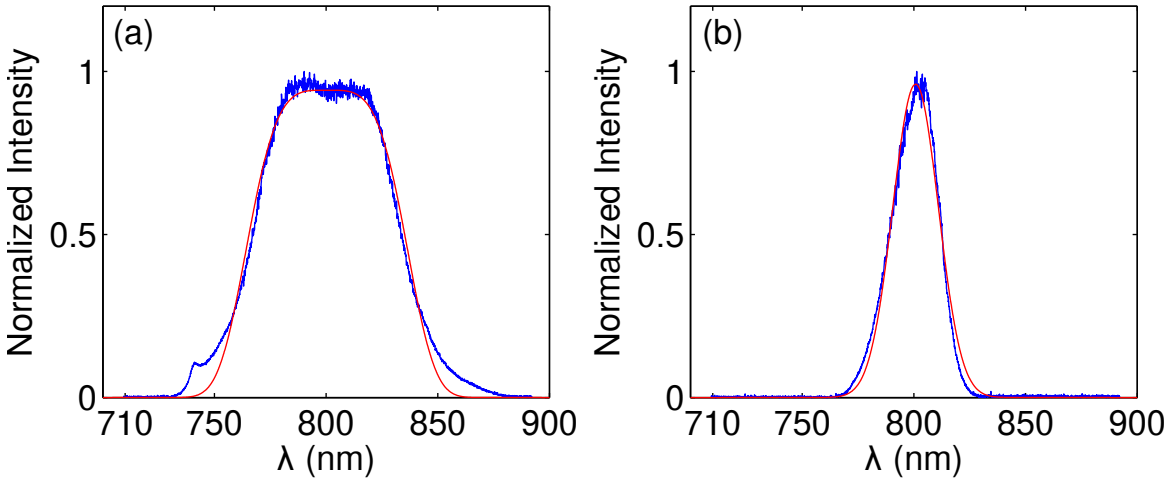

Figure 1.1: *Spectral intensities of femtosecond oscillator and laser chain. (a) Solid blue line is the spectral intensity of the femtosecond laser oscillator measured by a calibrated spectrometer. Solid red line is the Super-Gaussian fit with central wavelength of 800.3 nm and bandwidth of 71 nm at FWHM. (b) Solid blue line is the measured spectral intensity of the laser chain. Solid red line is the Gaussian fit with central wavelength of 800.7 nm and bandwidth of 24 nm at FWHM.*

In the following, I describe briefly the principles of the chirped pulse amplification and the characteristics of the beam at the output of each mentioned step [see Fig. 1.2 for the laser chain scheme and Tab. 1.1 for the beam characteristics at the output of each step]. The output of the laser oscillator is injected into a pulse stretcher

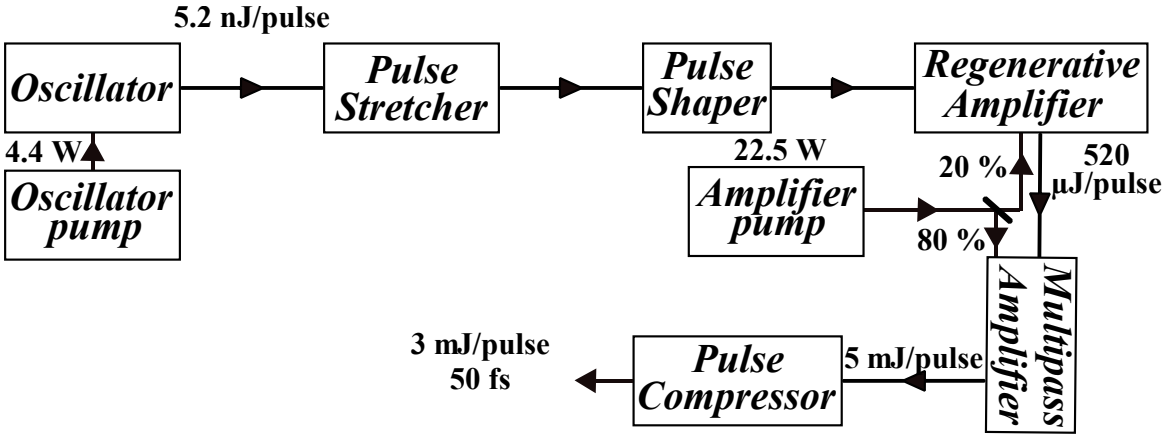

Figure 1.2: *Scheme of the laser chain with characteristics of the output beam at each step. The laser chain consists of femtosecond Ti-sapphire oscillator and Chirped Pulse Amplification (CPA) system. CPA system is made of a pulse stretcher, two sequent stages of amplifiers and a pulse compressor. Pulse shaper placed after pulse stretcher compensates the higher order residual phase produced by the laser chain optics.*

where the pulse duration is broadened by factor of 10^3-10^4 via adding a positive quadratic phase [38, 39]. The duration of the stretched pulse is determined by the need to avoid damage to the optics and to avoid nonlinear distortions of the spatial and temporal profile of the beam. At the output of the stretcher a pulse shaper that is called Acousto-Optic Programmable Dispersive Filter (AOPDF) [40] is embedded. It eliminates the higher order residual phases that are produced by optics of the laser chain. In the next step, pulses are amplified by a low-gain regenerative amplifier [41] to 520 μJ/pulse where the repetition rate falls to 1 kHz. Since the regenerative amplifier possesses a cavity, a low-gain configuration is typically used to prevent the generation of Amplified Spontaneous Emission (ASE). Pulses are then additionally amplified to 5 mJ/pulse by a high-gain multipass amplifier [42]. Finally, pulse compression is obtained by a pair of gratings by introducing the opposite phase of the pulse stretcher [43]. The output beam is therefore a train of almost Fourier limited pulses with duration of 50 fs and with energy of 3 mJ/pulse [see Fig. 1.3]. Figure 1.1(b) shows the spectral intensity at the output of the pulse compressor that

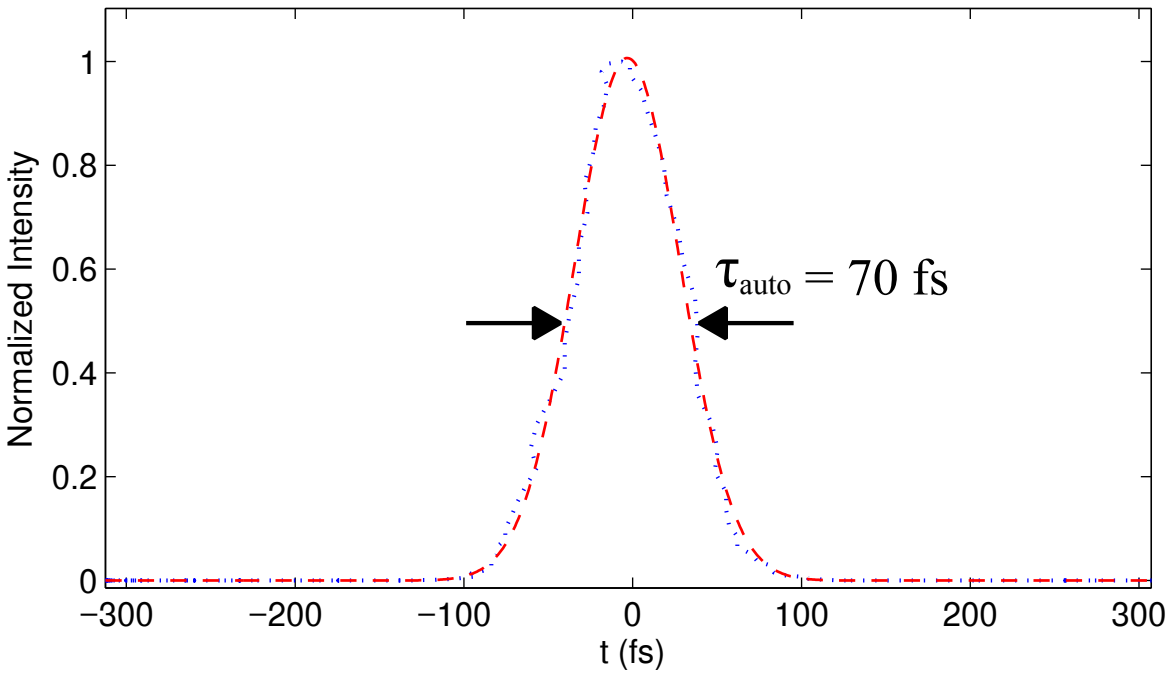

Figure 1.3: *Typical intensity autocorrelation of femtosecond pulses delivered by laser chain. Dotted blue line is the temporal intensity autocorrelation of the laser chain. Dashed red line is the Gaussian fit with bandwidth of 70 fs at FWHM which infers pulse duration of 50 fs.*

has a Gaussian profile centered at 800.7 nm with bandwidth of 24 nm at FWHM.

Properties	Oscillator	Regen	Multi-pass	Output
Average power	400 mW	520 mW	5 W	3 W
Repetition rate	76 MHz	1 kHz	1 kHz	1 kHz
Pulse energy	5.2 nJ	520 μJ	5 mJ	3 mJ
Central wavelength	800 nm	800 $\pm$ 10 nm	800 $\pm$ 10 nm	800 $\pm$ 10 nm
Spectral bandwidth	$\sim$ 70 nm	$\sim$ 25 nm	$\sim$ 25 nm	$\sim$ 25 nm

Table 1.1: *Characteristic of the femtosecond laser chain of LCAR*

The increased pulse duration compared with the output of the oscillator is due to the spectrum narrowing during the nonlinear amplification process. Additionally we have also used a home-made Ti-Sapphire oscillator without amplification system in our studies [44]. It provides 100 fs pulses centered at 800 nm with spectral bandwidth of 10 nm at FWHM and repetition rate of 76 MHz.

1.2 Mathematical description of ultrashort optical pulses

Ultrashort pulses can be characterized by measuring their electric field. In other words, the information that we can get from an experiment where the ultrashort pulses are used is directly dependent to the amount of knowledge that we can have over pulse electric field. This requires a proper mathematical description of the ultrashort pulses based on their electric field. In the following, I outline the mathematical notations of the optical pulses which will be used throughout this thesis. Such description would also provide a more intuitive understanding of the behavior of ultrashort pulses.
The optical pulse is characterized by its real valued electric field $\mathcal{E}(x, y, t)$, where x and y are its spatial dependences along its transverse plane while t is its temporal dependence. If the temporal characteristics of the pulse are independent of the spatial ones, the electric field can be written as a product of temporal and spatial factors

$$\mathcal{E}(x, y, t) = \mathcal{E}(x, y)\mathcal{E}(t) \tag{1.1}$$

and hence each factor can be derived independently from the wave equations. First, I present the temporal factor $\mathcal{E}(t)$.

Ultrashort pulses in temporal (spectral) domain
It is generally more convenient to use complex (analytic) representation of the electric

field. The real electric field $\mathcal{E}(t)$ is related to analytic electric field $\tilde{E}(t)$ through

$$\mathcal{E}(t) = \tilde{E}(t) + \tilde{E}^*(t) \tag{1.2}$$

where * is the sign of complex conjugation. The electric field of a typical pulse in the temporal domain with a linear polarization can be written

$$\tilde{E}(t) = |\tilde{E}(t)|e^{i\phi(t)}e^{-i\omega_0 t} \tag{1.3}$$

where $|\tilde{E}(t)|$ is the temporal amplitude, $\phi(t)$ is the temporal phase and ω_0 is the central frequency of the pulse. The intensity of the pulse is given by the temporal amplitude $I(t) \propto |\tilde{E}(t)|^2$. $\phi(t)$ can be written as a Taylor expansion at the arrival time of the pulse peak t_0

$$\phi(t) = \phi(t_0) + \frac{\partial\phi}{\partial t}|_{t_0}(t - t_0) + \frac{1}{2}\frac{\partial^2\phi}{\partial t^2}|_{t_0}(t - t_0)^2 + ... \tag{1.4}$$

where the zeroth order $\phi(t_0)$ is the carrier envelope offset (constant) manifesting the phase of the field oscillation at the peak of the pulse. This parameter plays an important role in few cycle pulses. However, in our case, since we are dealing with several cycle pulses, it can be ignored. The first derivative establishes the instantaneous frequency. More precisely, it shows the evolution of the instantaneous frequency as a function of time (temporal chirp). The second derivative shows the sign and magnitude of the temporal chirp.
The optical pulse may be also represented in spectral domain which is obtained from Fourier transforming of the electric field along temporal domain $\tilde{\mathcal{E}}(\omega) = FT[\mathcal{E}(t)]$. We are interested in spectral counterpart of $\tilde{E}(t)$ which is calculated by setting to zero the negative frequencies of the $\tilde{\mathcal{E}}(\omega)$. The relation between the complex value and positive frequency electric field is hence:

$$\tilde{\mathcal{E}}(\omega) = \tilde{E}(\omega) + \tilde{E}^*(-\omega). \tag{1.5}$$

The analytical spectral electric field of the pulse can be also written in polar notation

$$\tilde{E}(\omega) = |\tilde{E}(\omega)|e^{i\phi(\omega)} \tag{1.6}$$

where $|\tilde{E}(\omega)|$ is the spectral amplitude and $\phi(\omega)$ is the spectral phase. The spectral intensity can be calculated from the amplitude $I(\omega) \propto |\tilde{E}(\omega)|^2$ from which the spectral

bandwidth of the pulse can be extracted. The spectral phase can be also written as Taylor expansion at the central carrier frequency ω_0:

$$\phi(\omega) = \phi(\omega_0) + \frac{\partial\phi}{\partial\omega}|_{\omega_0}(\omega - \omega_0) + \frac{1}{2}\frac{\partial^2\phi}{\partial\omega^2}|_{\omega_0}(\omega - \omega_0)^2 + ... \tag{1.7}$$

where the zeroth order phase (absolute phase) $\phi(\omega_0)$ affects the carrier envelope offset with out modifying the temporal intensity. The first derivative of the spectral phase $\phi^{(1)} = \frac{\partial\phi}{\partial\omega}$ establishes the arrival time of a particular frequency (spectral chirp or group delay). The second derivative shows the value and the sign of the spectral chirp. If $\phi^{(2)}$ and the higher order terms are zero, the pulse is called Fourier limited pulse. It means that for the given spectral bandwidth $\Delta\omega$ pulse has the shortest possible duration at FWHM.

Spatial dimension

The spatial dependence of the pulse can be derived from the wave equation when it is independent of the temporal profile. The simplest solution for the spatial function is assuming a pulse with a constant intensity across the beam and infinitely large beam diameter (plane wave). A more general solution yields an optical pulse with a Gaussian spatial profile which is a solution to Maxwell wave equation under the paraxial approximation condition and when the beam propagates along the z direction and has a linear polarization.

Some useful definitions which are going to be used in the manuscript are the pulse spectrum

$$S(w) = \int_{-\infty}^{\infty} I(x, y, \omega)dxdy \tag{1.8}$$

and the pulse power in temporal domain

$$P(t) = \int_{-\infty}^{\infty} I(x, y, t)dxdy \tag{1.9}$$

and the pulse energy

$$F(x, y) = \int_{-\infty}^{\infty} I(x, y, t)dt. \tag{1.10}$$

1.3 Generation of ultrashort UV pulses

1.3.1 State of the art

The electronic absorption of most of the organic molecules lays in ultraviolet (UV) spectral region. Therefore, in order to perform ultrafast spectroscopy or coherent control experiments in such molecules, generation of ultrafast pulses in this spectral region is strongly desired. Unfortunately, this task is rather challenging because only a few exotic materials exist that can be used for light amplification in this spectral range. Moreover, the additional problem is that their bandwidth does not support pulses shorter than 100 fs [45]. Therefore, the usual approach has been to extend the operation range of standard near-IR Ti:sapphire laser systems to the UV-DUV spectral range by applying frequency conversion techniques.

In the earliest approach, Ringling and his colleagues [46] demonstrated 180 fs UV pulses by utilization of phase matched sequential frequency conversion of high peak power Ti-Sapphire laser pulses in three β Barium Borate (BBO) crystals (sum frequency mixing of a fundamental and its third harmonic). However, because of severe group velocity walk-off and phase matching bandwidth limitations inherent to the nonlinear crystals, the efficiency of the frequency conversions were reduced. Using gaseous nonlinear optical media can circumvent the pulse width limitations in the UV. Backus *et al.* [47] were the first who exploited a gaseous medium (air in their case) for generation of the then shortest ever UV pulses. They generated 16 fs pulses at 270 nm through a third harmonic conversion process. Later, other approaches were performed in hollow fiber [48] and filament [49] by parametric difference frequency mixing between the Fundamental Frequency (FF) and its Second Harmonic (SH) ($2\omega + 2\omega - \omega$). In the former case, 8 fs pulses with few microjoules energy were obtained while in the later, pulses were on the order of 12 fs with 20 μJ energies. More recently via direct frequency upconversion of sub 4 fs laser pulses at 750 nm focused into a Ne-filled, quasi-static gas cell, 2.8 fs UV pulses were demonstrated [50, 51].

In the direction of producing higher energy UV pulses, Nagy *et al.* [52] succeeded in the generation of 24 fs DUV pulses with energies of up to 200 μJ, by using the hollow fiber compression technique to high-energy pulses at 248 nm. In their work, 110 fs UV pulses were directly obtained from an excimer laser amplifier with 20 mJ energy. Ghotbi *et al.* [53] reported the generation of the highest pulse energies 300 μJ in the DUV spectral range with sub 20 fs duration. They took the advantage of the spectral broadening during filamentation in Argon. The UV pulses, applied

in their experiment, were generated from the Third Harmonic (TH) of an amplified Ti:sapphire laser system using BBO crystals.
So far, all mentioned techniques do not provide any wavelength tunability in UV region. Baum *et al.* [54] generated tunable sub 10 fs DUV pulses by second harmonic generation of a Noncollinear Optical Parametric Amplifier (NOPA). They used achromatic phase matching to circumvent the bandwidth limitations. However, the pulse energy was limited to 100 nJ, and the experimental setup was very complicated. Tunable pulses at about 1 μJ but with longer duration were produced by four-wave mixing in a hollow waveguide by Jailaubekov and Bradforth [55]. Ultrabroadband DUV pulses are also recently produced as the blue tail of a supercontinuum generated during filamentation of a few-cycle pulse at 800 nm in the air [56]. However, again the pulse energy is limited to 250 nJ. Later Beutler *et al.* reported the generation of tunable DUV pulses by directly frequency doubling the output of a high energy two stage visible NOPA without any spectral or angular beam shaping. They obtained about 10 μJ, sub-20 fs pulses tunable from 250 to 310 nm after pulse compression in a MgF_2 prism pair.
In our lab, ultrashort UV pulses are required for studying the spatio-spectral coupling effects of a UV pulse shaper. This study does not force the pulse to be at its extremes along the mentioned parameters (shortness, power and tunablity). Therefore, no complicated setup is required for generation of such pulses. We use the BBO crystals to convert the 800 nm output of the laser chain to 267 nm through sum frequency of the fundamental of the laser source and its second harmonic. In the following, I explain the experimental setup that I have built for generation of such pulses from our laser chain.

1.3.2 Experimental setup

As mentioned above, I have developed a source of ultrashort UV pulses at 267 nm to characterize the UV pulse shaper. The ultrashort UV pulses are produced through two subsequent nonlinear interactions: first second harmonic (SHG) of the laser source is generated using a BBO crystal and then the laser source and its generated second harmonic are combined in the second BBO crystal to generate UV pulses through sum frequency generation process (SFG). The second order nonlinearity $\chi^{(2)}$ is responsible for both SHG and SFG. Figure 1.4 shows the experimental setup. The horizontally polarized IR pulses from the laser source (chirped-pulse amplified: Tab. 1.1) with energy of 270 μJ/pulse and diameter of 2 mm are sent to a Type1 BBO crystal of

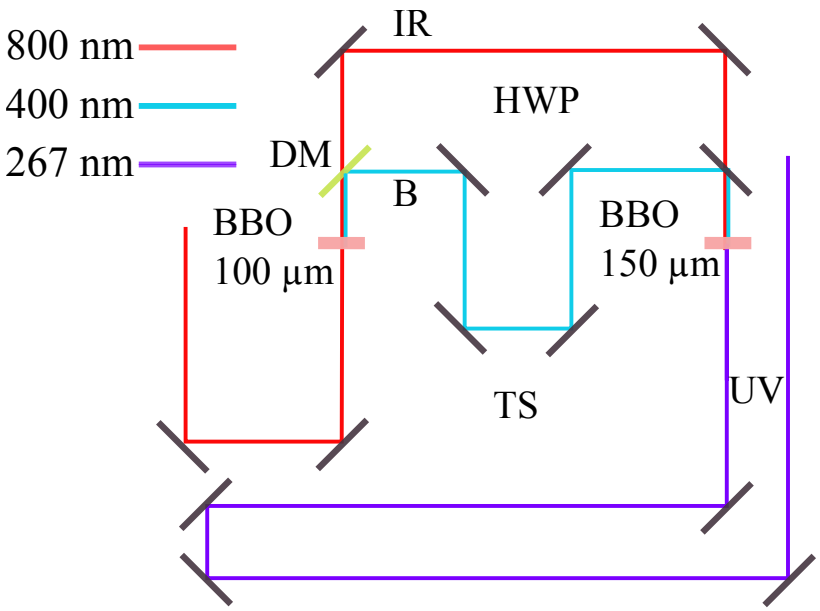

Figure 1.4: *Experimental setup for generation of ultrashort UV pulses. The ultrashort UV pulses at 267 nm are generated from sum frequency of the laser source (IR) and its second harmonic generation (B) in a type1-BBO crystal. The first type1-BBO crystal with thickness of 100 µm is used to generate second harmonic of the laser source. Second harmonic pulse and the residual IR pulse are separated from each other by a dichroic mirror (DM). The polarization of the residual IR pulse is rotated to be vertical by means of a half waveplate (HWP). The laser source and its second harmonic generation are then combined collinearly into the second type1-BBO crystal with thickness of 150 µm to generate UV pulses at 267 nm. The translation stage (TS) is used to insure the perfect synchronization of both arms into the crystal. The reflection bandwidth of mirrors used after generation of UV pulses is limited to UV region. This removes the residual IR and blue (second harmonic of IR) pulses.*

100 μm. This generates vertically polarized second harmonic pulses with energy of 70 μJ centered at 400 nm. The energy of the residual fundamental pulse is on the order of 180 μJ. The phase matching angle of the crystal is 29°. In the next step, two beams are separated by a dichroic mirror and the polarization of the residual IR beam is rotated to be vertical by means of a half-wave plate. Finally, the separated pulses are collinearly combined and directed to the second type1 BBO crystal of 150 μm (with phase matching angle of 45°) that yields horizontally polarized UV pulses through a sum frequency generation process. At the output, there still exists residual IR and Blue (second harmonic of IR) pulses. They are removed by using three consequent mirrors with reflection bandwidth centered at UV region. As mentioned, all beams are collimated. In more detail, no lens is applied to focus the beams on to the crystals. This may reduce the constraints of the phase matching condition

with the price of reduced efficiency of the nonlinear interactions. Figure 1.5(a) shows the spectral intensity of the generated UV pulses that are centered at 267 nm with bandwidth of 2 nm which supports transform-limited duration of around 50 fs at FWHM according to $\tau_p = \frac{2\ln 2\lambda^2}{\pi c \Delta\lambda}$ where λ is the pulse central wavelength, c is the speed of light in vacuum and $\Delta\lambda$ is pulse bandwidth at FWHM. Cross-correlation of UV pulse with laser source in the difference-frequency configuration using a thin type1 BBO crystal indicates a 150 fs pulse duration [see Fig. 1.5 (b)]. The difference between measured and transform-limited duration is attributable to dispersive effects within the nonlinear crystals of the source.

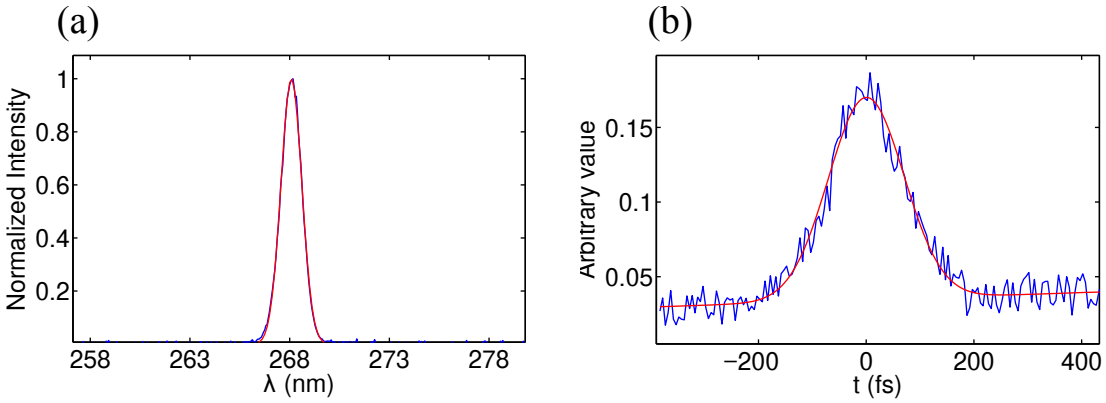

Figure 1.5: *Spectral and temporal intensity of the generated ultrashort UV pulse. (a) Solid blue line is the spectral intensity of the generated UV pulses measured by a calibrated spectrometer. Solid red line is the Gaussian fit with central wavelength of 267 nm and bandwidth of 2 nm at FWHM. (b) Solid blue line is the temporal intensity cross-correlation of the UV pulse with the IR laser source in difference frequency geometry. Solid red line is the Gaussian fit to the cross-correlation trace that has 200 fs bandwidth at FWHM leading to a 150 fs of UV pulse duration.*

1.4 Pulse shaping

Ultrashort pulse shaping techniques are complementary to femtosecond pulse generation and characterization techniques, because they have a wide range of applications in numerous fields of study. Their applications include coherent control of quantum mechanical processes [12–15], pulse compression [16], multidimensional nonlinear microscopy [17], optical communications [18] and factorization of numbers [19–21]. There exists wide variety of pulse shaping techniques [57, 58] among which we have applied two in our lab. The goal of this section is to briefly present their principle and basic properties. I start with folded 4f-line infrared pulse shaper in which a pair

of Liquid Crystal Spatial Light Modulators (LC-SLM) are embedded [59]. It is used for spatio-spectral control of multiply scattered light [see chapter 3]. The next pulse shaper is an Acousto-Optic Programmable Dispersive Filter (AOPDF) [40] which operates in UV region [60]. A complete space-time characterization of the AOPDF is presented in chapter 2 [61].

1.4.1 4f-line+LC-SLM

The design of the dispersion line (4f-line) has been pioneered by Froehly and his coworkers who developed it for picosecond pulses [62]. It consists of a pair of identical gratings and lenses. Figure 1.6 shows the geometrical configuration of this apparatus where all optical components are implanted in a straight line and separated from each other by f which is the focal length of the lenses. The spectral components of the

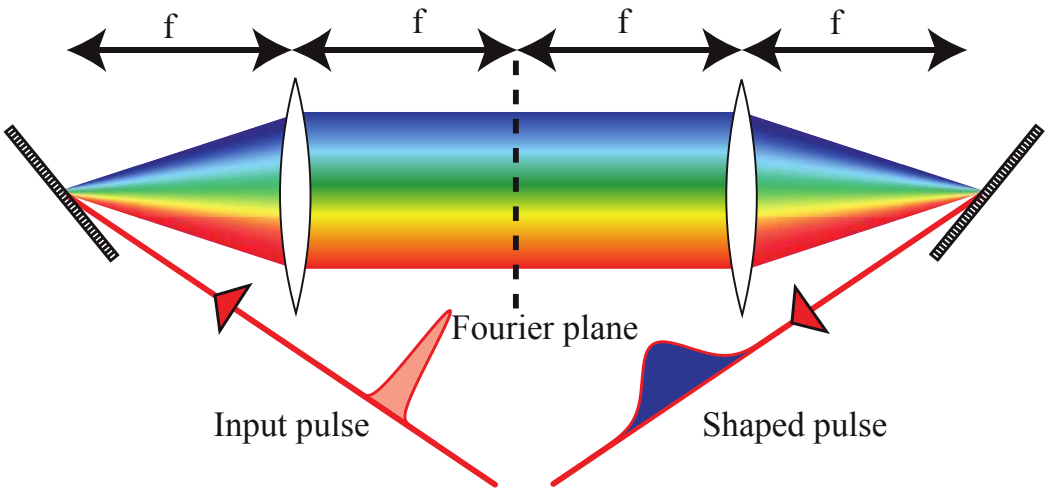

Figure 1.6: *Schematic configuration of a 4f-line pulse shaper. The optical elements are separated from each other by f which is the focal length of the lenses. The first grating disperses angularly the spectral components of the input pulse. The first lens collimates and focus them on to the Fourier plane. The second half of the device recombines the spectral components and reverts them to a single collimated beam. The spatial light modulators placed at the Fourier plane can modulate the phase, both amplitude and phase and also the polarization of the spectral components and hence shape the input pulse.*

input beam are angularly dispersed by the first grating. Then, they are collimated by the first lens and focused to the smallest diffraction spots in the Fourier plane. By applying a spatial filter in the Fourier plane, one can manipulate the optical path and/or amplitude [57, 63] and also the polarization [64] of each spectral component and hence shape the pulses as desired. The second half of the device recombines the spectral components and reverts them to a single collimated beam. Since the lenses in

the femtosecond regime introduce significant aberrations and dispersions, they maybe replaced by a pair of curved mirrors. In our case, the shaping in the Fourier plane occurs only in one spatial direction; therefore, cylindrical mirrors are used instead of spherical mirrors. Moreover, for the ease of alignment and also application of the least amount of the optical elements, complete line is converted to a folded line by removing the second half of the apparatus and embedding a mirror at the rear side of the spatial light modulators [59] [see Fig. 1.7].

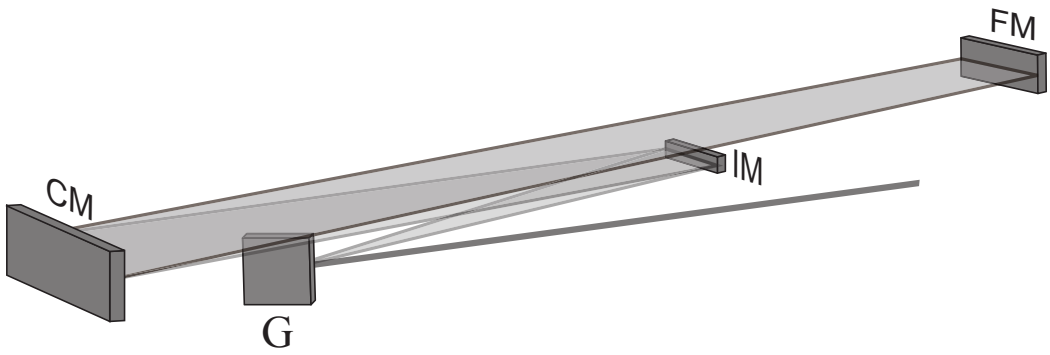

Figure 1.7: *Schematic demonstration of a folded 4f-line. The second half of the device is replaced by a mirror that is placed at the rear side of the spatial light modulators (Fourier plane). This simplifies the alignment and also reduces the amount of the used optical elements. CM is a cylindrical mirror, G is a grating, IM is an intermediate mirror and FM is the folded mirror.*

Spectral resolution

As it is mentioned above, the spectral components of the femtosecond pulse are dispersed spatially in the Fourier plane of the 4f-line. Shaping the pulse with a spatial mask requires the knowledge of the parameter α (spatial dispersion) that relates each dispersed spectral component ω_k to its corresponding spatial position x_k on the Fourier plane

$$x_k = \alpha\omega_k. \tag{1.11}$$

From optical properties of the grating and the lens (cylindrical mirror) α is set to be [23]:

$$\alpha = \frac{\lambda_0^2 f}{2\pi c d \cos\theta_{d0}} \tag{1.12}$$

where λ_0 is the central wavelength of the pulse, c is the speed of the light, d is the grating period and θ_{d0} is the diffracted angle of the central wavelength from the grating. From Eq. 1.11, the spectral resolution is set to be $\delta\omega = \delta x/\alpha$. δx is the

Parameter	Value
λ_0 (nm)	800
f (mm)	600
1/d (grooves/mm)	2000
δx_{in} (mm)	2
θ_i (°)	64

Table 1.2: *Properties of the optical elements applied in our 4f-line pulse shaper.*

spatial focus size of each spectral component in the Fourier plane which is given by [22]

$$\delta x = 2\ln 2 \frac{\cos\theta_i}{\cos\theta_{d0}} \frac{f\lambda_0}{\pi \delta x_{in}}. \tag{1.13}$$

Here, θ_i is the pulse incident angle to the grating and δx_{in} is the initial pulse diameter at FWHM which can be adjusted by a diaphragm used in the setup. Our 4f-line shaper is designed to work with pulses centered at 800 nm with bandwidth of 10 nm (old laser system). Given that the spatial mask has a pixel size of $\delta x_p = 97$ μm and total length of L=64 mm, optical elements according to Eq. 1.12 and Eq. 1.13, are chosen in a way that the focal points are of one third of the mask pixel size $\delta x_p = 3\delta x$ (Nyquist criterion). This is because the bigger spot size reduces the resolution of the pulse shaper. In contrast, smaller spots give rise to the pixellization effects. Moreover, the mask is three times larger than the spatial size of the pulse (corresponding to spectral bandwidth at FWHM) on the Fourier plane in order to avoid the cutting of the spectrum at the edges of the spatial mask [65]. Table. 1.2 shows the properties of the applied optical elements in our pulse shaper.

Temporal windows

The Fourier transform of spectral resolution yields the temporal windows of the pulse shaper

$$T = 4\ln(2)/\delta\omega = \delta x_{in}/|v| \tag{1.14}$$

where $|v| = cd\cos\theta_i/\lambda_0$ is the space-time coupling speed of the pulse shaper which will be briefly explained in the following. T is the upper bound of the pulse shaper and all the shaping in time domain should stay below this value. In our setup, T is typically on the order of 24 ps depending of the input beam diameter [65]. The lower bound of the temporal domain is given by Fourier transform of the bandwidth of the pulse in the spectral domain.

Spatial mask

Different masks with their own specific properties and applications can be embedded in the Fourier plane of the 4f-line among which the liquid crystal plates and acousto-optic modulators are the most popular ones [57, 58]. In our lab, we have applied a liquid crystal-spatial light modulator (LC-SLM) provided by the *Jenoptik* company. It consists of 640 separated programmable wave plates [see Fig. 1.8]. The LC-SLM consists of a nematic liquid crystal molecules that are sandwiched between two glass substrates. Nematic liquid crystals are small rod-like molecules whose orientation depends on the value of launched voltage. When no voltage is launched, they are parallel to the glass substrate (x-y plane). Depending on the amount of launched voltage they tend to rotate to the direction of the applied field (y-z plane). This rotation modifies the birefringence of the medium and results in modification of the optical path for polarized light along the anchorage direction.

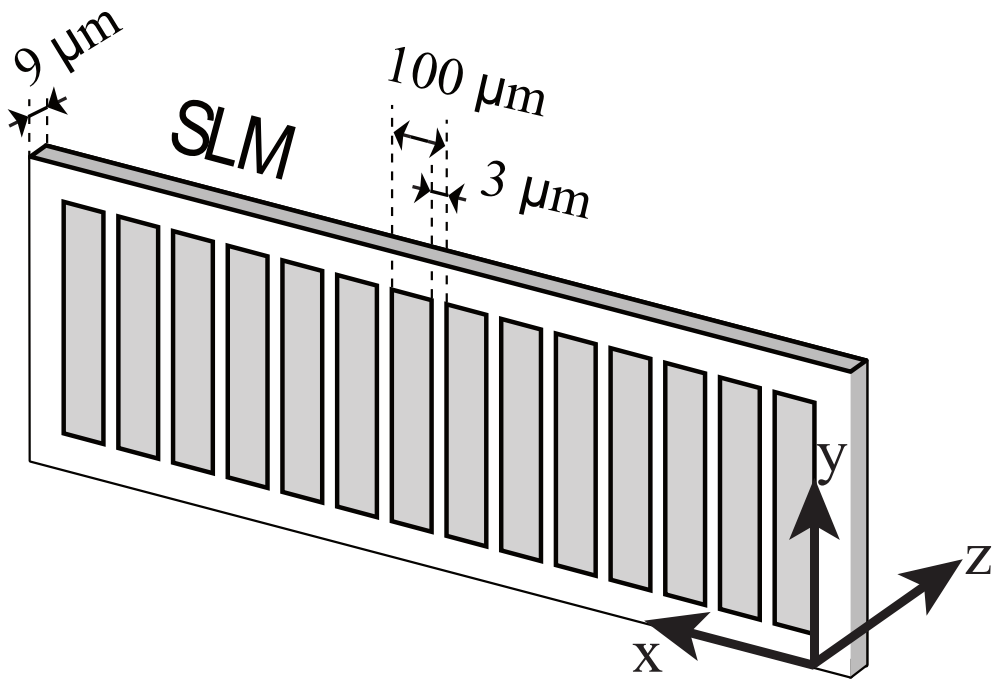

Figure 1.8: *Schematic demonstration of our Spatial light modulator placed in the Fourier plane of 4f-line apparatus. Pixel sizes are 97 μm with inter-gap of 3 μm. The crystal thickness is 9 μm.*

The desired voltage is launched to each pixel of the LC-SLM by means of transparent ITO (Indium tin oxide) electrodes that are coated on the glass substrate. For a

particular frequency ω the applied voltage U leads to phase change of

$$\phi(\omega, U) = \frac{\omega \Delta n(\omega, U) e_{CL}}{c} \tag{1.15}$$

where $\Delta n(\omega, U)$ is the difference of fast and slow refractive index of the crystal and e_{CL} is the thickness of our crystal. In our case, e_{CL} is 9 μm.
There exists different types of pulse shaping including amplitude, phase (both) and polarization depending on the initial alignment of the molecules and the number of the LC-SLM embedded in the 4f-line. The control of both phase and amplitude can be achieved by two masks where the molecules are initially perpendicular to the z axis and making 45° and -45° with respect to the horizontal axis x (x-y plane). Defining ϕ_1 and ϕ_2 respectively to be the phase of the first and the second mask, the final transfer function of the particular pixel k of the mask is set to:

$$H_k = \exp\left(i\frac{\phi_1(\omega_k) + \phi_2(\omega_k)}{2}\right) \cos\left(\frac{\phi_1(\omega_k) - \phi_2(\omega_k)}{2}\right) \tag{1.16}$$

where ω_k is the impinging frequency on pixel k.

Calibrations

Two calibrations should be realized before using the pulse shaper apparatus. The first one is the calibration of the produced phase that is associated to the applied voltage and the frequency. The next calibration is the dispersion calibration which means the mapping of ω_k to x_k. Both of them are completely detailed in the thesis manuscript of Monmayrant [65].

Limitations

The LC-SLM is a patterned plate with gaps between them that can not be programmed. These properties of the mask introduce some unwanted effects on shaped pulse. The unprogrammed gaps in the mask produce a weak zero delay impulse in the output shaped pulse which has sometimes comparable intensity with strongly shaped pulse [65]. The second unwanted effect comes from pixellization of the mask in spatial domain. Since the spectral domain is discretized it leads to a periodic impulse response in temporal domain with period of $T_{rep} = 2\pi/\delta\omega$.
The other limitation of such pulse shapers is the generation of spatio-temporal coupling effects at the output signal. For example when a pulse delay is programmed by the pulse shaper, at the output in addition to the temporal shift a spatial shift occurs

also along the transverse coordinate (along the direction that pulse shaping is performed). The ratio between the spatial and the temporal shift is precisely equal to the mentioned spatio-temporal coupling speed ν. The origin of this space-time coupling lies in the fact that in addition to the spectral masking in the Fourier plane of the pulse shaper, the spatial profile also undergoes a time-varying translational shift. Several articles [11,23,66,67] have covered spatio-temporal coupling in detail. The space-time coupling effect leads to a Gaussian temporal windows which attenuates the unwanted effects of pixellization. For more explicit description of the limitations and their removals I invite the readers to refer again to the thesis of Monmayrant [65]. This pulse shaper will be used in chapter 3 of this manuscript to control the spatio-temporal speckles.

1.4.2 Acousto-Optic Programmable Dispersive Filter

There exists an alternative method of pulse shaping different than 4f-line pulse shaper that is called Acousto-optic programmable dispersive filter (AOPDF) [40]. It has been invented in late 90th by Pierre Tournois in order to remove the residual phase of the chirped pulse amplifiers. Its principle finds an analogy with chirped mirrors [68] in which the various spectral components of the pulse experience different time delays by reflecting from different layers of the chirped mirror (fixed longitudinal grating). In the AOPDF that is commercially called the DAZZLER, the grating is transiently generated by interaction of the acoustic beam and birefringent crystal [69]. It was initially designed for operating in IR region by using of a TiO_2 crystal [70]; but later its application has been extended to the other optical regions covering mid IR [71] and UV [60,72] by using alternative crystals. In our lab, the temporal characterization of UV-AOPDF pulse shaper has been done by Weber [73,74]. Later, we have extended the characterization to the spatio-temporal domain [61]. In the following, I detail the performance concept and theory of the UV-AOPDF pulse shaper while its space-time characterization is detailed in chapter 2.

The pulse shaping in AOPDF is based on controlling the group arrival time of the pulse [69]. Using an anisotropic crystal helps to achieve this goal. In more detail, since the refractive index of the ordinary and extraordinary axis are different in anisotropic crystals, the spectral components propagating with polarization lying along the slow or fast axis will arrive at the end of the crystal with different delays. The group arrival time $\tau(\omega)$ is the derivation of the spectral phase $\partial\phi(\omega)/\partial\omega$. Therefore, one may control the spectral phase by modifying the group arrival time of the spectral compo-

nents. Figure 1.9 shows schematically the performance concept of the AOPDF pulse shaper where the input pulse is polarized along the ordinary axis of the anisotropic crystal (slow axis). Depending on the form of the desired output pulse, the spectral components diffract at different places of the crystal $z(\omega)$ and hence propagate with polarization along the extraordinary axis of the crystal. Analogous to nonlinear ef-

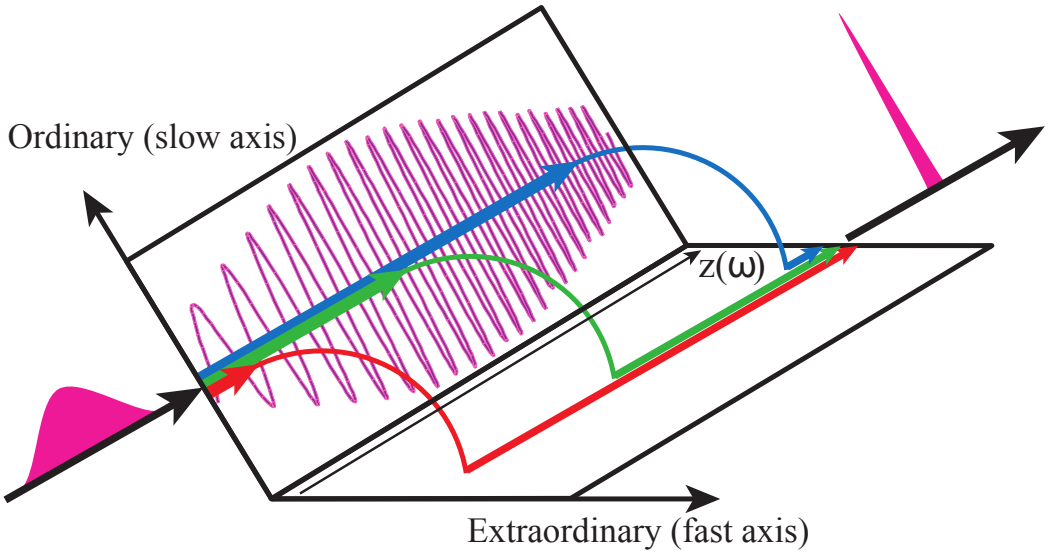

Figure 1.9: *Schematic demonstration of the AOPDF pulse shaper. Depending on the form of the desired output shaped pulse the spectral components of the incident pulse (along the ordinary axis) diffract at different positions of the birefringent crystal and hence propagate along the extra-ordinary axis. The diffraction occurs where the conservation of energy and momentum condition is satisfied between the acoustic and optical beam. Because of the difference of the refractive index along the two mentioned axes, spectral components experience different paths (group delay) and hence by controlling the group delays the output pulse takes the form of the desired shape.*

fects, the diffraction occurs when the energy and momentum conservation condition are verified between the launched acoustic wave and the optical beam:

$$\begin{aligned} \omega_d &= \omega_i + \Omega \\ k_d(\omega_d) &= k_i(\omega_i) + K(\Omega). \end{aligned} \tag{1.17}$$

Here, d and i are the indices of diffracted and incident beam respectively. K and Ω are the wave-vector and the frequency of the launched acoustic wave. The group arrival time of the different spectral components $\tau(\omega)$ is

$$\tau(\omega) = \partial\phi(\omega)/\partial\omega = \frac{z(\omega)}{v_{go}(\omega)} + \frac{L - z(\omega)}{v_{ge}(\omega)} \tag{1.18}$$

where L is the length of the crystal and v_g is the group velocity along the ordinary (o) and extraordinary (e) axis. Knowing the form of desired shaped pulse $\phi(\omega)$ yields $\tau(\omega)$. Referring to Eq. 1.18 and knowing the values of v_{go} and v_{ge} sets $z(\omega)$. Calculating the location of the interaction $z(\omega)$ reveals the $K(\Omega)$ from Eq. 1.17 [69]. The amplitude of each spectral component is controlled by the amplitude of applied acoustic wave at the place of diffraction $z(\omega)$.
In the frequency domain the output pulse can be written [40]:

$$E_d(\omega) \propto E_i(\omega) \cdot S_{ac}(\gamma\omega) \tag{1.19}$$

and equivalently in temporal domain:

$$E_d(t) \propto E_i(t) \otimes S_{ac}(t/\gamma) \tag{1.20}$$

where $\gamma = \frac{\Omega}{\omega} = \frac{|\Delta n|\nu_{ac}}{c}$ is the scaling factor between acoustic and optical frequencies. ν_{ac} is the acoustic wave speed and Δn is the difference of the refractive index of the fast and slow axis. Working in UV region and hence the choice of KDP crystal, γ is calculated to be approximately 1.3 $\times 10^{-7}$ [60]. This scaling value lets the direct transfer of the phase and the amplitude of the acoustic wave to the optical wave. The orthogonal polarization of diffracted and non diffracted beams makes it easier to distinguish the shaped pulse from the unshaped one.

Properties of our UV-AOPDF pulse shaper

Figure 1.10 shows the interaction geometry of our pulse shaper. The acoustic and the optical wave propagate in the plane consisting [100] and [001] axis of the crystal. The wave-vector of the acoustic wave K makes an angle θ_a with the [100] axis. θ_d and θ_i are respectively the angles of the diffracted and input optical wave vectors (k_d and k_i) with respect to [100] axis. The sound shear wave velocities along the [100] and [001] crystal axis are V_{100} =1650 m/s and V_{001} = 2340 m/s, respectively. The acoustic Poynting vector is aligned with the optical input optical beam to have optimized acousto-optic interaction length [70] which is realized when $\tan\theta_a = (\frac{V_{100}}{V_{001}})^2 \tan\theta_o$. This maximizes the spectral resolution and diffraction efficiency. Since the crystal is a birefringent medium, the diffracted beam experiences a refractive index n_d which depends on the propagation angle θ_d through:

$$1/n_d^2 = \cos^2\theta_d/n_o^2 + \sin^2\theta_d/n_e^2. \tag{1.21}$$

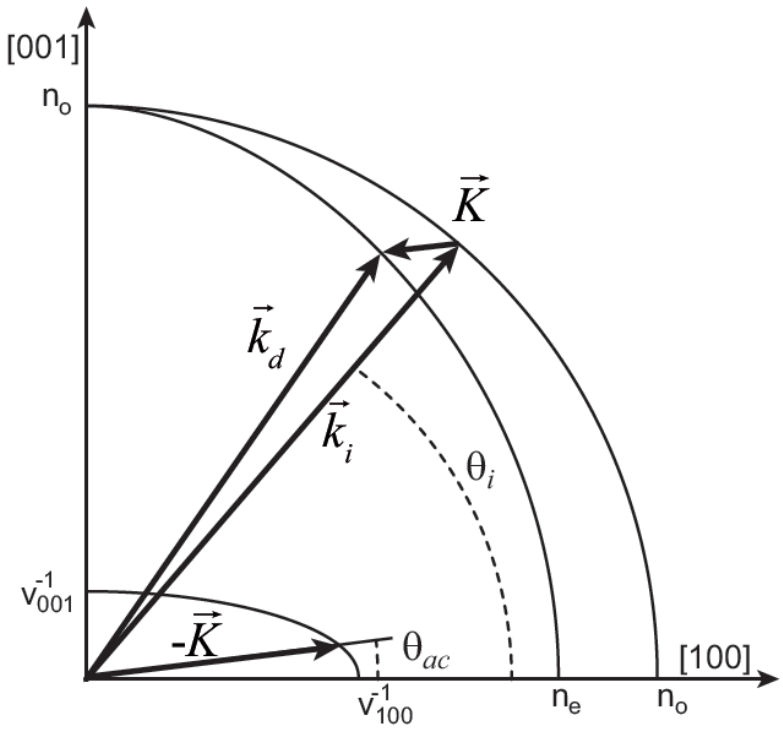

Figure 1.10: *Interaction geometry of our UV-AOPDF pulse shaper that consists of a KDP crystal with a negative anisotropy. The wave-vector of the acoustic wave K makes an angle θ_{ac} with the [100] axis. k_d and k_i are the wave-vectors of the diffracted and incident beam respectively. n_o and n_e are the ordinary and extraordinary refractive indices of the crystal. θ_i is the angle of the input optical wave-vector k_i with respect to [100] axis. The sound shear wave velocities along the [100] and [001] crystal axis are indicated by V_{100} and V_{001} respectively.*

In KDP crystal the optical anisotropy $\Delta n = n_o - n_e$ is small compared to n_o which yields $\delta n = n_d - n_o = \Delta n \cdot cos^2\theta_i$. Now according to the laws of energy and momentum conservation [Eq.1.17] the angles and the wave-vectors can be written

$$\begin{aligned} \theta_d - \theta_i &= \frac{\Delta n}{n_0} \cos^2\theta_i \tan\left(\theta_i - \theta_a\right) \\ K &= k_i \frac{\Delta n}{n_0} \frac{\cos^2\theta_i}{\cos\left(\theta_i - \theta_a\right)}. \end{aligned} \tag{1.22}$$

The ordinary and extraordinary refractive index of KDP crystal for $\lambda = 300$ nm are 1.5451 and 1.4977 respectively. The optimum incident angle of the optical beam θ_i for the case of maximum diffraction efficiency is calculated to be 48.5° [60]. The other calculated parameters of the KDP crystal is presented in Tab. 1.3 [60]. The other important parameters of the UV-AOPDF pulse shaper are spectral resolution, temporal

Parameter	Value
Δn	0.0474
θ_a (°)	29.34
$\theta_d - \theta_i$ (°)	0.269
n_d	1.5237
γ	$\frac{\Omega}{\omega} = 1.35 \times 10^{-7}$

Table 1.3: *Optimum parameters of the KDP crystal for a pulse with central wavelength of 300 nm.*

windows and the diffraction efficiency which can be calculated from the acousto-optic interaction theory that are addressed in reference [70]. For the specific case of KDP crystal, they are calculated in [60]. I only present the final equations and the calculated values for the KDP.

Efficiency

The efficiency of the diffraction for particular frequency ν is given by

$$\frac{I_d(\nu)}{I_i(\nu)} = \frac{P\pi^2}{4P_0} sinc^2\left[\frac{\pi}{2}\sqrt{\frac{P}{P_0} + \Delta\phi^2}\right] \tag{1.23}$$

where P is the acoustic power, $P_0 = \frac{1}{2M_2}\left[\frac{\lambda}{L\cos(\theta_i - \theta_a)}\right]^2$ where M_2 is the merit factor of the KDP crystal which depends on properties of the crystal and the speed of the acoustic beam in the crystal. Finally, $\Delta\phi$ is the phase shift due to the phase mismatching which gives:

$$\Delta\phi = \frac{\Delta KL}{\pi}\cos(\theta_i - \theta_a) \tag{1.24}$$

Since ultrashort pulses contain broad spectral bandwidth, it is not straight-forward to extract the efficiency of the output shaped beam.

Spectral resolution

The resolution of the KDP crystal $\delta\lambda$ for central wavelength of 270 nm and the crystal length of 75 mm is calculated to be 0.036 from [70]:

$$\delta\lambda = \frac{0.8\lambda^3}{\Delta nL\cos^2\theta_i} \tag{1.25}$$

when $\Delta\phi = 0.8$ and $P = P_0$. In this particular case the efficiency is about 50%.

Temporal windows

Temporal windows of the AOPDF is determined by the crystal thickness and its anisotropy. It is equal to the maximum difference of the group time of a particular frequency propagating upon along ordinary or extraordinary axis:

$$L\left(\frac{1}{v_{ge}}-\frac{1}{v_{go}}\right)=\frac{L\Delta n_g}{c}\cos^2\theta_i. \tag{1.26}$$

In our case where a KDP crystal with length of $L = 75$ mm is used, the temporal window T varies between 6-8 ps depending on the central wavelength of the input pulse.

1.5 Pulse measurement techniques

There exists a vast variety of ultrashort pulse measurement techniques that may be classified according to their performance. A basic distinction is based on the amount of information that they provide about the pulses: incomplete, nonself-referenced and self-referenced characterization methods. Methods lying in the first category usually give an estimate of the pulse duration or of the pulse intensity envelope without a full reconstruction of electric field $\tilde{E}(t)$. The most widely used methods for incomplete characterizations are intensity autocorrelation and cross-correlation. The remaining two categories allow a full reconstruction of the electric field. The difference between them is that the nonself-referenced methods require a previously well-characterized pulses, while self-referenced methods do not require this assistance.
In this section, I briefly introduce the techniques I have frequently used in our lab from the simplest to the most refined one. For more detailed and explicit description of pulse measurement devices I invite the interested readers to refer to [75].

1.5.1 Incomplete pulse characterization methods

Autocorrelations

Autocorrelation is a simple method to estimate the temporal intensity profile of the ultrashort pulses. In a conventional autocorrelator, the unknown pulse is divided into two replicas via a Mickelson interferometer. Then the replicas, with an adjustable relative delay τ, are focused into a nonlinear material (usually $\chi^{(2)}$) that generates second or higher order harmonic pulses. Finally, a slow detector records the generated

pulse as a function of the relative delay which reads

$$\begin{aligned} S_2(\tau) &= \int_{-\infty}^{\infty} \left|[E(t)+E(t-\tau)]^2\right|^2 \mathrm{d}t \\ &= 2\int_{-\infty}^{\infty} I^2(t)\mathrm{d}t + 2\mathrm{Re}\left\{\int_{-\infty}^{\infty} [E(t)E^*(t-\tau)]^2\,\mathrm{d}t\right\} \\ &+ 4\mathrm{Re}\left\{\int_{-\infty}^{\infty} I(t)E(t)\left[E(t-\tau)+E(t+\tau)\right]^*\mathrm{d}t\right\} \\ &+ 4\int_{-\infty}^{\infty} I(t)I(t-\tau)\mathrm{d}t. \end{aligned} \tag{1.27}$$

There are two types of autocorrelators depending on their geometry: intensimetric autocorrelator [76, 77] with noncollinear and interferometric autocorrelator [78, 79] with collinear geometry. In our lab, I use the intensimetric autocorrelator where two replicas are focused into the $\chi^{(2)}$ crystal with a modest angle [see Fig. 1.11a]. In this

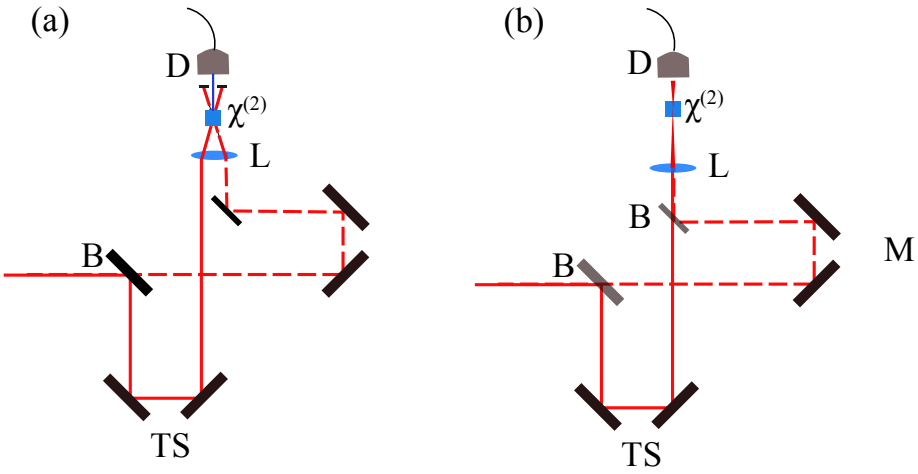

Figure 1.11: *Typical scheme of Autocorrelator. (a) Noncollinear geometry, (b) collinear geometry. TS is the translation stage, L is the lens, B is the beam splitter, $\chi^{(2)}$ is the nonlinear crystal, M is the mirror and D is the detector.*

configuration only the generated sum frequency replica of the two replicas is recorded, corresponding to the last term of Eq. 1.27. In other words, the noncollinear geometry allows only spatial filtering of the last term of the Eq. 1.27. This measurement does not contain any information about pulse phase and is just used to estimate the pulse duration; however, it is widely used in the community because of its simplicity. Changing the configuration from noncollinear to the collinear geometry with interferometric

stability results in the recording of all terms of the Eq. 1.27, known as interferometric autocorrelation [see Fig. 1.11 (b)]. The interferometric autocorrelator provides more information about the pulse than the intensimetric autocorrelator because the spectral phase can be retrieved via an iterative deconvolution algorithm[i] [80]. The general drawback of both arrangements is that they do not allow the evaluation of the asymmetry of the pulses (time ambiguity) [81].

Cross-correlations

Autocorrelators are not suitable devices to measure the pulses with complex temporal structures e.g. strongly chirped pulses or pulse sequences. In this case, a cross-correlator may be applied. It is obvious from Fig. 1.12 that a typical cross-correlator is analogous to the autocorrelator except that a short reference pulse is used instead of the replica pulse [82]. The advantage of cross-correlation measurement is its ability to measure weak signals that becomes possible by applying an intense reference pulse. Moreover, there is the possibility of applying the reference pulse from different spectral regions.

The reference pulse should be short enough to resolve the intensity structure of the test pulse. The limitation is that the intensimetric cross-correlation follows the same structure of the noncollinear autocorrelator and hence does not give full information on the pulse complex electric field. In our lab, I have often used intensimetric cross-correlation to measure the duration of UV pulses. It is realized by mixing the UV test pulses with the reference IR pulses in a thin Type1-BBO crystal to generate 400 nm pulses through difference frequency generation and recording them as a function of the relative delay between two arms on a slow photodiode operating in the visible region. Since a thin crystal is chosen the effect of group velocity walk-off and phase matching bandwidth limitations on the duration of the measured cross-correlation signal can be neglected.

1.5.2 Referenced characterization methods

Complete characterization of an ultrashort pulse requires measurement of the complex electric field $\tilde{E}(t)$. However, it is not possible to measure it directly because of the limited response time of the detectors which are at best several picoseconds. The solution to this problem is the indirect measurement of $\tilde{E}(t)$. This can be achieved by Fourier transforming the complex spectral electric field $\tilde{E}(\omega)$ which is constructed of

i. Retrieving the spectral phase requires a separate measurement of the pulse spectrum.

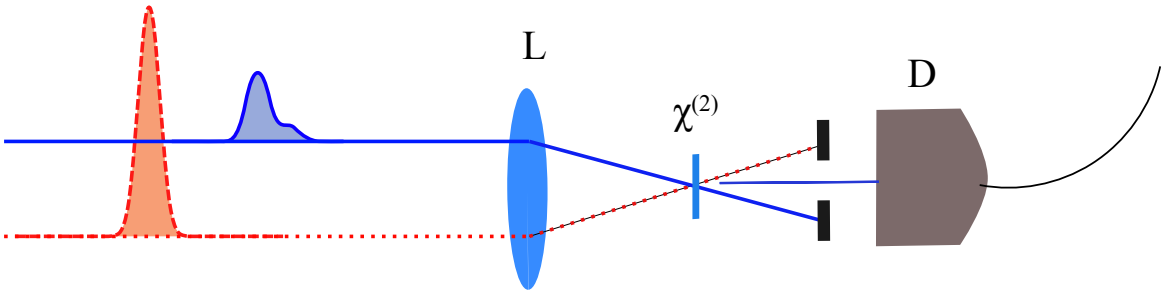

Figure 1.12: *Typical scheme of intensimetric cross-correlation. L is the lens, $\chi^{(2)}$ is the nonlinear crystal and D is the detector.*

spectral amplitude $|\tilde{E}(\omega)|$ and phase $\phi(\omega)$. The spectral amplitude $|\tilde{E}(\omega)|$ is obtained directly by measuring the spectrum $I(\omega) = |\tilde{E}(\omega)|^2$ via a spectrometer. The spectral phase $\phi(\omega)$ is obtained either by linear or nonlinear measurement techniques.
The linear measurement techniques are a different variation of conventional interferometry from which the relative spectral phase of two arms $\phi_s(\omega) - \phi_r(\omega)$ can be obtained. The sample phase can be retrieved only in the case of having a well characterized reference arm. The referenced characterization methods can be classified into spectral and temporal interferometry which are related to each other through a Fourier transform. In the following, I detail the referenced characterization methods specifically, the spectral interferometry that is often used in our lab.

Spectral Interferometry

Spectral Interferometry (SI) that was first introduced by Froehly and his coworkers [83] was used for measuring the dispersion of transparent materials by placing them in one of the arms of the interferometer. However, it was Joffre and his colleagues [84] who applied it for the first time as a pulse characterization technique. A conventional setup of SI is shown Fig. 1.13 where the test and the reference pulses are combined collinearly with an adjustable relative delay τ and sent to the spectrometer. The recorded signal exhibits a fringe pattern (Fig. 1.14) due to the interference which reads:

$$\begin{aligned} S(\omega) &= |\widetilde{E}_r(\omega) + \widetilde{E}_s(\omega)\exp(i\omega\tau)|^2 \\ &= |\widetilde{E}_r(\omega)|^2 + |\widetilde{E}_s(\omega)|^2 + \widetilde{E}_r^*(\omega)\widetilde{E}_s(\omega)\exp(i\omega\tau) + c.c. \\ &= |\widetilde{E}_r(\omega)|^2 + |\widetilde{E}_s(\omega)|^2 + 2\left|\widetilde{E}_r(\omega)\right|\left|\widetilde{E}_s(\omega)\right|\cos\left[\omega\tau + \phi_s(\omega) - \phi_r(\omega)\right] \end{aligned} \tag{1.28}$$

where c.c. is the complex conjugate of the third term. The first two terms in this

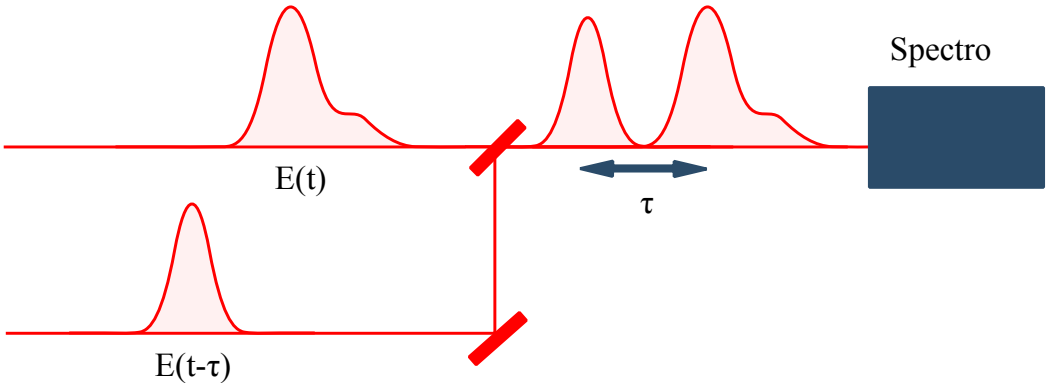

Figure 1.13: *Typical scheme of a spectral interferometer. The reference and the test pulse with an adjustable relative time delay τ are sent to the spectrometer. The spectrometer records the interference fringes from which the relative spectral phase of the reference and the test pulses $\phi_s(\omega) - \phi_r(\omega)$ is retrievable.*

expression are spectral intensity of the reference and sample pulses respectively. The third term corresponds to the fringes in the power spectrum. The spacing of the fringes $\delta\omega_{fr}$ is determined by the relative delay of the two beams τ. These fringes are additionally modulated by the relative phase difference of two beams $\phi_s(\omega) - \phi_r(\omega)$. One possible method for the relative phase extraction would be

$$\Delta\phi = \cos^{-1}\left[\frac{S(\omega) - I_r(\omega) - I_s(\omega)}{2\sqrt{I_r(\omega)I_s(\omega)}}\right]. \tag{1.29}$$

This requires the separate measurement of the reference and the sample arms. However, the application of this method is impossible because cos^{-1} is not a single valued function and hence yields an ambiguity in the sign of the phase. Furthermore, the raw data should be divided by the square root of the measured intensity which introduces a drastic noise to the calculated phase. There are couple of other indirect phase determination techniques based on introduction of a relative delay τ. For example the relative phase can be extracted by pointing the maxima of the fringe pattern [85]. However, the most common method among them is Fourier filtering technique [86]. Figure 1.14 shows the Fourier filtering process where the measured interference pattern is first Fourier transformed along the spectral dimension. The first two slowly varying terms of Eq. 1.28 correspond to a lobe located at $t = 0$ in quasi-temporal domain which is called the dc term. The dc term is the electric field autocorrelation function of the pulses which corresponds to a duration of a signal and reference pulse with a flat spectral phase (Fourier limited pulses). The two lobes located at t = $\pm\tau$

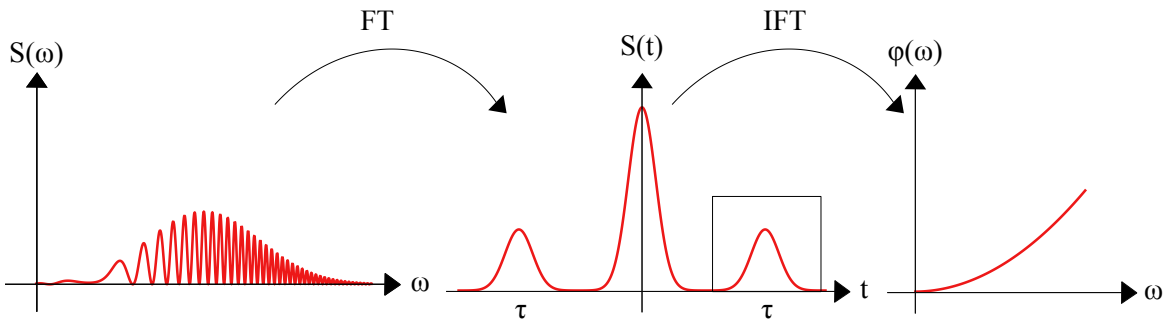

Figure 1.14: *Fourier filtering process. Combination of a Fourier transform limited reference and a chirped pulse results in interference fringes with a frequency inversely proportional to the relative delay τ. They are additionally modulated by the relative spectral phase of two arms. Fourier transforming the recorded signal along the spectral dimension yields three lobes separated by τ in quasi-temporal domain. Filtering one of the ac lobes located at $\pm\tau$ and Fourier transforming back reveals the relative spectral phase of the reference and test pulses.*

are the Fourier transform of the third term of the Eq. 1.28 and correspond to the cross-correlation of the temporal electric fields. The duration of the sideband lobes depends on the duration of the test and reference pulses. Filtering one of the sideband lobes by a rectangular filter in quasi-temporal domain and Fourier transforming back yields the third term of the Eq. 1.28 from which the relative phase can be easily determined. The spectral interferometry is called Fourier Transform Spectral Interferometry (FTSI) when the Fourier filtering algorithm is applied for the extraction of the spectral phase.

Applying FTSI has some conditions that should be fulfilled to properly reconstruct the spectral phase difference. Referring to Eq. 1.28 shows that the reference pulse spectral intensity should be non-zero where the spectral intensity of the test pulse is present. Furthermore, the two arms of the interferometer should be coherent. Finally, there is an upper and lower limit for τ. The spectral resolution of the spectrometer $\delta\omega$ should be a few times finer than the fringe spacing $\delta\omega_{fr}$ to resolve it properly

$$\delta\omega_{fr} = 2\pi/\tau > 3\delta\omega. \tag{1.30}$$

This defines the upper limit of τ. The lower limit is originated from application of the Fourier filtering. In fact, in order to be able to filter the ac term from the dc term in quasi-temporal domain the lobes should be well separated. This implies that $\tau > 3T$, where T is the duration of the longest of both the reference and test pulse.

According to Shannon criterion the spectral resolution of the spectrometer should be

at least three times finer than the inverse of pulse duration

$$3\delta\omega < 2\pi/T \tag{1.31}$$

or in other words the temporal window ΔT should be at least three times larger than the pulse duration $\Delta T > 3T$. However, in the case of application of Fourier filtering process, the temporal window should be at least nine times larger than the pulse duration. This is because three lobes are separated by τ which is at least three times larger than pulse duration T. This can be considered as a drawback for the Fourier filtering which implies a higher spectral resolution than it is required, much of which is lost in the reconstruction process. However, this problem can be solved by introducing a spatial dimension to the spectral interferometry which I will present in next chapter as Fourier Transform Spatio-Spectral Interferometry (FTSSI).

Temporal interferometry

Temporal interferometry is the temporal counterpart of the spectral interferometry and has a same setup as spectral interferometry except that the spectrometer is replaced by a slow detector, e.g. photo-diode. It records the energy superposition of the two fields as a function of the time delay τ [see Fig. 1.15]. The measured signal reads:

$$\begin{aligned} S(\tau) &= \int_{-\infty}^{\infty} |E_r(t-\tau) + E_s(t)|^2 \, dt \\ &= \int_{-\infty}^{\infty} |E_r(t-\tau)|^2 \, dt + \int_{-\infty}^{\infty} |E_s(t)|^2 \, dt + \int_{-\infty}^{\infty} E_r^*(t-\tau) E_s(t) dt + c.c. \end{aligned} \tag{1.32}$$

The first two terms yield a constant background signal while the last two terms correspond to interference fringes whose frequency ω_0 is the center frequency of the measured pulse. These terms correspond directly to the electric field cross-correlation of two pulses. Fourier-transforming along the temporal axis yields three lobes in quasi-spectral domain located at $\omega = 0, \pm\omega_0$. The lobe at ω_0 stands for $\tilde{E}(\omega)\tilde{E}^*(\omega)$ from which the relative spectral phase can be extracted. The temporal interferometry accompanied with Fourier filtering process is called Fourier-Transform Spectroscopy (FTS) [87, 88]. According to Shannon principle the temporal step size $\delta\tau$ should be at least three times finer than the optical period of the pulse T_0

$$3\delta\tau < T_0 = 2\pi/\omega_0. \tag{1.33}$$

The optical oscillation in visible region is so fast which makes this technique less practical in the visible than in the infrared. The other drawback of the temporal interferometry compared to SI is that the delay between two arms should be scanned, while it is done only by a single measurement in SI. In this technique the number of steps is determined by the complexity of the test pulse. Dealing with more complex pulses requires a better spectral resolution $\delta\omega = 2\pi/N\delta\tau$ which results in increasing N and therefore longer process.

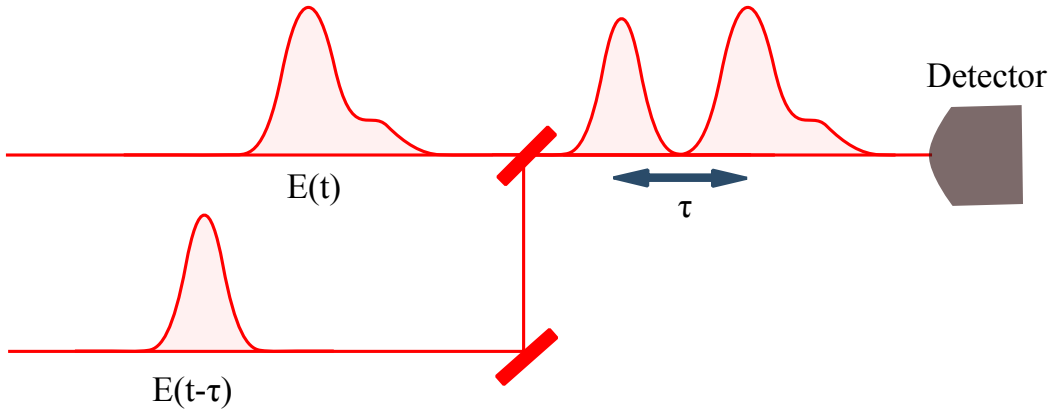

Figure 1.15: *Typical scheme of a temporal interferometry. It is analogous to the spectral interferometry with a minor difference which is the replacement of the spectrometer by a detector. The detector records the signal as a function of two arms' relative delay.*

1.5.3 Self referenced characterization methods

Ultrashort characterization devices implementing stationary linear optics are able to perform a complete measurement of the ultrashort pulses only when we use a fully characterized references. In order to circumvent the necessity of applying a well characterized reference and hence having a self-referenced complete characterization, one ought to apply nonlinear or non-stationary optics [87,89]. There are three main classes of techniques performing a complete self-referenced characterization: tomographic, spectrographic and interferometric techniques among which, the spectrographic and interferometric are more common. Spectrographic techniques are based on measuring the spectrum at different temporal slices of the test pulse. The most established spectrographic technique is Frequency Resolved Optical Gating (FROG) [9, 90]. It performs the temporal gating (slicing) by sending the test pulse and its tunable delayed replica into a nonlinear crystal. Then a spectrometer records the spectrum of the gated pulse as a function of the delay between the test pulse and its replica. This

yields a time frequency signal distribution from which one can extract the spectral phase and amplitude of the test pulse using an iterative algorithm [91, 92]. Since I have used the interferometric techniques in our lab, I present them more in detail in the following.

Interferometric techniques

It has been mentioned that spectral interferometry is a powerful tool for retrieving the spectral phase of the unknown pulses only under the condition of having a well characterized reference pulse. In order to have self referenced measurement, there should be a connection between the reference and the signal arm so that the phase can be determined from the relative phase difference. Lateral Shearing interferometry (LSI) [93, 94](to be described briefly in next chapter), which is widely used in characterization of the wavefront of monochromatic light, inspired researchers to invent the Spectral Shearing Interferometry (SSI). It is based on generation of a replica from the test pulse with a relative delay τ and a frequency shift Ω. Therefore the interference signal reads

$$\Gamma(\omega) = \phi(\omega + \Omega) - \phi(\omega) + \omega\tau \tag{1.34}$$

from which $\phi(\omega)$ can be extracted via either an integration or a concatenation procedure. The next step is the experimental realization of the desired spectral shearing. There exist several techniques for this purpose among which Spectral Phase Interferometry for Direct Electric Field Reconstruction (SPIDER) is the most common one [8]. In a conventional SPIDER the spectral shear is achieved via sum-frequency generation process. In other words, the test pulse and its delayed replica are upconverted with two different quasi-monochromatic pulses. Since quasi-monochromatic pulses have different central frequencies the upconverted test pulse and its replica will be spectrally sheared. Figure 1.16 depicts a standard SPIDER setup where the test pulse is divided into three arms. Two of them are devoted to generation of two temporally delayed, τ, replicas of the test pulse and the third one to generation of a strongly chirped pulse via a pulse stretcher. The chirped pulse is stretched such that it is quasi-monochromatic over the duration of the test pulse. Next, the replicas and the chirped pulse are focused into a nonlinear crystal (conventionally the second order crystal $\chi^{(2)}$). The relative delay τ forces the replicas to experience a different spectral component of the chirped pulse in the crystal. These two quasi monochromatic spectral components are separated from each other by $\Omega = \tau/\phi^{(2)}$ where $\phi^{(2)}$ is the chirp of the dispersed pulse. The sum frequency generated pulses are therefore

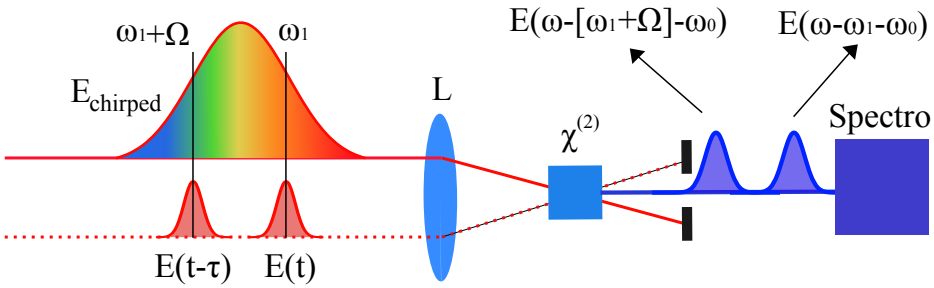

Figure 1.16: *typical scheme of a SPIDER. The test pulse and its delayed replica interacts with to different spectral components of a strongly chirped pulse in a nonlinear crystal. The spectrometer records the interference of two generated up converted pulses from which the spectral phase of the test pulse can be retrieved.*

$E(\omega-\omega_1-\Omega-\omega_0)$ and $E(\omega-\omega_1-\omega_0)$ where ω_1 and $\omega_1-\Omega$ are the frequencies of the chirped pulse which are contemporaneous with the test pulse replicas in the crystal and ω_0 is the central frequency of the test pulse and its replica. The upconverted signal is sent into the spectrometer that reads

$$\begin{aligned} S(\omega') &= |E(\omega') + E(\omega'-\Omega)\exp(i\omega'\tau)|^2 \\ &= |E(\omega')|^2 + |E(\omega'-\Omega)|^2 + 2\,|E(\omega')|\,|E(\omega'-\Omega)|\cos\left[\phi(\omega'-\Omega) - \phi(\omega') - \omega'\tau\right] \end{aligned} \tag{1.35}$$

where $\omega^{'} = \omega - \omega_1 - \omega_0$ sets the upconverted frequency to the origin. Identical to spectral interferometry, a Fourier Transform Algorithm renders the phase difference from which the spectral phase of the test pulse can be extracted. Here in the SPIDER technique, τ follows the same conditions that was defined for FTSI.

The SPIDER setup is now well established and commercially available. In our lab, we have used a commercial Long Crystal SPIDER (LX-SPIDER) to characterize the output of our laser chain [95, 96]. It is a compact and user friendly device that performs a reliable measurement for the pulses with duration longer than 20 fs. However, it requires lots of calibrations and adjustments. Moreover, because of applying dispersive elements in its setup, it is not proper device for characterization of ultrabroad band pulses (few cycle pulses). Different types of SPIDER have been developed in recent years to overcome these limitations. However, since all SPIDER techniques are based on nonlinear interactions, they are not sensitive to weak signals. In our lab, to overcome the challenging issue of calibrations and the insensitivity to the weak signals, we have used the FTSI technique with an additional spatial dimension (FTSSI to be explained in chapter 2). It will be used for spatio-temporal characterization of

the UV-AOPDF pulse shaper (chapter 2) and spatio-temporal speckles (chapter 3).

Chapter 2

Space-time couplings of UV-AOPDF pulse shaper

When there exists an interdependence between spatial (angular) and spectral (temporal) coordinates of the ultrashort pulses, they are referred to as spatio-temporally coupled pulses. These couplings, which are due to the broad spectral bandwidth of the ultrashort pulses, are introduced from their propagation in optical elements such as gratings, prisms and air. These couplings often erode temporal resolution, reduce intensity and cause a wide range of other problems. Therefore, in order to properly understand and control them, an extensive study and characterization of them and their sources is required.

Pulse shapers [57] are also main sources of space time couplings. Since they have wide range of applications in the ultrafast community, studying their relevant couplings are highly desired. Extensive studies of the pulse shapers based on 4f-line configuration have been already undertaken and it is now well known both experimentally and theoretically that the output shaped pulses of such devices are spatio-temporally coupled [11, 22–26]. Even more, the influence of space time couplings on a focused beam from SLM based 4f-line pulse shapers has been demonstrated that has significant effects on the coherent control experiments [66, 67]. By contrast, the AOPDF pulse shapers which have wide range of applications in CPA systems [97] and control experiments [98], have been less well characterized [26, 99–101]. They are good candidates for pulse shaping due to their versatility, compactness, ease of alignment, and wide wavelength range.

This chapter is devoted to complete characterization of the space-time coupling effects produced by the UV-AOPDF pulse shaper (published in [61]). It consists of mathe-

matical description of coupling effects, their characterization techniques, experimental results and conclusion. In mathematical description, I will review the general characteristics of space-time couplings, how different couplings are related to each other, what are the common sources of such couplings and how one can mathematically describe them. In the second section, I present the current state of space-time coupling measurement techniques. Later, I will present the experimental results concerning the spatio-temporal characterization of the UV-pulse shaper and the physical origin of such couplings. Finally in the conclusion, I will compare our experimental results with two recently published articles [100, 101] and I will conclude.

2.1 Mathematical description of space-time couplings

In the previous chapter, the spatial and temporal dependences of the ultrashort pulse were assumed to be separable into independent functions and hence the solutions of the wave equation were derived independently for each of the dependences. However, this assumption fails when there is a coupling between these dependences and hence the pulse can not be written anymore in the form of $\tilde{E}(x, y, t) = \tilde{E}(t)\tilde{E}(x, y)$. These couplings are called spatio-temporal couplings or distortions and one needs to describe them in a combined space (wavenumber) and time (frequency) picture. For the ease of calculation, I assume the couplings occur along one of the spatial axes x. These couplings are common in ultrafast optics and applied frequently in the generation, amplification and manipulation of the ultrashort pulses. As an example, the space-time coupling is introduced deliberately by a set of gratings or prisms in a specific configuration to produce a pulse with a negative chirp to compensate the positive chirp introduced from propagation of the pulse in the dispersive media [43, 102–104]. An other common example is the shaping of the pulses with a zero dispersion 4f-line pulse shaper. In such pulse shapers the spectral components of the pulse are spatially separated to perform a desired pulse shaping by varying the phase of each spectral component using a spatial light-modulator (SLM) [57]. The spectral components of the output pulse, after being manipulated, should be recombined again to form a coupling free pulse. However, a small and almost inevitable misalignments often allow some residual distortions to remain in the beam. These distortions often deprave the temporal resolution and hence cause several problems in the experiments in which such pulses are applied. Even in the case of a perfect alignment the applied SLM

couples the spatio-temporal dependences of the output shaped pulses.
In the presence of the space-time couplings, four possible representations exist for the electric field: (x,t), (x,ω), (k,ω) and (k,t) where each domain is the Fourier transform of the other. Considering only the first order couplings, there exists four possible couplings for the amplitude of the electric field corresponding to each of four domains. Apart from amplitude couplings the phases may be also coupled which results in total of eight first-order space-time couplings. For example $E(x)E(\omega+\alpha x)$ reveals the coupling of the spectral and the spatial dependencies of the pulse amplitude where α is the coupling parameter and shows the strength of the coupling between two dependences. The physical significance of the couplings could be nontrivial in a specific domain while more intuitive in the others. Table 2.1 shows all the possible lowest-order space-time phase couplings and their description in the parallel other domains. Three types of space-time coupling are particularly common: Spatial Chirp (SC), Angular Dispersion (AD) and Pulse Front Tilt (PFT).

Spatial chirp

Spatial chirp is one of the most common sorts of couplings that occurs when the central frequency of the pulse varies with the transverse position. A common source of the spatial chirp is the angularly dispersive optical elements such as gratings or prisms [see Fig. 2.1(a)]. The propagation of the ultrashort pulse through such elements causes the angular separation of the spectral components. These components later become spatially separated after an additional propagation. A tilted substrate also spatially separates the spectral components [see Fig. 2.1(b)]. Spatial chirp may be also generated deliberately in the zero dispersion 4f-line pulse shapers where the spectral components are desired to be spatially separated in the location of the Fourier plane [see Fig. 2.1(c)]. The use of ultrashort pulses contaminated with the spatial chirp may yield inappropriate results in the corresponding experiments. For example, when the temporal resolution of the pulses is the aim of their application, in the presence of the spatial chirp, each ray of the pulse will contain only a fraction of the full pulse spectrum and hence will not be as short as the pulse containing all spectrum. Moreover, the presence of spatial coupling can result in confused interpretations in the pump probe spectroscopy experiments. In other words, since in such experiments the optical pulses are focused on to the medium, the presence of the spatial chirp results in a temporally stretched pulse.
There are two definitions of spatial chirp [105,106]. The first one measures the central

(x,ω)	(x,t)	(k_x,ω)	(k_x,t)
Spatial chirp $\tilde{E}(x+\xi\omega,\omega)$ Frequency dependent beam center position	—	$\tilde{E}(k_x,\omega)\exp(i\xi k_x\omega)$ Wavenumber-spectral phase	$\tilde{E}(k_x,t-\xi k_x)$ Wavenumber dependent arrival time
$\tilde{E}(x,\omega)\exp(-i\alpha\omega)$ Spatio-spectral phase	**Pulse front tilt** $\tilde{E}(x,t+\alpha x)$ Position dependent pulse arrival time	$\tilde{E}(k_x+\alpha\omega,\omega)$ Frequency dependent tilt	—
—	$\tilde{E}(x+\zeta t,t)$ Time dependent beam center position	**Angular Dispersion** $\tilde{E}(k_x,\omega+\zeta k_x)$ Wavenumber dependent center frequency	$\tilde{E}(k_x,\omega)\exp(i\zeta k_x t)$ Wavenumber-temporal phase
$\tilde{E}(x,\omega-\beta x)$ Position dependent frequency	$\tilde{E}(x,t)\exp(-i\beta x t)$ Spatio-temporal phase	—	**Time versus angle** $\tilde{E}(k_x+\beta t,t)$ Time dependent tilt

Table 2.1: *Representation of space–time couplings in different domains including spatial chirp (first row), pulse front tilt (second row), angular dispersion (third row) and time versus angle coupling (last row). Each of these couplings can be also represented in other domains; however, they are more trivial in one specific domain. Empty boxes mean that there is no clear description in such domain.*

frequency of each spatial slice $\omega_0(x)$. In this case, the coupled complex electric field can be written as $\tilde{E}(x,\omega+\varsigma x)$ where $\varsigma=\partial\omega_0(x)/\partial x$ is the coupling parameter called frequency gradient. The other, includes measurement of the beam center position for each spectral component $x_0(\omega)$. In this case, the coupling can be expressed by $\tilde{E}(\omega,x+\xi\omega)$ where $\xi=\partial x_0(\omega)/\partial\omega$ is the alternative parameter of coupling called spatial dispersion. For experimental considerations it is important to pay attention to the way the couplings are actually introduced. The use of spatial dispersion will make the beam larger in size when mapping each frequency to a different position. On the other hand, a frequency gradient will increase the frequency bandwidth. Since the spatial chirp is most commonly introduced through linear optical systems, which rarely alter the bandwidth, spatial dispersion is more fundamental and so is preferred. In our studies, we have applied the spatial dispersion definition.The general theory of first-order spatio-temporal distortions including the interdependence of the mentioned

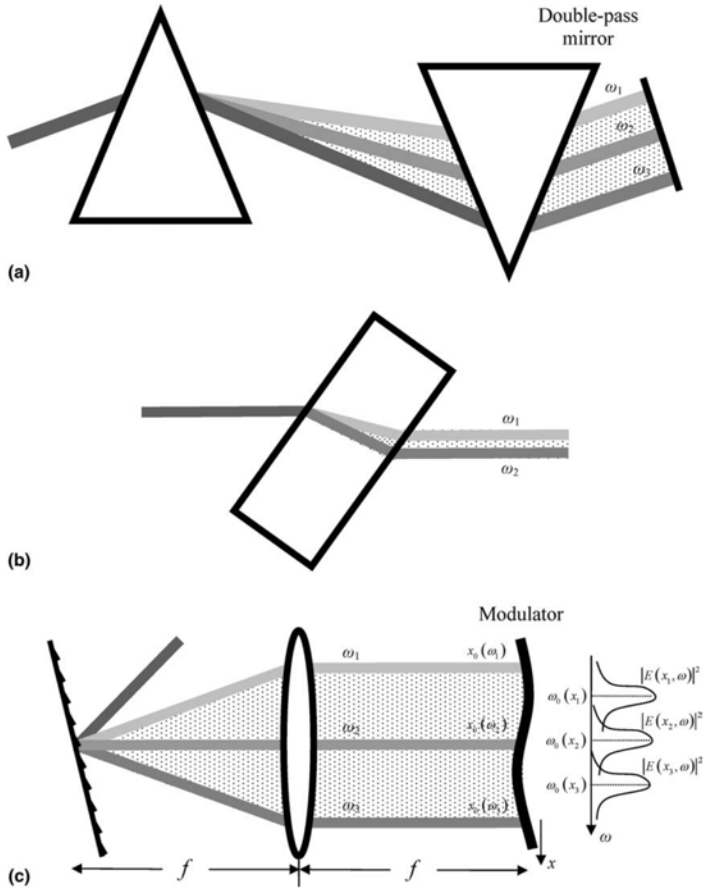

Figure 2.1: *Generation of spatial chirp. (a) The propagation of ultrashort pulses through a prism causes an angular separation of the spectral components. Propagation of angularly dispersed pulse through a second prism results in spatial chirp. (b) Propagation of broadband pulse through a tilted substrate also produces spatial chirp. (c) The case of generation of a deliberate spatial chirp in a 4f-line pulse shaper. The figure is adopted from [105].*

definitions was developed by Akturk *et al.* [107, 108].

Angular dispersion

Angular dispersion is introduced by angularly dispersive optics such as grating or prism which refers to a situation in which the spectral components of the ultrashort pulse propagate in different directions [see Fig. 2.1 (a)]. It is one of the most applied and useful distortions, because it causes a negative group velocity dispersion (negative chirp) which is used to compress the pulses that are stretched from propagating in dispersive media (positive group velocity dispersion). Angular dispersion can be written in the form of $E(k_x, \omega + \zeta k_x)$ where $\zeta = \partial k_x(\omega)/\partial\omega$ is the coupling parameter

and $k_x(\omega)$ is the wave-vector for each spectral component. Similar to the case of spatial chirp the angular dispersion can be written in the alternative form where the frequency is wave-vector dependent.

Pulse front tilt

Pulse front tilt occurs when the arrival time of the pulse peak is position dependent $t_0(x)$. The pulse front tilt is always generated in presence of the angular dispersion but the angular dispersion is not the only source of the pulse front tilt [see Fig. 2.2]. In other words, in the absence of the angular dispersion the combination of the spatial chirp and temporal chirp also generate a pulse front tilt [109]. PFT can be written in

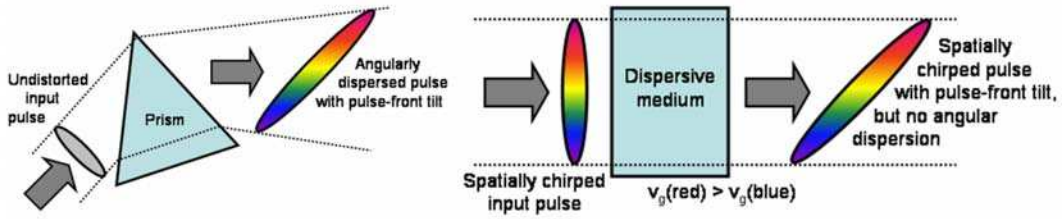

Figure 2.2: *Two sources of pulse-front tilt. Left: The well-known angular dispersion results in pulse front tilt. Right: The combination of spatial and temporal chirp yields a pulse front tilt. The figure is adopted from [109].*

the form of $E(x, t + \alpha x)$ where α is the coefficient of the pulse front tilt. It should be noted that the pulse front tilt is different than pulse tilt. In the presence of the pulse front tilt the group phase (the plane of constant group delay at the center frequency) is tilted with respect to the phase front (the plane of constant phase at the center frequency) whereas in the case of pulse tilt both phase front and group front are tilted with a same amount.

So far, the gratings, prisms, and tilted substrates are mentioned as a source of space-time couplings. The lenses are other commonly applied optical devices that introduce the spatio-temporal couplings (combination of first and higher order distortions) [91, 110–116]. These couplings are mainly due to the combination of the achromatic aberrations and the radial varying group delay and group velocity dispersions. In more detail, the radially varying thickness of the sample introduces radially varying group delay and group velocity dispersion which increases the pulse duration at the focal point.

2.2 State of the art of space–time measurements

In the previous chapter, I focused on ultrashort pulse characterization techniques. All these methods reconstruct the overall temporal electric field or intensity of the pulses (averaged over spatial profile) without providing any information about their spatial characteristics. The reconstructed electric field is valid only when we assume that the pulse's electric field is separable into a product of spatial and temporal dependencies or equivalently, the pulse's temporal properties are same for every spatial position along the beam. When space-time couplings are present this assumption fails and therefore each spatial position along the pulse wavefront will have its own specific temporal properties. Studying the space-time couplings, which is the interest of this section, thus requires either the extension of the conventional temporal characterization techniques to the spatial domain or invention of novel independent instruments. In this section, I review the state of art of the measurement techniques used for space-time characterization of the ultrashort pulses. I first start with spatial characterization techniques that can be combined with the temporal measurement methods to measure the pulse couplings. Then, I move to a presentation of the space-time characterization techniques which are only able to measure some specific space-time couplings. Finally, I focus on full spatio-temporal characterization methods among which I use Fourier Transform Spatio-Spectral Interferometry (FTSSI) for full spatio-temporal characterization of the UV pulse shaper (AOPDF).

2.2.1 Spatial characterization techniques

Shack-Hartmann wavefront sensor

One of the most common techniques of monochromatic beam wavefront characterization is Shack-Hartmann wavefront sensor [117, 118]. Figure 2.3 shows its typical configuration that consists of an array of lenslets of the same focal length and a 2D detector (CCD) placed at the focal plane of the lenslets. Each lenslet forms a focus spot at the detector from a particular portion of the test beam. If the test beam is collimated, the foci at the detector are equally separated from each other. Otherwise, when there exists an aberration which can be considered as a tilt in each sampled position of the beam, the foci will be displaced from the nominal position in the detector. The local tilts can be calculated from their corresponding displaced foci and hence reconstruct the test wavefront. At first glance Shack-Hartmann sensor seems not to be a practical device for wavefront measurement of the ultrashort pulses. Primarily

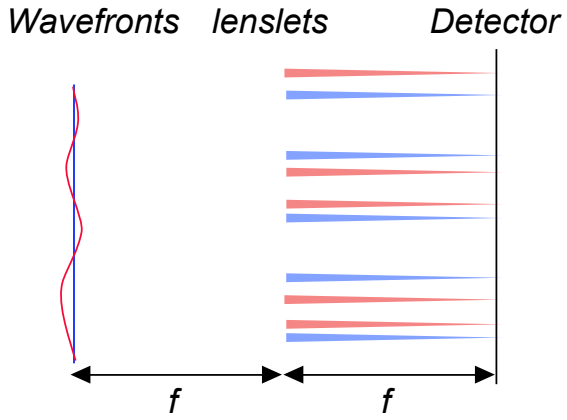

Figure 2.3: *Typical configuration of Shack-Hartmann wavefront sensor. Each lenslet forms a focus spot at the detector from a particular portion of the test beam. The detector is placed at the focal plane of the lenslets. In the case of being illuminated by a collimated beam, the foci are equally separated from each other. Otherwise, in the case of existence of an aberration, the foci will be displaced from the nominal positions on the detector from which the degree and type of the distortion can be calculated.*

because the focal length of the lenslets are wavelength dependent (chromatic aberration) that blurs the foci. Secondly, when there exists a space-time coupling, each spectral component has its own particular wavefront that yields multiple foci from a specific sampled portion of the beam. However, a separate wavefront measurement of each spectral component of the pulse may overcome the problem. It is accomplished by placing a sets of spectral filters and repeating the measurement for each of the spectrally filtered pulse components [119]. It is possibly even much easier by placing the Shack-Hartmann device in the imaging plane of a 2D spectrometer [120].

Spatial interferometry

Another technique that is widely used for characterization of the spatial phase of the beam wavefront is spatial interferometry. Analogous to the spectral interferometry, spatial interferometry is based on interfering the reference and the test beam with a small angle.[i] The relative spatial phase can be extracted from recorded interference pattern by means of different techniques [121] among which, the Fourier filtering [86] is the most established one. It should be mentioned that the production of the well characterized reference beam is much easier in spatial than spectral domain because

i. The relative angle between two beams is the counterpart of the relative temporal delay in the spectral domain that is necessary for filtering the interfering term in the Fourier filtering algorithm. Furthermore, it removes the spatial phase sign ambiguity which is due to the symmetry of the interaction of the collinear geometry.

the reference beam can be easily made from the test pulse itself. As an example, the reference beam can be achieved by selecting a small section of the wavefront by placing a pinhole in front of the test beam and forming a well defined spherical wavefront. In fact this is the base of Point Diffraction Interferometry (PDI) [122] that is one of the simplest and most applied method among the spatial interferometry techniques.
Although a spatial interferometer is only convenient for wavefront characterization, its modified version can be used for characterization of the pulse front tilt [123]. In the modified version, analogous to conventional spatial interferometry, two beams with a small relative angle are combined and sent to the 2D detector with an exception that the beams are spatially reversed with respect to each other. In a standard geometry where two replicas are combined without any modification, the pulse front tilt can not be detected. This is because the delay between two pulses remains constant at each position along the beam [see Fig. 2.4 (a)]. However, the situation changes when one of the beams is spatially reversed with respect to the other one. In this case [Fig. 2.4 (b)], the pulse front tilt forces the delay between two pulses to be spatial position dependent (position along the beam). Figure 2.4 shows the relevant setup used by Pretzler and his colleagues for detection of the pulse front tilt [123]. Because of using of reversed spatial interferometry the spatial position dependent delay resulted in an inhomogeneous spatial interference. They calculated the value of the pulse front tilt from the contrast of the interference fringes [see Fig. 2.4 (c)].
An alternative way of space-time couplings characterization is combining the spectral phase measurement techniques with the spatial interferometers. The spatial interferometer measures the spatial phase of the each spectral component of the pulse by spectrally filtering and interfering them with the original pulse. In this case, the phase function is not measured versus frequency. An additional spectral phase measurement at a location where all spectral components are present yields the spatio-temporal phase of the pulse [124]. However, the main drawback of this technique appears in the case of existence of a strong spatial chirp, because spectral components are spatially chirped and it is impossible to find a location to perform the spectral phase measurement where the whole spectrum of the pulse is present.

Spatial shearing interferometry

Spatial shearing interferometry, which is the counterpart of spectral shearing interferometry in spatial domain, consists of interfering the test monochromatic beam with its slightly spatially displaced replica. In fact, it is the spectral shearing interferometry

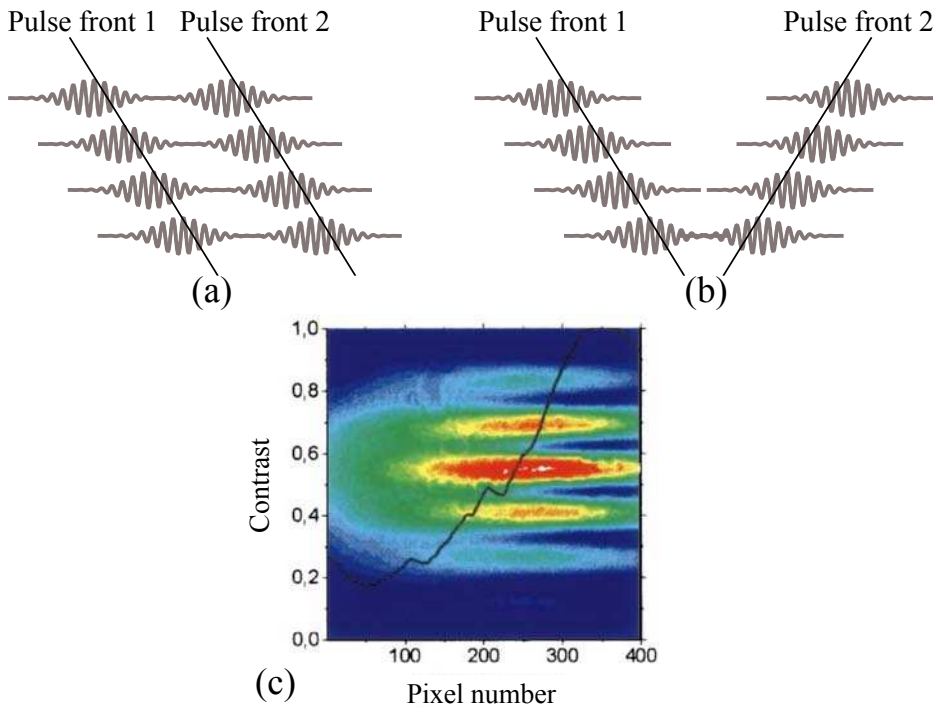

Figure 2.4: *Pulse front tilt measurement using reversal spatial interferometry. Spatial interferometry is insensitive to the pulse front tilt (a) unless one of the arms is reversed with respect to the other one (b). In this case, different spatial positions of the pulse front will experience different delays depending on the strength of the pulse front tilt (c). This results in detection of an inhomogeneous spatial interference from which the value of pulse front tilt can be calculated. This figure is adopted from [123].*

that is inspired by spatial shearing interferometry. Despite the conventional interferometry where the recorded interference signal yields the phase difference between test and reference beam, here, the phase at one position of the test beam wavefront is referenced to the phase of the other position of the same beam wavefront (similar to spectral shearing interferometry). Existence of small angle between two sheared replicas is necessary if one desires to apply the Fourier filtering to the recorded signal to extract the phase difference. After performing of Fourier filtering process, the reconstruction of the spatial phase is done by integration or concatenation that was explained in the previous chapter in spectral shearing interferometry section. The issue of performing the spatial shearing has led to the development of different types of the spatial shearing interferometers among which the Lateral Shearing Interferometry (LSI) is the most common one [93, 94]. The LSI is based on interfering the test beam with its replica that is spatially sheared along one of the spatial axis of the beam wavefront y or x [see Fig. 2.5]. This yields the finite phase difference $\phi(x+dx, y) - \phi(x, y)$,

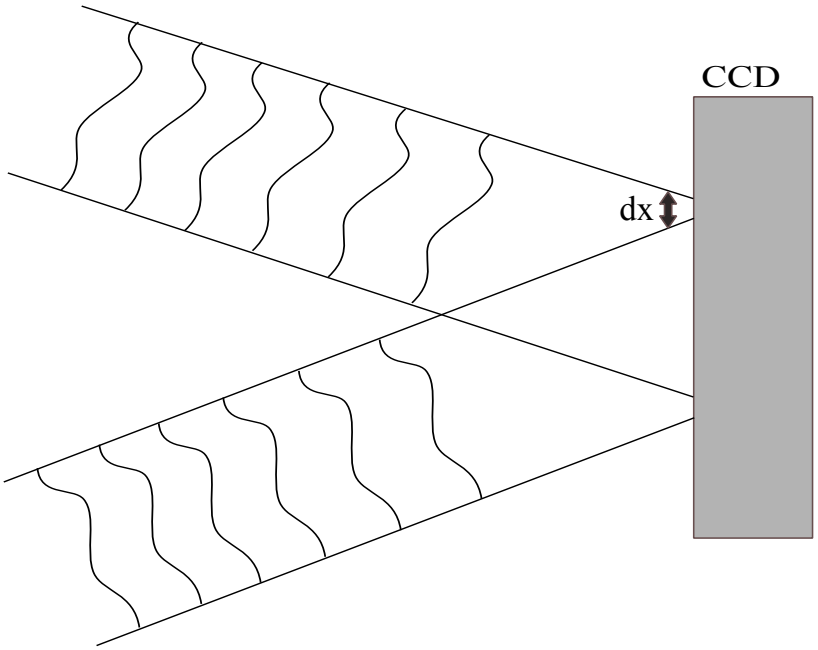

Figure 2.5: *Schematic configuration of a lateral shearing interferometer. It is based on interfering the test beam with its replica that is slightly shifted along the x axis. A small relative angle between two arms enables the application of the Fourier filtering process to extract the spatial phase value $\phi(x)$.*

from which the spatial phase $\phi(x, y)$ can be extracted by an integration along x axis. However, the integration yields an unknown function of $f(y)$ which comes from the constant of integration of each line. Therefore, in order to completely characterize the spatial phase, an additional shearing along the orthogonal direction is required [125]. In lateral shearing, the two wavefronts do not overlap completely which means this technique can not recover the spatial phase of the whole beam wavefront. Therefore other type of interferometer has been developed called Radial Shearing Interferometer (RSI) in which, two identical arms of the interferometer are combined with a slightly different magnifications m [126]. This yields $\phi(mr, \theta) - \phi(r, \theta)$ from which one can extract the full 2D spatial phase of the beam by integrating along the radial lines. r and θ are the radial and the angular coordinates respectively. This integration does not yield any ambiguity that is present in one dimensional lateral shearing interferometry because all the integrations have a common origin that is the central point of the beam.

Spatial shearing interferometers are proper devices for spatially characterizing the monochromatic beams; nevertheless, they can be applied to measure the spatial phase of each spectral component of the ultrashort pulses obviously by spectrally resolving

the interference pattern [127]. They can be also added to the temporal pulse characterization techniques e.g. SPIDER, and hence construct the space–time metrology devices that are able to measure the space-time coupling effects of the pulses [128,129].

2.2.2 Incomplete space-time coupling measurement techniques

2D imaging spectrometer (detection of spatial chirp)

The spatial chirp is one of the easiest measurable types of space-time couplings. In order to measure it, the spatio-spectral intensity profile of the pulse is required. This can be easily measured by means of a 2D imaging spectrometer. The 2D spectrometer is an extension of a conventional spectrometer that measures the intensity trace of $I(\omega, x)$ by selecting a slice of the beam wavefront and spectrally resolving different points of the mentioned slice on to different rows of the 2D-detector. The linear spatial chirp appears as a tilt in the spatio-spectral intensity profile. Gu and his coworkers were the first who measured quantitatively the spatial chirp using a 2D imaging spectrometer [105]. It should be noted that the aberrations in spectrometers can mimic the effect of spatial chirp. Therefore, a precise measurement of this coupling requires a 2D spectrometer free of any aberrations. In our lab, we have used a home-built aberration free 2D imaging spectrometer in the FTSSI setup. It has been also directly used to measure the spatial chirp of the shaped pulses. I will detail its design and properties in the experimental results section.

Single-shot autocorrelator (detection of pulse front tilt)

Single shot autocorrelators can be applied for detection of the pulse front tilt just under a condition that one of the interferometer arms is spatially reversed [130] with respect to the other one (basically because of the same reason that was explained in spatial interferometry). Assuming that the pulse front tilt occurs along the x axis and the pulses are combined in the $y-z$ plane, imposes each overlapped point along x to experience a different arrival time gap between the two beams. The interdependency between the generated second harmonic signals along x and y axis results in rotation of the detected elliptical trace with respect to the x axis on the detector. Raghuramaiah *et al.* [131] demonstrated a quantitative measurement of the pulse front tilt via measuring the rotation angle of the elliptical trace.

Single shot FROG variants (detection of spatial chirp and pulse front tilt) Single shot FROG variants can also measure some specific types of space-time couplings, e.g. spatial chirp and pulse front tilt. Conventional FROG variants can be transformed to the single shot geometry basically by following the same transforming procedure that is utilized for designing single shot autocorrelators: delay to transverse position mapping by crossing two arms at an angle and using a 2D detector. One of the simplest among the FROG variations is called single shot Second Harmonic Generation FROG (SHG-FROG) in which two beams are crossed with an angle on the second order nonlinear crystal [132]. As is the case for single shot autocorrelators, the cross angle causes that two pulses arrive with different delays with respect to each other on the crystal along the transverse dimension. In the cases where the space-time couplings are absent and the test pulse is transform limited, the recorded trace on the 2D detector will be a symmetrical elliptical trace where its major axes are parallel with spatial and spectral axes. However, in the presence of the spatial chirp, where the spectral components of the replicas are separated along the transverse dimension, each position of the cross section area will experience interaction of the pulses with different delays and different spectral components [see Fig. 2.6]. This results in detection of a tilted elliptical FROG trace from which the value of spatial chirp can be extracted [133]. Single shot SHG-FROG is not able to measure the pulse front tilt because any of the interferometer arms are not spatially reversed with respect to each other. Nonetheless, the simplest variation of FROG devices called GRENOUILLE (grating-eliminated no-nonsense observation of ultrafast incident laser light e-fields) [134] is able to detect pulse front tilt as well as spatial chirp [135]. Figure 2.7 depicts a schematic setup of GRENOUILLE where the detected signal at the camera is a single-shot SHG FROG trace with delay running horizontally and wavelength running vertically. It is similar to single shot FROG with some modifications to make the device more compact and user friendly. Similarly to single shot SHG-FROG, the presence of spatial chirp results in rotation of the elliptical GRENOUILLE signal trace on the camera from which its value can be extracted. Unlike single shot SHG-FROG, GRENOUILLE device can detect and hence measure the pulse front tilt that represents itself as a shift of the GRENOUILLE trace from the zero delay to a nonzero delay on the camera. In the absence of the pulse front tilt, two beamlets meet each other with zero relative delay at the central position of the crystal. However, in the presence of the pulse front tilt, because the arrival time of the pulse maximum intensity is position dependent, the position where two beamlets meet each other with

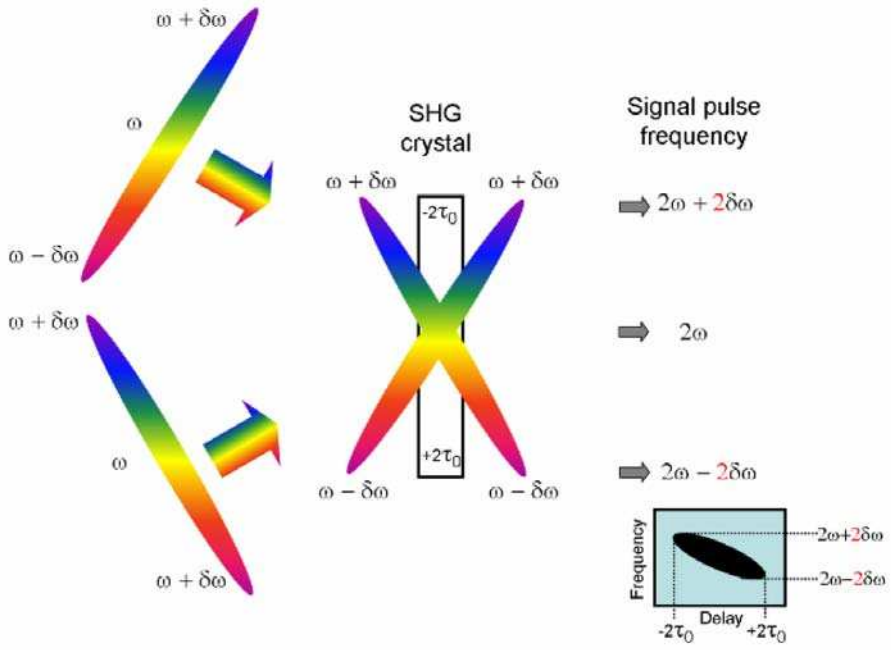

Figure 2.6: *Spatial chirp detection by a single shot SHG-FROG. In the presence of a spatial chirp (along the transverse dimension), each position of the cross section area experiences interaction of two pulses with different frequencies and delays. This results in a tilt in the detected elliptical FROG trace with respect to the major axis from which the value of the spatial chirp can be extracted. This figure is adopted from [133].*

zero delay will be shifted from central position of the crystal that yields the shifted GRENOUILLE trace. One can calculate the value of pulse front tilt from this displacement from the central position via the GRENOUILLE trace. The drawback of the single-shot FROG variants appears when the test pulse is contaminated with temporal chirp. The presence of temporal chirp also rotates the detected elliptical FROG traces in a similar manner to the spatial chirp. This makes it difficult to distinguish and hence measure them.

2.2.3 Full spatio-temporal characterization techniques

Fourier Transform Spatio-Spectral Interferometry (FTSSI)

Fourier-transform spectral interferometry technique was presented in the previous chapter (section 1.5.2) as a strong referenced pulse characterization technique. Since its operation requires one dimensional array, adding the second dimension simply by implementing a 2D detector (CCD camera) and a 2D imaging configuration, can be used to measure the spatially resolved spectral phase of the pulses. This is what we

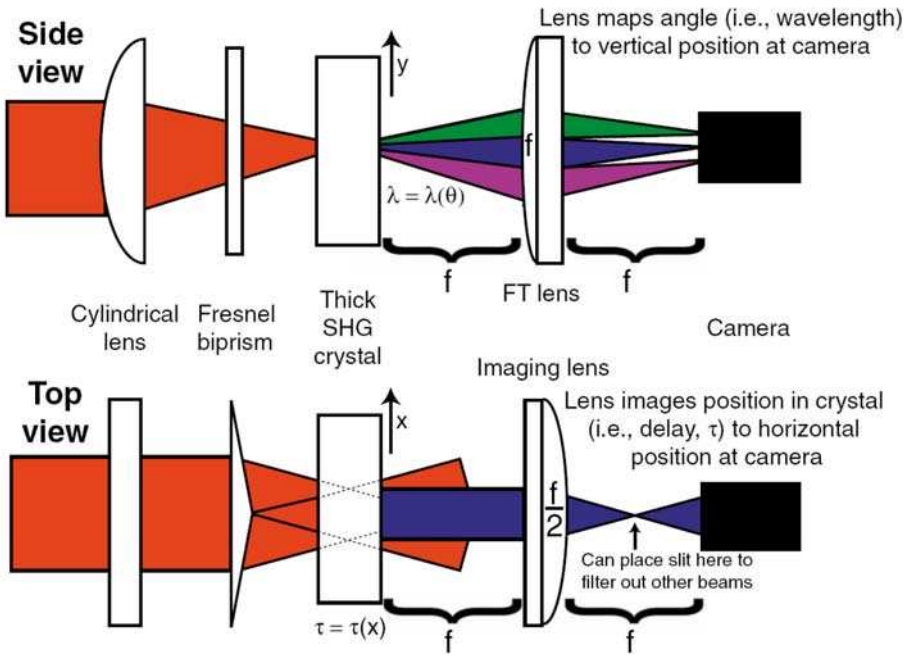

Figure 2.7: *Top and side view of GRENOUILLE. A Cylindrical lens focuses vertically the input beam on to a biprism. The biprism divides the incident beam into two beamlets and combines them with an angle in the horizontal plane. A thick SHG crystal resolves and maps the spectral components to different angles in the vertical plane. An additional cylindrical lens at the other side of the crystal maps the angularly dispersed components on to different positions of the camera in the vertical plane. The signal at the camera is therefore a single-shot SHG FROG trace with delay running horizontally and wavelength running vertically. This figure is adopted from [134].*

have used to spatio–temporally characterize the shaped pulses of the UV-AOPDF pulse shaper and I will present it in more detail in the following. Figure 2.8 (a) depicts a typical setup of a spatio-spectral interferometer in which the reference arm and the test pulse are combined collinearly with a relative delay at the entrance slit of a 2D imaging spectrometer. The imaging spectrometer selects one spatial slice of the overlapped beams. In this case, the spectrally resolved interfering electric field of different points along the beam slice y is recorded on different rows of the 2D camera. Therefore, the recorded signal reads

$$S(\omega, y) = |\widetilde{E}_r(\omega, y) + \widetilde{E}_s(\omega, y) \exp(i\omega\tau)|^2 \tag{2.1}$$

which corresponds to spatially resolved spectral interference intensity [see Fig. 2.8 (b)]. The relative spatio-spectral phase can be extracted by using the Fourier-transform filtering algorithm for each point y of the interference pattern [see Fig. 2.8 (c)]. In

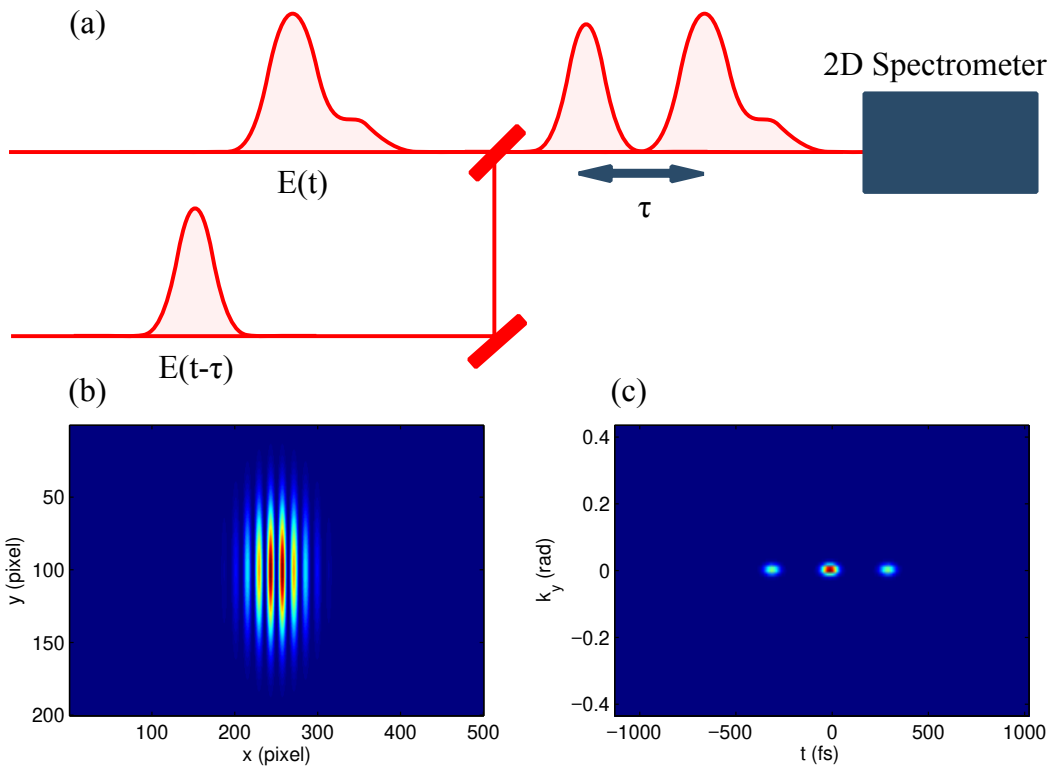

Figure 2.8: *Schematic configuration of a collinear spatio-spectral interferometer along with the detected signal. (a) The test and reference arm are combined collinearly with a relative delay at the entrance slit of a 2D spectrometer. (b) The 2D spectrometer records the spatially resolved intensity interference of two arms. (c) The recorded interference fringes correspond to three lobes separated from each other by the amount of the relative delay τ in quasi-temporal domain.*

order to reconstruct the spatio-spectral phase of the test pulse, the spatial and spectral phase of the reference arm should be already known. However, this task by itself is challenging because it requires a separate spatio-spectral pulse characterization technique. Having a reference pulse with spectral phase independent of its spatial transverse coordinate (space-time coupling free pulse) may ease the problem. In this case, by measuring the spectral phase at a chosen point y_0 that contains all spectral components $\phi_r(\omega, y_0)$, one can obtain the spatio-spectral phase $\phi_r(\omega, y) = \phi_r(\omega, y_0)$ and therefore the spatio-spectrally characterized reference pulse. This consideration, a spatially independent spectral phase, maybe achieved by putting a pinhole in front of the test pulse, choosing a specific point y_0 from the wavefront of the test pulse and collimating it by means of a lens. However, there are at least two constraints for this approach. First, when the test pulse spectrum is ultra broad, it is almost impossible to make a collimated beam where all spectral components have a plane wavefront.

Secondly, when the test pulse is strongly spatio-spectrally coupled, it is difficult to find a position which contains all the spectral components. Nonetheless, spatially resolved spectral interferometry can be considered as one of the strongest tools that spatio-spectrally characterize the pulses. Its applications includes studying lens aberrations [136, 137], self focusing effects of transparent media [138] and spatio-temporal speckles [34].

Figure 2.9 shows how FTSSI is capable of measuring different types of the space-time couplings. Figure 2.9(a) shows the effect of the spatial chirp on the spatio-spectral interference pattern. It appears as a tilt of the elliptical spatio-spectral intensity pattern with respect to the spectral axis. Figure 2.9 (b) shows effect of pulse front tilt on the recorded interference pattern. The spectral fringe frequency $\delta\omega_{fr} \propto 1/\tau$ depends on the relative delay of two arms τ. In the presence of pulse front tilt along the entrance slit (vertical plane), the delay between two arms become position dependent. In more detail, each point along the slit in addition to fixed relative delay τ, also experiences different arriving times of the beams due to the tilt of the test arm with respect to the reference arm. The arrival time of this position dependent pulse tilts the interference fringe pattern, depending on the magnitude of the pulse front tilt, with respect to the vertical axis.

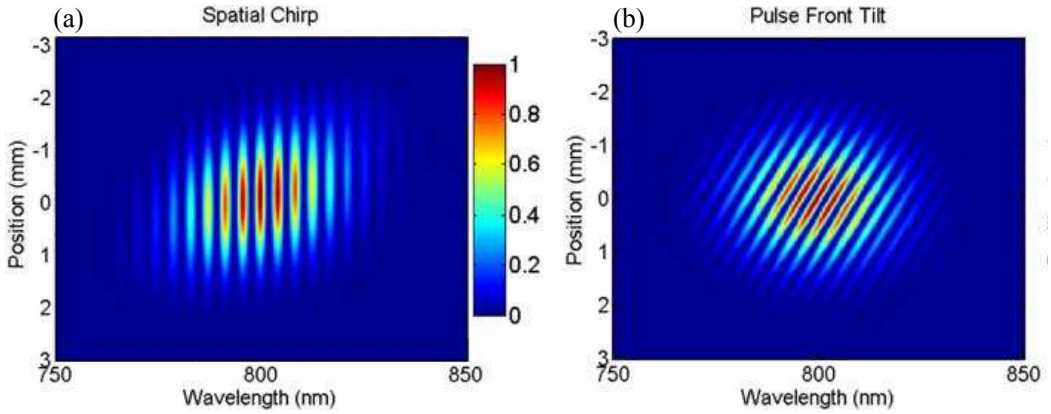

Figure 2.9: *Spatially resolved interferograms of a spatio-spectral interferometer in the case of combination of a transform limited reference pulse with a spatio-temporally coupled test pulse. The presence of spatial chirp (a) tilts the elliptical spatio-spectral intensity pattern with respect to the spectral axis; while, the presence of the pulse front tilt (b) results in rotation of the interference fringe pattern. This figure is adopted from [106].*

The spatio-spectral phase can be extracted by means of a Fourier filtering algorithm similar to the one dimensional spectral interferometry. However, as was mentioned in the presentation of Spectral Interferometry in the first chapter, using Fourier filtering

algorithms demands a spectrometer with higher resolution than it is normally required for sampling the finest features of the spectrum signal. A solution to this problem is crossing the arms on the entrance slit of the spectrometer with a small angle θ. This results in appearance of the spatial interference pattern where its frequency is proportional to θ. Figure 2.10 (a) shows the recorded signal on the detector that reads

$$S(\omega, y) = |\widetilde{E}_r(\omega, y) + \widetilde{E}_s(\omega, y) \exp(ik_y y + i\omega\tau)|^2 \tag{2.2}$$

where, k_y is the difference between transverse components of the propagation vectors k and related to crossing angle θ through

$$k_y = k \sin\theta. \tag{2.3}$$

Now, performing a two-dimensional Fourier transform along both the spectral and spatial axes yields three lobes. Here, in addition to the temporal separation the lobes are also separated along the quasi-spatial frequency dimension [see Fig. 2.10 (b)]. This means that the interfering term can be easily filtered without necessity of introduction of a relative delay. This approach therefore eases the spectral resolution requirement of the spectral interferometry. Depending on what the measurement re-

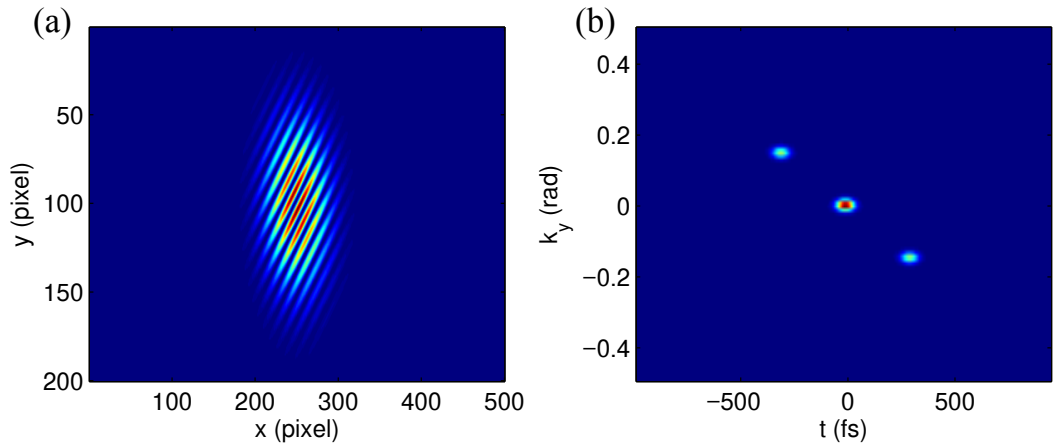

Figure 2.10: *Homemade simulation of detected signal by a 2D spectrometer of a non-collinear spatio-spectral interferometer . (a) The 2D spectrometer records the spatially resolved interference of the transform limited reference and the test pulses with a relative delay and angle. (b) The recorded interference fringes correspond to three lobes that are separated from each other by the amount of the relative delay τ and angle θ in the wavenumber-temporal domains.*

quests, high spectral resolution or high spatial resolution, one can play with spatial and spectral resolution of the measurement by modifying the values of the relative

delay and relative angle. In more detail, the spectral resolution will be lost when the relative angle is zero and the interfering term is separated from the dc term just by relative delay or inverse, the spatial resolution is lost when the relative delay is zero.

SEA TADPOLE

To overcome the problem of compromise between spatial and spectral resolution of the FTSSI, SEA TADPOLE Spatial encoded arrangement for Temporal Analysis by Dispersing a Pair of Light E-fields, can be used [139, 140]. In this method two pulses are combined by using of two monomode equal-length optical fibers [see Fig. 2.11]. In more detail, the reference arm is coupled into one of the fibers and the second fiber

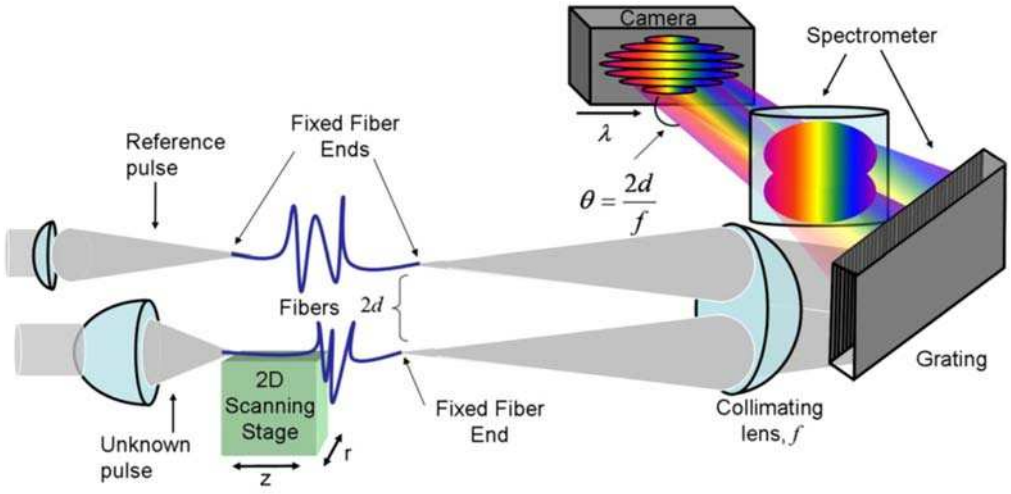

Figure 2.11: *Schematic configuration of the SEA-TADPOLE. A reference pulse and an unknown pulse are coupled into two single-mode fibers with approximately equal lengths. At the other end of the fibers, the diverging beams are collimated using a spherical lens (f). After propagating a distance f, the collimated beams cross and interfere, and a camera is placed at this point to record the interference. In the other dimension, a grating and a cylindrical lens map wavelength onto the camera's horizontal axis x. This figure is adopted from [106].*

selects a specific point from the unknown pulse. Then the emerging beams from the fibers are crossed in the vertical plane with an angle which results in spatial fringes. Leading the fringe pattern to the 2D imaging spectrometer results in spectrally resolving the spatial fringes. In this case, the delay between two pulses are set to zero. Since Fourier filtering algorithm filters the trace in the spatial coordinate, the spectral resolution of the measurement is kept untouched. Scanning the fiber transversely yields the spatially resolved spectral phase of the unknown pulse. Therefore, in this technique the spatial resolution is defined by the mode size of the fiber. SEA TAD-

POLE is a strong measurement tool for measurement of the spatio-spectral phase of the tightly focused pulse giving that the mode size of the fiber is several times smaller than the size of the focus. However the challenging issue concerning this technique is the calibration of the relative delay between the two arms, because transversely scanning the fiber also introduces longitudinal fluctuation.

SEA-SPIDER

All above mentioned devices are referenced measurement techniques. Similar to Spectral interferometry that is extended to measure the additional spatial domain by using of a 2D imaging spectrometer, spectral shearing interferometry also can be extended to spatio-spectral phase measurement device. SEA-SPIDER, Spatial Encoded Arrangement SPIDER [141] is the name of the developed device for spatio-spectral measurement of the pulses. In this technique, a 2D imaging spectrometer is implemented instead of non imaging spectrometer. Moreover, two spectrally sheared replicas, instead of being temporally delayed, are combined with an angle in to the imaging spectrometer. In this case, spatial fringes are produced instead of spectral fringes that relax the spectral resolution of the spectrometer through the Fourier filtering algorithm as explained before. Furthermore, using an imaging spectrometer gives the possibility of measuring the spectral phase at each point along the unknown pulse wavefront. However, SEA-SPIDER is a self referenced technique that does not retrieve the group delay of the unknown pulse. This means that the spatially dependent group delay of the pulse (spatial phase) remains unknown. Nonetheless, it reveals interesting signatures of spatio-spectral coupling of the pulses. One can encompass this problem by applying both spatial and spectral shearing simultaneously. This is called 2D shearing interferometry [129] in which two spectrally sheared replicas of the pulse are combined by a small angle with additional spatial displacement. Spatial and spectral phase can be separately extracted via Fourier filtering algorithm and then stitched together to retrieve a complete spatio-spectral characterization of the pulse.

STRIPED-FISH

So far, because of applying 2D detectors, all mentioned spatio-spectral characterization techniques are limited at best to measure spatio-spectral phase of the pulses $\phi(y, \omega)$ where the information about the other spatial dimension is lost. Fortunately, in most cases the generated spatio-spectral couplings occur only between one spatial and spectral (temporal) dependence of the pulse electric field. Therefore, the

loss of one spatial dimension is acceptable. However, some fields require the whole spatio-spectral characterization of the pulses $\phi(x, y, \omega)$. 2D SPIDER and SSI technique can adopt themselves to 3D measurement by scanning the entrance slit of the spectrometer. This requires a multishot measurement which is not always desired due to its several constraints. A different approach is STRIPED-FISH [142, 143], a form of Fourier-transform interferometry with a spatial carrier. In this technique, the test and reference beams pass through a coarse grating, which produces many diffracted orders. These diffracted orders then pass through an interference filter. Since each order has a slightly different wave-vector and the passband of the filter is angularly dependent, the passband frequency seen by each order is different. Each order therefore contains a quasi-monochromatic spatially encoded interferogram, and these are simultaneously recorded on a two-dimensional detector. Combining the interferograms yields a three-dimensional dataset. However the spectral resolution of the reconstructed electric field is reduced.

2.3 Experimental results

Here, I focus on studying spatio-temporal coupling effects produced by the UV-AOPDF pulse shaper which has led to a recent publication [61]. I apply the FTSSI as a measurement technique because it is capable of measuring the spatio-temporal characteristics of unknown pulses in all spectral regions. Moreover, it is highly sensitive to weak signals due to its linear measurement nature. In the following, before detailing the experimental setup, some hints are given on designing of our home-built 2D imaging spectrometer which can affect the accuracy and precision of the measurements.

2.3.1 Spectrometer design, calibration and characteristics

I have applied a home-built 2D imaging spectrometer in our FTSSI setup which is an extension of the conventional Czerny-–Turner imaging spectrometer. Figure 2.12 shows notations and the basis of a conventional Czerny-–Turner spectrometer which is in fact based on a 4f configuration. In this configuration, the entrance slit S, the plane grating G and the 2D detector D are located in the focal planes of the spherical mirrors. The first spherical mirror C collects and collimates the divergent wavefront from the entrance input slit. The diffraction grating disperses angularly the spectral components of the collimated beam. The second spherical mirror F focuses the spec-

tral components on the 2D detector placed at its focal plane. In order to measure

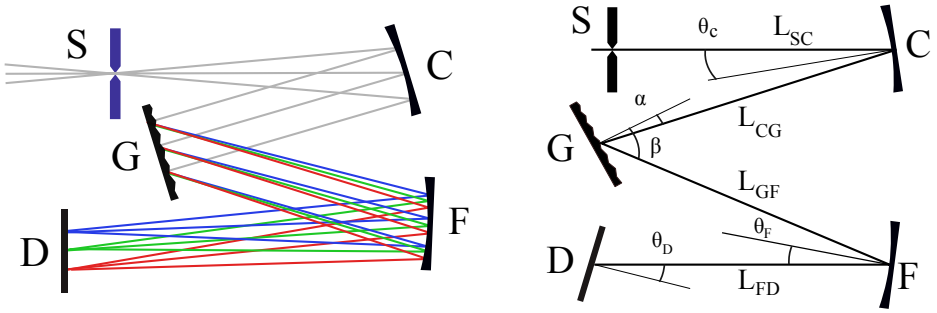

Figure 2.12: *Configuration of Czerny-Turner spectrometer:entrance slit S, slit to collimating mirror length L_{SC}, spherical collimating mirror C with angle of incidence in tangential plane θ_C and radius R_C, collimating mirror to grating distance L_{CG}, grating G with angles of incidence α and diffraction β, grating to focusing mirror distance L_{GF}, spherical focusing mirror F with angle of incidence in tangential plane θ_F and radius R_F, focusing mirror to detector distance L_{FD}, and detector D angled $\theta_D$to beam.*

the characteristics of the ultrashort pulses with large spectral bandwidth, imaging spectrometers ought to have a high quality image over a broad spectrum. However, since the spherical mirrors have a different focal length for tangential and saggital planes in the off-axis reflection configuration, the produced image of the entrance slit along tangential plane occurs before the saggital plane (zeroth order astigmatism). There also exists first order astigmatism which is due to the wavelength dependence of the diffraction angle of the grating $\beta(\lambda)$. In more detail, $\beta(\lambda)$ causes the incident angle on the focusing mirror F to be also wavelength dependent. Furthermore, the incident point of the optical ray on the focusing mirror will be also wavelength dependent which results in wavelength dependent tangential and saggital imaging planes. In order to correct the zeroth and first order astigmatism and hence obtain stigmatic images two conditions should be fulfilled. First, for a specific wavelength, the distances of the tangential and saggital images from the focusing mirror should be the same $S_T(\lambda_0) = S_S(\lambda_0)$ (correction of the zeroth order astigmatism). Secondly, both tangential and saggital image distances should change at the same rate as the distance between the focusing mirror and the detector changes $\frac{\partial S_T}{\partial \lambda} = \frac{\partial S_S}{\partial \lambda} = \frac{\partial L_{DF}}{\partial \lambda}$ (correction of the first order astigmatism). The zeroth order astigmatism can be corrected by reducing the distance between the input entrance slit and the collimating mirror L_{SC}. Under such conditions, the grating is under a divergent illumination and its diffraction in the tangential plane introduces an astigmatism that compensates the astigmatism that is introduced by the spherical mirrors. The first order astigmatisms can be corrected by different approaches such as implementation of non spherical (toroidal)

Parameter	Value
Central wavelength	270 nm
R_C	300 nm
R_F	300 nm
θ_C	5°
θ_F	8°
α	-4°
Γ	600 mm^{-1}
β	24.2°

Table 2.2: *Basic parameters of the 2D imaging spectrometer.*

mirrors [144] or aplanar (cylindrical) grating [145]. Austin *et al.* [146] showed a simpler technique that does not require the replacement of the optical elements. It was only based on modification of optical elements angles and distances with respect to each other. In more detail, the angle of the detector in the tangential plane θ_D, and the distance from the grating to the focusing mirror of the spectrometer L_{GF}, would compensate the astigmatism for a broad spectral bandwidth. The design of our homemade spectrometer which is done in collaboration with Oxford university is based on divergent illumination and the modifications detailed in [146].

Design

Designing of a 2D imaging spectrometer requires all parameters (e.g. inter-component distances, incident angles and the properties of each optical components) to be known. In our case, the given parameters are mirror radii, incident angles on grating and mirrors [see Tab. 2.2]. The slit image distance along tangential S_T and saggital S_S planes from the focusing mirror are calculated from the imaging equations of each individual optical components. Setting equal S_T and S_S, zeroth order astigmatism correction condition, yields the distance between the slit and the collimating mirror L_{SC}. The detector distance from the focusing mirror L_{DF} is then computed from setting it equal to the imaging distances. The condition for first order astigmatism

correction is obtained by setting equal the wavelength dependent variation of both the saggital and the tangential slit image and the detector distances from the focusing mirror $\frac{\partial S_T}{\partial \lambda} = \frac{\partial S_S}{\partial \lambda} = \frac{\partial L_{DF}}{\partial \lambda}$. It yields the detector angle θ_D and the distance between grating and the focusing mirror L_{GF}. Figure 2.13 shows the layout of our astigmatism free 2D-imaging spectrometer that is built in Oxford considering the parameters of Tab. 2.2. Two planar mirrors are additionally implemented between the collimating mirror and the grating and also between the focusing mirror and the detector to provide enough room for the mounts.

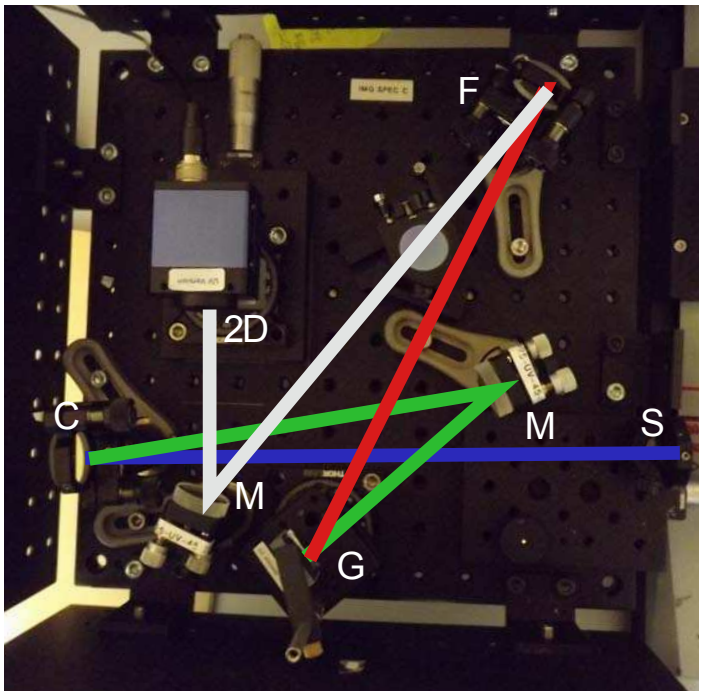

Figure 2.13: *Layout of home-built 2D imaging spectrometer. entrance slit S, collimating mirror C, planar mirror M, grating G, focusing mirror F, 2D detector 2D.*

Calibration

In order to use the spectrometer, we should know the dispersion relation on the detector ($\omega = \alpha x$) or in other words, find the relationship between each pixel on the detector and the corresponding spectral component of the input pulse. We make several narrow bandwidth holes on different spectral regions of the pulse using the calibrated AOPDF pulse shaper and record the diffracted beam with our imaging spectrometer. By computing the pixel indexes corresponding to the spectral amplitude holes we work out the variable α. Once α is calculated, we can perform the pixel to wavelength mapping. However, an important fact that should be mentioned

is that our spectrometer is only corrected for astigmatism and there still exists a distortion aberration. In more detail, each recorded spectral component on the detector is a curved line instead of being a straight line. This effect is more visible using a mercury—argon calibration lamp as an input beam. In Fig. 2.14(a) we can see the curvature of the spectral line. In the presence of the distortion, since each column on the detector x_n does not correspond to a specific spectral component ω_n, the pixel-to-wavelength mapping should be reconsidered. This is done by measuring the curvature of the spectral line and redoing the mapping process by taking it into account.

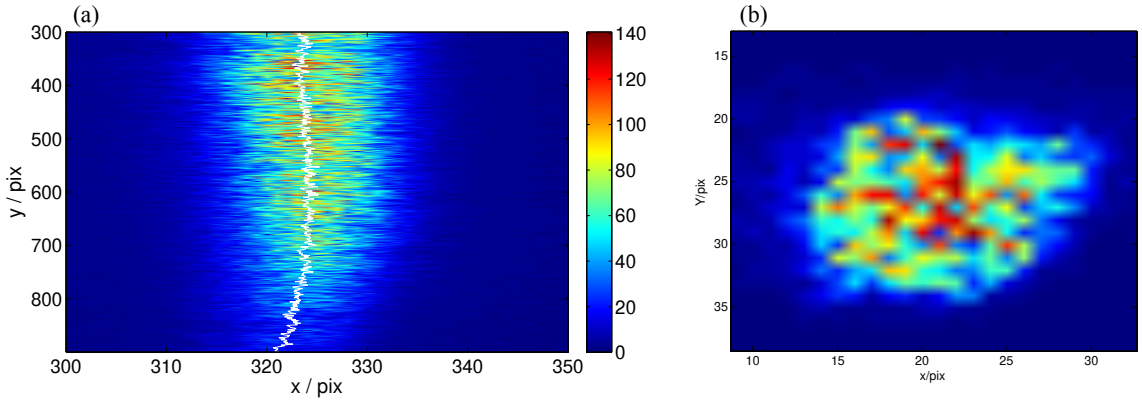

Figure 2.14: *Specific spectral intensity of a mercury-argon calibration lamp. (a) White line is the intensity average of each position along the spectrometer slit y and shows the curvature of the line for a specific wavelength. (b) Intensity distribution of the mercury-argon lamp is recorded by CCD camera using a 25 μm diameter pinhole in the entrance of the spectrometer. It reveals the spatial and spectral resolution of the spectrometer.*

Resolution

The spatio-spectral resolution of the spectrometer is measured by replacing the entrance slit with a 25 μm diameter pinhole and illuminating the spectrometer with a mercury–argon calibration lamp. Figure 2.14(b) shows the imaged spot on the 2D-detector. The detector is a CCD camera (EHD Imaging UK-1158UV) with a pixel size of 6.45 μm. The spatial resolution is 40 μm which is obtained by measuring the size of spot at FWHM along the y axis. The spectral resolution is 0.08 nm which is measured by $\frac{\Delta\lambda}{\Delta x} \times \delta x$ where, $\Delta\lambda$ is the wavelength separation of two spectral lines of the calibration lamp, Δx is their corresponding pixel separation and δx is the width of specific wavelength along the x axis.

2.3.2 Experimental Setup

The first step towards space-time characterization of shaped UV pulses is their generation from our CPA Ti:Sapphire laser source. I have already detailed our experimental setup for the generation of such pulses in the third section of first chapter [see section 1.3]. For more convenience, I just repeat the main characteristics of the generated pulses. The generated ultrashort UV pulses are centered at 267 nm with spectral bandwidth of 2 nm at FWHM and energy of 2 μJ. The repetition rate is 1 kHz and the beam diameter is around 2 mm. The generated pulse duration is around 150 fs. The next step, as soon as UV pulses are generated, is performing a FTSSI measurement. Therefore, the UV source is divided into reference and sample arms by means of a beam splitter with ratio of 30:70 respectively. Figure 2.15 depicts the layout of our FTSSI setup where the AOPDF is placed in the sample arm of the interferometer. The KDP crystal of the pulse shaper is cut in such way that requires the incident beam to be vertically polarized to satisfy the phase matching condition. According to Fig. 2.16 the pulse shaper output consists of diffracted and nondiffracted beam that are exiting with different angles. The crystal diffracts the incident beam by approximately 2.4°, while the nondiffracted beam leaves the device at around 2° with respect to the direction of the input beam. Since it is only the diffracted beam that delivers the desired shaped pulses we have isolated them by blocking the nondiffracted beam.

In practice, two important AOPDF adjustments provide an efficient and correct performance:
- The first one is the alignment of the beam within the AOPDF which consists of input beam height, collimation, incident angle and incident location on the AOPDF pulse shaper. The input beam collimation yields the best spectral resolution for the pulse shaper. Moreover it should be horizontal meaning that its height should stay unchanged within the pulse shaper. This is particularly important because we have a long crystal with typical length of 75 mm. If the input beam is well centered in the crystal its efficiency will be improved. The central position is found by mounting the pulse shaper on a translation stage and laterally displacing it in front of the input beam until the maximum energy is achieved for the output diffracted beam. The final step is finding the best incident angle of the input beam on the pulse shaper. In fact, the phase matching condition of the pulse shaper crystal (KDP) for each spectral component is strongly dependent on the incident beam angle. The pulse shaper is designed in such a way that the phase matching condition is fulfilled only when the

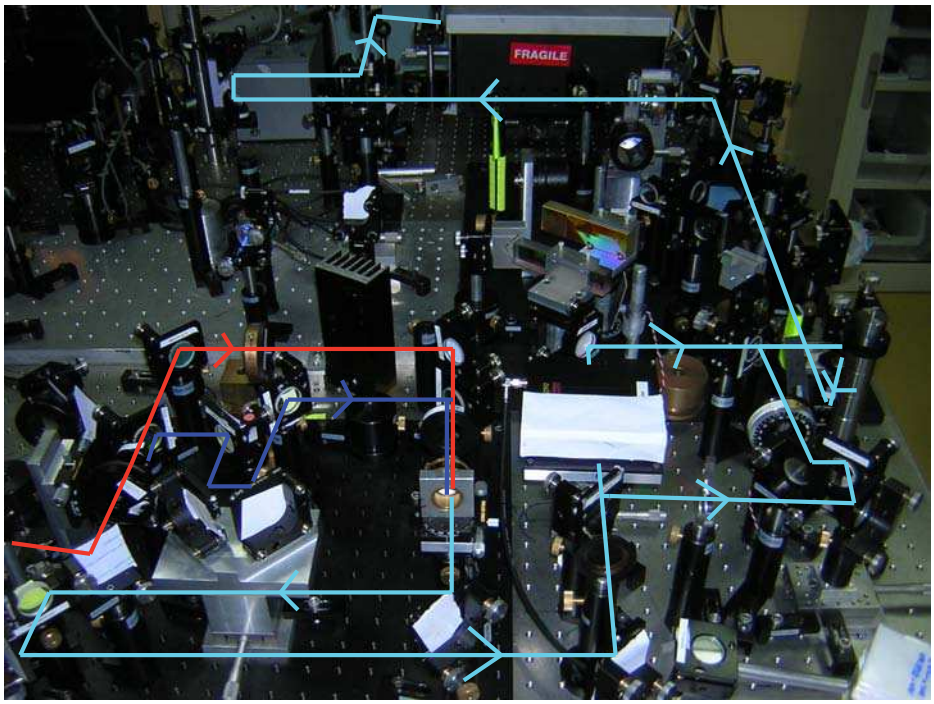

Figure 2.15: *Layout of experimental setup. Ultrashort UV pulses (blue line) centered at 267 nm is generated from sum frequency of the laser source (red line) and its second harmonic generation (violet line) in a type1-BBO crystal. The UV pulse is divided into reference and test arms by means of a beam splitter. The emerged beam from the UV-AOPDF (diffracted shaped) is combined with the reference arm and directed to a 2D imaging spectrometer. The polarization of the reference arm is rotated to be parallel with the diffracted sample arm by means of half wave-plate. The wave-front of both beams are rotated by 90° by a twisted periscope to make the spatio-temporal coupling axis along the entrance slit of the spectrometer.*

incident beam is normal to the KDP crystal. In order to be sure about the best angle, we program a narrow bandwidth hole at a specific wavelength of the shaped pulse and record it with a spectrometer. This is easily done by programming the acoustic wave in such way that the diffraction does not occur at those desired wavelengths. When the input beam is not normal, the hole on the spectrum appears at a different wavelength than the programmed one. Rotating the crystal, spectrally shifts the location of the hole and hence one can find a condition in which the hole appears at the same wavelength than it is programmed. In this case the phase matching condition is fulfilled and the pulse shaper is well aligned.

- The second adjustment concerns the time delay between the acoustic wave and the optical beam in the KDP crystal. The acoustic wave is seen frozen by the optical beam due to their propagation speed difference in the crystal. However, it is not stationary

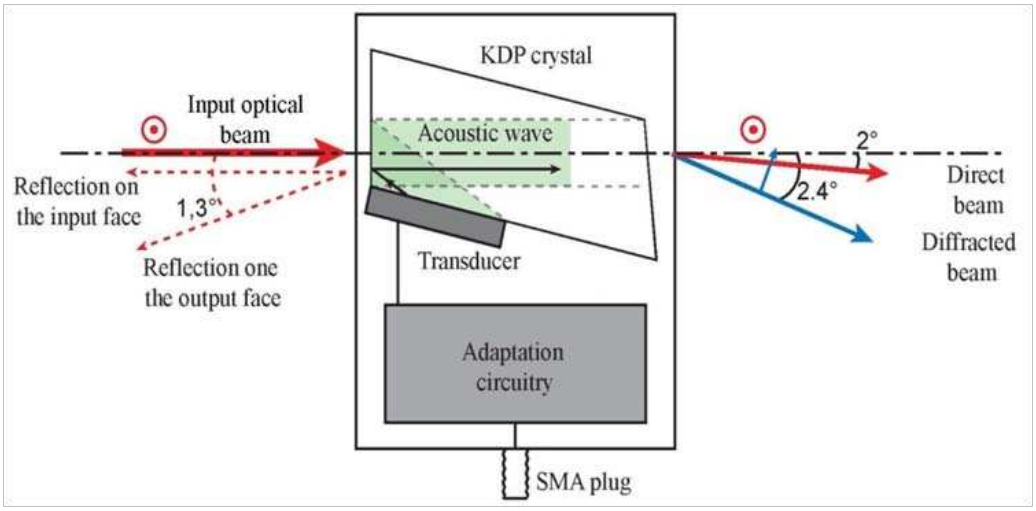

Figure 2.16: *Schematic view of our UV-AOPDF pulse shaper. The pulse shaper diffracts the incident beam by approximately 2.4°, while the nondiffracted beam leaves the device at around 2° with respect to the direction of the input beam. The reflected beam has an angle of approximately 1.3 ° with respect to the direction of input beam.*

and hence its generation rate and propagation in the crystal should be synchronized with the optical beam. The generation rate should of course posses the same repetition rate as the optical source (1kHz for our laser source). The arriving time of the acoustic wave inside the crystal with respect to the optical beam should be synchronized in a way that all its spectral components can be diffracted anywhere inside the crystal. This condition is fulfilled when the acoustic beam has already propagated to the middle of the crystal as the optical beam enters it. We use an electronic time delayer which synchronizes the acoustic wave with the preceding pulse. In order to be sure of the optimum relative delay, we tune it to find a condition where the incident pulse can be diffracted in all locations of the crystal with same efficiency.

The reference arm is combined with the output shaped beam of the sample arm with a small angle θ (in the vertical plane yz) and controllable relative delay τ at the entrance slit of the home-built imaging spectrometer [147]. The polarization of the output shaped pulse is orthogonal to the polarization of the reference beam, thus a half wave-plate is placed in the reference beam to provide a parallel polarization for both arms before their combination. Since the spectrometer employs a two dimensional detector, it performs a measurement of the spectrum for each spatial position y of the beam slice. However, there is no interest in performing a measurement along

this vertical axis, because all interesting spatio-temporal couplings occur in the horizontal plane (the plane on which diffraction occurs). Therefore, both reference and diffracted beam wave-fronts are rotated 90° by means of a twisted periscope. Finally, in order to increase the signal, a cylindrical mirror is placed before the entrance slit that focuses the beams on to the entrance slit along the horizontal plane xz (non imaged axis of the beam or in other words, along the insensitive axis of the beam to the spatio-temporal couplings). The combination of the reference and the sample

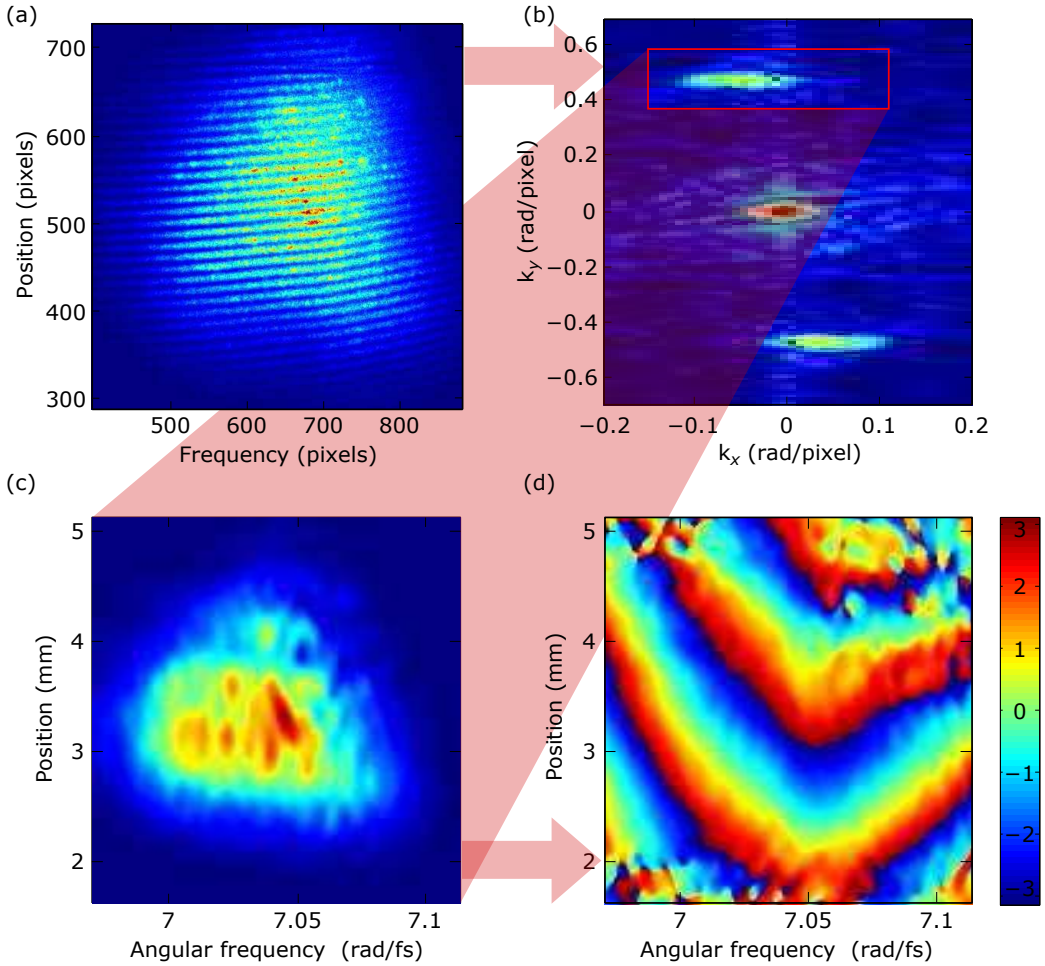

Figure 2.17: *The Fourier filtering process. (a) A raw interferogram measured by the spectrometer camera. (b) A two-dimensional Fourier transform is performed. An ac term is filtered out within the Fourier domain. (c) An inverse two-dimensional Fourier transform of this term isolates the final term of Eq. 2.4. The mapping onto calibrated frequency and position axes is calculated. (d) Extracted phase difference $\phi_s(x,\omega)-\phi_r(x,\omega)$, modulo 2π. A subsequent procedure calibrates the camera pixels into physical units of frequency and position.*

arm on the entrance slit results in the formation of a 2D interference pattern on the

spectrometer detector [see Fig. 2.17(a)] that reads

$$\begin{aligned} S(y,\omega) &= |A_s(y,\omega)e^{i\phi_s(y,\omega)} + A_r(y,\omega)e^{i[\phi_r(y,\omega)+\omega\tau+k_y y]}|^2 \\ &= |A_s(y,\omega)|^2 + |A_r(y,\omega)|^2 \\ &+ 2\,|A_s(y,\omega)|\,|A_r(y,\omega)|\cos\left[\omega\tau + k_y y + \phi_s(\omega,y) - \phi_r(\omega,y)\right]. \end{aligned} \tag{2.4}$$

Here, k_y is the difference between the transverse components of the propagation vectors (such that their subtended angle is $\theta = k_y/\mathbf{k}$). A_s, A_r, ϕ_s and ϕ_r denote the spatio-spectral amplitude and phase of the shaped (s) and reference (r) pulse respectively. The first two terms of the equation are the reference and sample intensities respectively and the third term shows the coupling of the sample and the reference amplitudes with their relative spatio-spectral phase. In order to reconstruct the spatio-spectral characteristics of the shaped pulse, we need to calculate the spatio-spectral amplitude and the phase of the shaped pulse. The amplitude is directly obtained by measuring the sample intensity on the spectrometer when the reference arm is blocked. The phase can be extracted from the third term of the above equation via different methods. We use the Fourier filtering algorithm [86] where the interferogram is Fourier transformed along both spatial and spectral dimensions [see Fig. 2.17(b)]. Then, one of the ac terms is filtered out and inverse Fourier transformed with the carrier frequency removed [see Fig. 2.17 (c)]. This isolates the final summand of Eq. 2.4, which contains the phase difference $\phi_s(y,\omega) - \phi_r(y,\omega)$. Finally, the spatio-spectral phase of the transmitted light is reconstructed [see Fig. 2.17(d)]. The full spatio-temporal electric field and intensity may thus be reconstructed by a further Fourier transform.

The spatial and spectral carriers, k_y and τ, are chosen in order to separate the ac and dc terms in the Fourier transform whilst ensuring that the fringe period is greater than the spectrometer resolution. In order to be able to handle complex temporal structure, a predominantly spatial carrier of $\theta \approx 3$ mrad and $\tau \approx 0$, giving rise to predominantly spatial fringes, is employed for these experiments.

Device calibration

The extracted phase $\Delta\phi(\omega)$ is the spectral phase difference between the reference and sample arm which consists of the added phase of the pulse shaper $\phi_{AO}(\omega)$ plus the intrinsic second and higher order phases associated with the two arms of the

interferometer $\phi_s(\omega)^{int}, \phi_r(\omega)^{int}$:

$$\Delta\phi(\omega) = \phi_s(\omega) - \phi_r(\omega) = \phi_{AO}(\omega) + [\phi_s(\omega)^{int} - \phi_r(\omega)^{int}]. \tag{2.5}$$

In order to measure the intrinsic higher order phases of the optical components and hence calibrate the measurement device, we take a FTSSI measurement with the AOPDF removed:

$$\Delta\phi_{rem}(\omega) = \phi_s(\omega)^{int} - \phi_r(\omega)^{int}. \tag{2.6}$$

Figure 2.18(a) shows the extracted relative spatio-spectral phase of two arms when the Dazzler is removed. The added intrinsic relative phase averaged over the spatial extent of the pulse is 600 fs^2 [see Fig. 2.18 (b)]. The error in the measurement of the second order phase is about 100 fs^2 which is estimated by computing the standard deviation of the inferred sample phase over 10 shots in the regions where the intensity is greater than 10% of the peak [see Fig. 2.18 (b)]. The significant sources of the

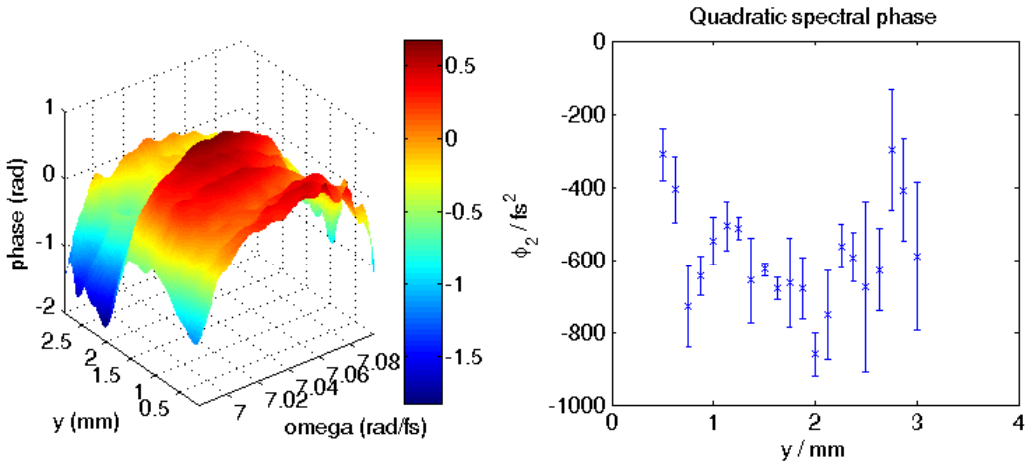

Figure 2.18: *Intrinsic dispersion of the delay line as a function of position and frequency. (a) The dispersion of the interferometer as a function of position and frequency averaged over ten shots. (b) The second order spectral phase at different positions along the beam wavefront. The added second order dispersion is approximately 600 fs^2 which is estimated from the averaging of the inferred phase along different spatial positions. The precision of the second order phase measurement is 100 fs^2 which is estimated by computing the standard deviation of the inferred sample phase over 10 shots in the regions where the intensity is greater than 10% of the peak. The variation of the spectral phase over extent of the pulse wavefront is less than 140 fs^2 that is estimated by computing the standard deviation of the inferred second order phase along the extent of the pulse.*

measured phase error are camera shot noise, shot-to-shot fluctuation of the UV source

Pulse shaper	$H(\omega)$
Pulse delay	$\exp\left[-2(\omega-\omega_0)^2/\Delta\omega^2 + i\omega\tau\right]$
N-pulse train	$\sum_n^N \exp(i\omega\tau_n)$
Chirps	$\exp\left[-2(\omega-\omega_0)^2/\Delta\omega^2 + i(\omega-\omega_0)^2\phi^{(2)}/2\right]$
π step	$\exp\left\{i\arctan\left[(\lambda-\lambda_0/\Delta\lambda_{step}\right]\right\}$

Table 2.3: *Transfer function, $H(\omega)$, for the pulse shapes presented within this section, where $\omega_0 = 2\pi c/\lambda_0\theta$ is the central angular frequency. For the pulse delay and chirped-pulse cases, a narrowed spectral bandwidth of $\Delta\lambda = (\lambda_0^2/2\pi c)\Delta\omega = 1$ nm was employed. All other parameters are defined in the text.*

and finally unwrapping and fitting in the phase extraction process. The error in the measurement of the reference amplitude depends also on the shot-to-shot fluctuation of the UV source and the camera noise. The signal-to-noise ratio at the peak of the signal is approximately 10 [ii]. The variation of the second order phase over the spatial extent of the pulse is less than 140 fs^2 [Fig. 2.18(b)].

2.3.3 Pulse shapes

In order to study the spatio-temporal coupling effects of the AOPDF pulse shape, we produce various of the most common pulse shapes used in quantum control experiments including pulse trains, chirped pulses and a π phase step. The mathematical expression of each desired transfer function is presented in Tab. 2.3.

Pulse delays

As a first experiment we produce different pulse delays (first order spectral phase). This is done by scanning the launched acoustic wave inside the KDP crystal that results in diffraction of the single pulse at different positions and hence generation of different pulse delays τ. Since the acoustic wave is tailored to compensate the natural dispersion induced by the KDP itself, the intensity bandwidth of the pulse is narrowed to 1 nm to reduce the length of the acoustic wave. This enables us to have a larger range of delays to be accessed without clipping the acoustic wave on the edge of the

ii. We only estimate the fluctuations of the reference amplitude and apply it for the sample arm. This is because, in order to have optimum fringe visibility, both arms are chosen in such a way that have approximately same intensities on the CCD camera.

crystal. Figure 2.19(a) depicts the measured delays induced by the pulse shaper with step size of 400 fs that are found to be in good agreement with the programmed delays within an error of 3% [see Fig. 2.19(b)]. Looking precisely at central position of the

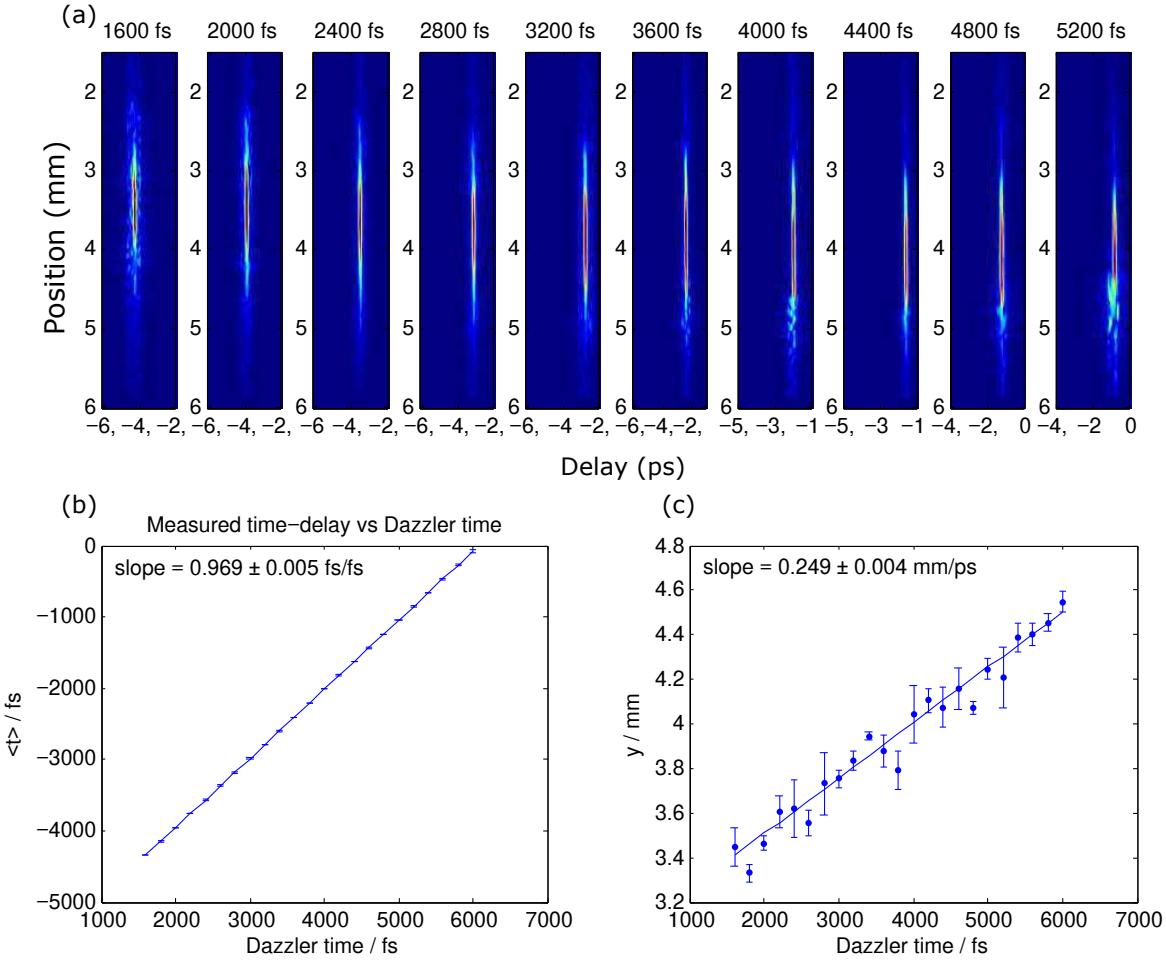

Figure 2.19: *Generation of different pulse delays with step size of 400 fs by scanning the acoustic wave inside the AOPDF crystal. (a) Reconstructed spatio-temporal intensity of the induced pulse delays. (b) Temporal arriving moments of the pulses as a function of programmed delays. It shows a good agreement between the induced and the programmed pulse delays with an error of 3%. (c) Central position of the diffracted pulses as a function of programmed delays. The central position of the diffracted pulses varies linearly with a coupling speed of 0.249 ±0.012 mm/ps.*

pulses at different delays shows that they vary linearly with a coupling speed of 0.249 ±0.012 mm/ps as a function of programmed delay [see Fig. 2.19(c)]. This behavior is also confirmed with a direct measurement of the beam position on a CCD camera. We also calculate the beam pointing angle $\theta \approx k_y/k$ as a function of the delays from the reconstructed wavenumber-temporal intensity $I(k_y, t)$. No angle variation is observed.

Therefore, as a conclusion there is only a single coupling effect which is the spatial variation of the central beam position as a function of the pulse delay.

Pulse trains

The second step is generation of pulse trains. According to the mathematical expression of the pulse trains presented in Tab. 2.3, we program various trains of pulses with different time gaps and varying numbers of pulses ranging from two to thirteen. A typical reconstructed spatio-temporal intensity distribution is shown in Fig. 2.20 for a train of three pulses separated by 1.5 ps. No spectral phase is added to the individual pulses. Once again, we narrow the bandwidth of the diffracted pulse. The pulse separation is verified to within 1%. A pronounced linear spatio-temporal

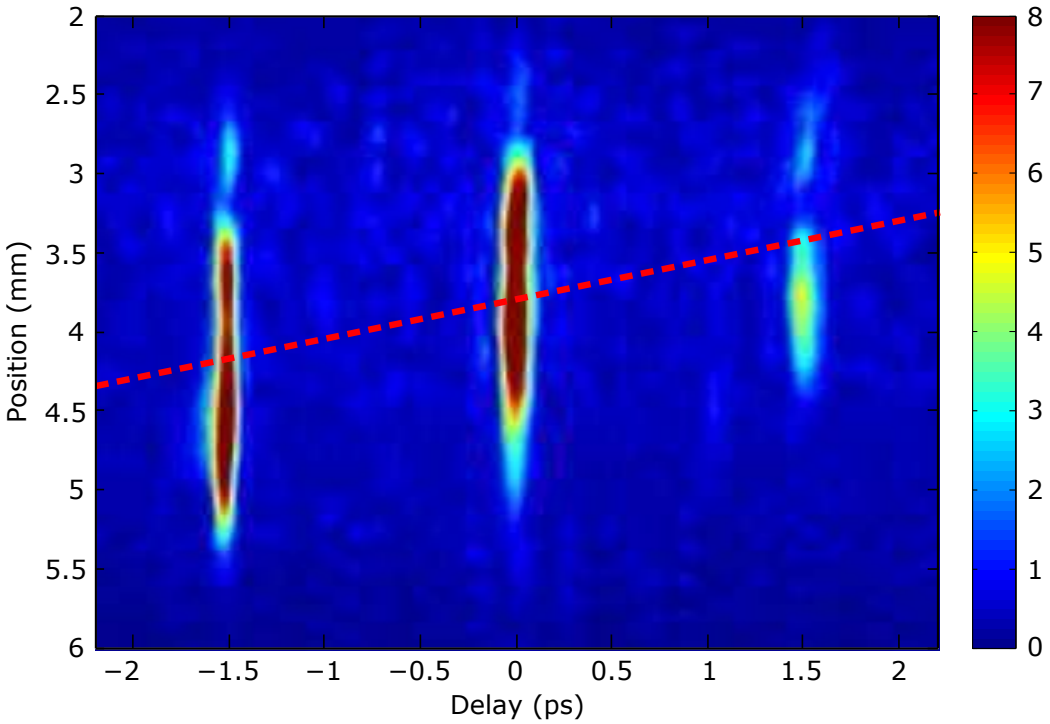

Figure 2.20: *Reconstructed spatio-temporal intensity distribution of train of tree pulses separated by 1.5 ps. The reconstructed pulse train exhibits a linear spatiotemporal coupling effect that is consistent with the 0.25 mm/ps best-fit gradient observed for the pulse delay experiments (superimposed dotted line). The spatio-temporal coupling subsequently resulted in a worsened alignment for the third pulse in the train, concomitantly reducing the fringe visibility. This accounts for the apparent reduction in intensity for the final pulse.*

coupling is observed in the reconstruction of spatio-temporal intensity. The coupling speed is estimated by computing the spatial moment of the pulses as a function of

delay. This is a linear function and hence the best-fit results in slope gradient of 0.249 mm/ps which is quantitatively consistent with coupling speed observed during the delays experiments. We also program pulses trains with different central wavelengths with different second and higher order phases to test the performance of the pulse shaper. Figure 2.21 depicts an example of two pulse trains with time gap of 1 ps with different central wavelengths. The central wavelength difference results in gen-

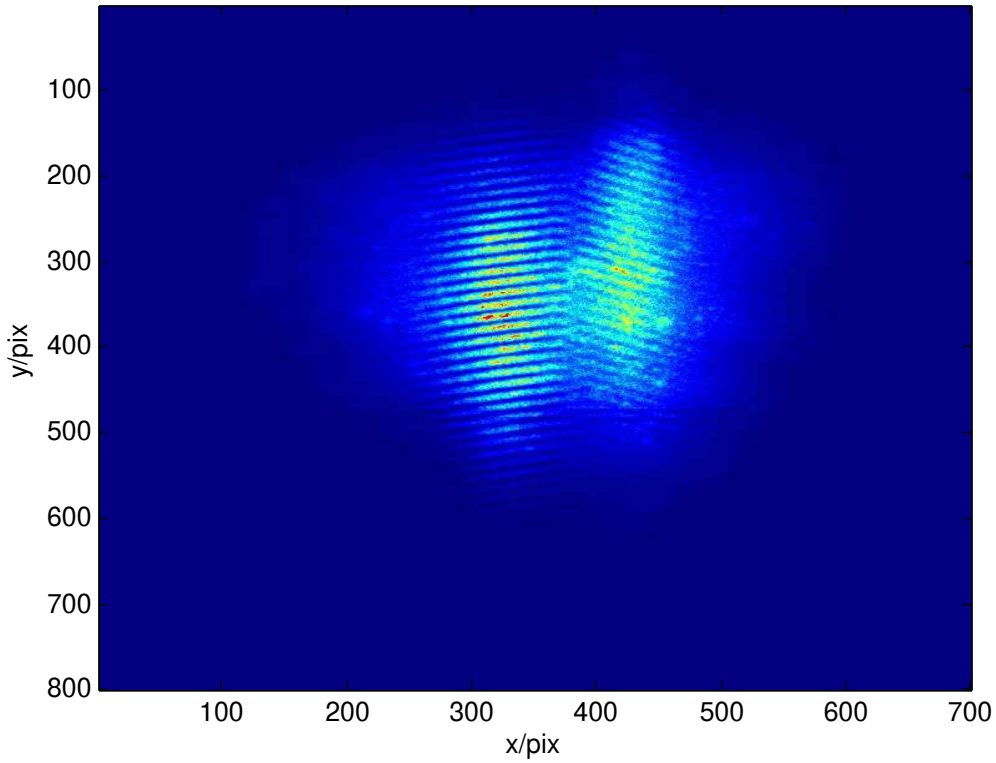

Figure 2.21: *Spatio-spectral intensity of two pulse trains with different central wavelengths. Two intensity slopes are induced because two pulse trains have different central wavelengths which is programmed to be 1.5 nm. The two pulses are separated from each other by 1 ps. The orientation of the fringe patterns are different at two lobes because the reference pulse is combined with different relative delays with each of them. The two lobes are displaced spatially with respect to each other because of being diffracted at different locations of the pulse shaper.*

eration of two lobes in recorded spatio-spectral intensity pattern. Furthermore, since the reference arm is combined with these two pulses with different relative delay, the generated fringes at the lobes have different slopes. Finally, the two lobes are spatially displaced with respect to each other. This effect, as explained above, is consistent with the time delay dependent spatial variation of the central position of the pulses in pulse delay measurements.

Chirped pulses

This experiment consists of generation of pulses with various second and higher orders to look for the existing spatio-temporal coupling effects and also verifying the consistency of the measured phases with the programmed ones [see Tab. 2.3 for the mathematical expression of the pulse chirps]. Our AOPDF pulse shaper allows programming of second order phase within the range of -100000 to +100000 fs^2 only for the case of narrowed diffracted pulse bandwidth $\Delta\lambda = 1$ nm. Figure 2.22 shows the extracted second order polynomial phase $\phi^{(2)}$ coefficients for the programmed dispersions from -100000 to +100000 fs^2 with step size of 10000 fs^2. A linear best-fit shows that the constructed phase coefficients matched the programmed values within 6%. Once again the error in the second order phase measurement is estimated from computing the standard deviation of the inferred phases over ten accumulated images. The estimated value is about 140 fs^2 [see the error bars in Fig. 2.22] that is consistant with the estimated phase error for the case where the pulse shaper is removed from the interferometer. In order to study the relevant plausible spatio-temporal coupling

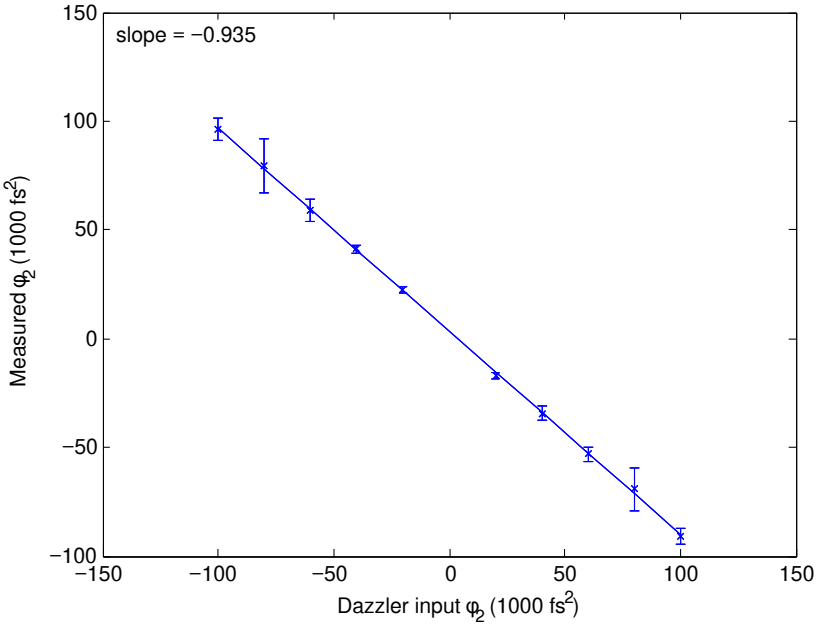

Figure 2.22: *Extracted second order polynomial phases $\phi^{(2)}$ as a function of programmed chirps from -100000 to +100000 fs^2. The x shaped points is the averaged extracted phase over ten accumulated images. The error bars shows the error in measurement of the averaged inferred phase which is estimated by standard deviation of the inferred phase over ten accumulated images. A linear best-fit shows that the constructed phase coefficients matched the programmed values within 6%.*

effects we reconstruct their spatio-spectral intensities that is shown in Fig. 2.23(a).

A spatio-spectral tilt (spatial chirp) is observed that varies as a function of chirp strength [see the dashed lines of Fig. 2.23(a)]. This observation has important consequences for control experiments with regard to spatial alignment with the sample. In

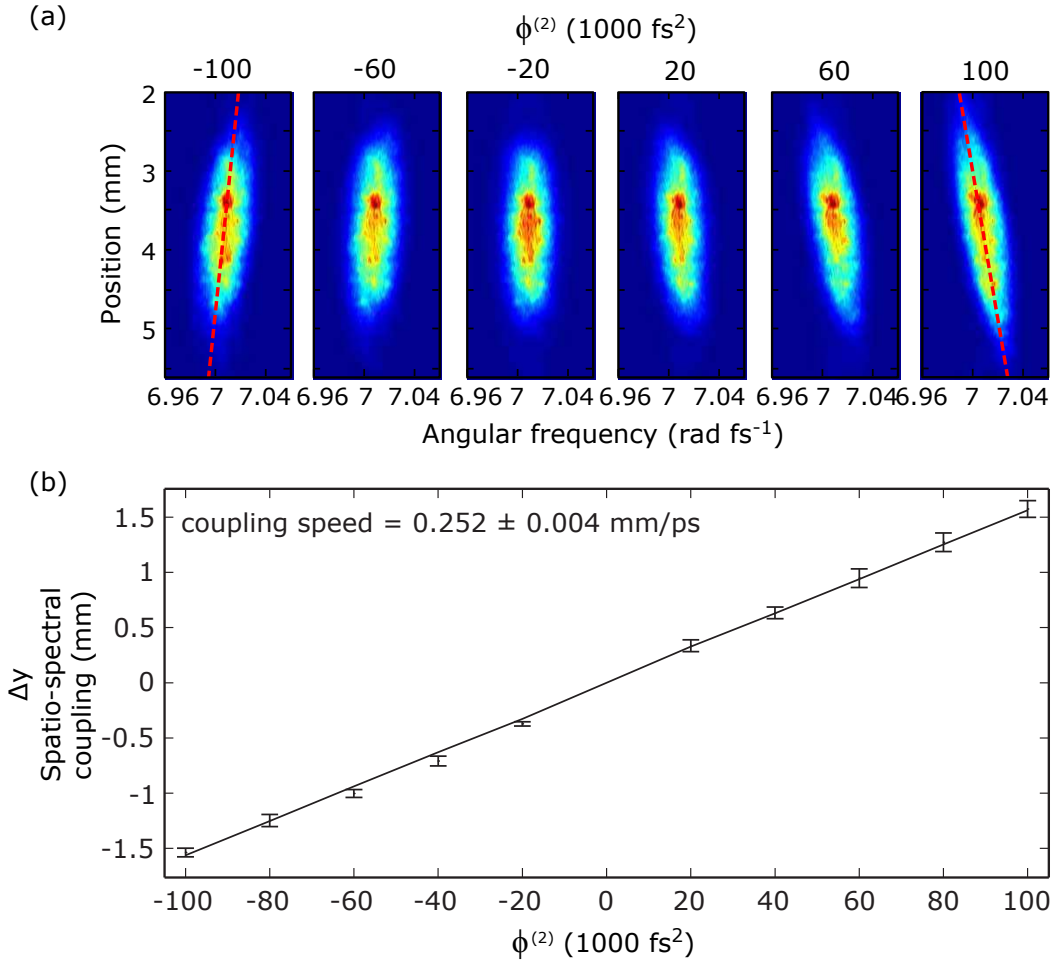

Figure 2.23: *Spatio-spectral coupling effects for a series of chirped pulses [$\phi^{(2)}$ parameters as shown]. (a) Reconstructed spatio-spectral intensities of pulses for different chirps. A spatio-spectral tilt is observed that follows linearly the chirp values. (b) Extracted spatio-spectral coupling as a function of chirp (data points) together with a calculated best-fit coupling speed of 0.252 ± 0.004mm/ps (solid line). This value is in close agreement with the measurement of coupling speed in the pulse train and pulse delay experiments. The vertical axis shows the change in central position of the beam across the spectral bandwidth of the pulse.*

order to study quantitatively the existing spatio-spectral coupling effect, we extract numerically the spatio-spectral tilts $\alpha = \Delta y/\Delta\omega$ for a range of programmed chirps. Δy is the spatial displacement of the beam center across the spectral bandwidth, $\Delta\omega = 2\pi c\Delta\lambda/\lambda^2$ is the spectral bandwidth at FWHM, c is the speed of light, λ_0=267 nm is the central wavelength and $\Delta\lambda = 1$ nm is the spectral bandwidth at FWHM.

Next, we extract Δy from the computed tilt and plot it as a function of programmed chirps in Fig. 2.23(b). Since spectral chirp is intrinsically a frequency-dependent group delay, the best-fit gradient of these points can be related to a group-delay-dependent displacement via the corresponding chirped-pulse temporal duration. This fit takes into account an intrinsic spatio-spectral tilt present on the reference beam corresponding to a 0.35 mm shift in beam center across the spectral bandwidth. The best-fit coupling speed for these experiments is 0.252 ± 0.004 mm/ps, in very close agreement with observed coupling speed in pulse delay and pulse train experiments. This demonstrates that one single underlying physical mechanism is responsible for different spatio-temporal coupling effects.

π phase step

The final experiment is the generation of π phase step at the central frequency according to $\exp[i \arctan[(\lambda - \lambda_0)/\Delta\lambda_{step}]$ (shown in Tab. 2.3). Phases with different sharpnesses, $\Delta\lambda_{step}$, are programmed. The reconstructed spectral phases, starting from lower to higher sharpnesses, across the center of the pulses (crosses) are depicted in Fig. 2.24 together with their corresponding fit function(solid line). In general, the retrieved phases match the programmed phases with regard to the parameters of above equation. The sharpest measured step sizes are in the order of 0.08 nm which is limited by the resolution of the spectrometer. The location of the π step frequency is measured to be stable in the process of programming different sharpnesses. Furthermore, neither second nor higher order phase is observed. We reconstruct the spatio-spectral intensities of the mentioned π step phase with different sharpnesses to study their plausible coupling effects. Figure 2.25 (a) depicts three of them. A local spatial displacement occurs in the spectrum at the π-step frequency, manifesting itself as a "notch" in the reconstructed spatio-spectral intensity [see arrow in Fig. 2.25(a)]. The size of the notches is dependent on the sharpness of the phase step and increases with them. In fact, this notch effect may be explained by the group velocity dependent displacement of the beam. The step phase gradient at the location of the π step can be considered as a local group delay term in the spectral phase. Therefore, a sharper step is equivalent to a steeper gradient in the spectral phase and hence a larger group delay. A group-velocity-dependent spatial displacement therefore shifts spectral components $\Delta\lambda_{step}$ by an amount dependent on the step sharpness. This argument is supported by the calculations presented in Fig. 2.25(b) based on these experimental data. In this figure, the notch sizes for each image within Fig. 2.25(a) are extracted

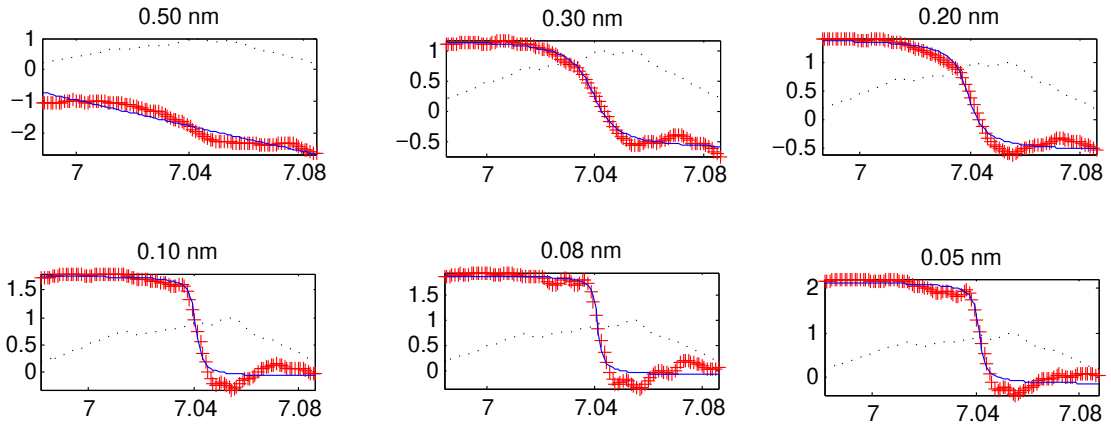

Figure 2.24: *Reconstructed spectral phase across a slice through the middle of the pulses with different π step sharpnesses(crosses) together with a fit of the function in Tab. 2.3 (solid line). The limitation in estimation of the spectral phase sharpness is 0.08 nm equal to the resolution of the spectrometer. The dotted black line reveals the reconstructed spectral amplitude of programmed ϕ phase steps.*

and plotted as a function of step sharpness (data points). The local group-delay terms at the phase step are calculated according to $\phi^{(1)} = \frac{\partial\phi(\omega)}{\partial\omega} \approx \frac{\pi}{\Delta\omega_{step}}$. They are then multiplied by the 0.25 mm/ps coupling speed previously observed (solid line), and the results shows good agreement with the experiment. Once again, the results are found to be quantitatively consistent with the same spatio-temporal coupling effect as above, reinforcing the evidence for a single underlying physical mechanism for all of these manifestations. This spatio-spectral coupling effect is identical to the same coupling effect that happens in 4f zero-dispersion line programming π phase steps [25]. In pixelated SLM shaper a complete spectral hole appears for a sharpness equal to the spectral resolution of the device. As the step sharpness is further increased in these AOPDF experiments, the π-step group delay will eventually exceed the temporal window of the crystal (which is inversely proportional to the AOPDF spectral resolution), and a spectral hole, rather than a notch, will be formed as a consequence.

Physical origin of the coupling effects

It is shown that a single spatio-temporal coupling mechanism within the AOPDF, group-delay-dependent displacement [100], accounts for all the manifestations observed in different pulse shapes. In order to explain the physical nature of this effect, it is necessary to consider a couple of effects present within the Dazzler: the birefringent and geometrical walk-off effects of the diffracted relative to the undiffracted beam, and the fact that each optical wavelength within the ultrafast pulse is diffracted

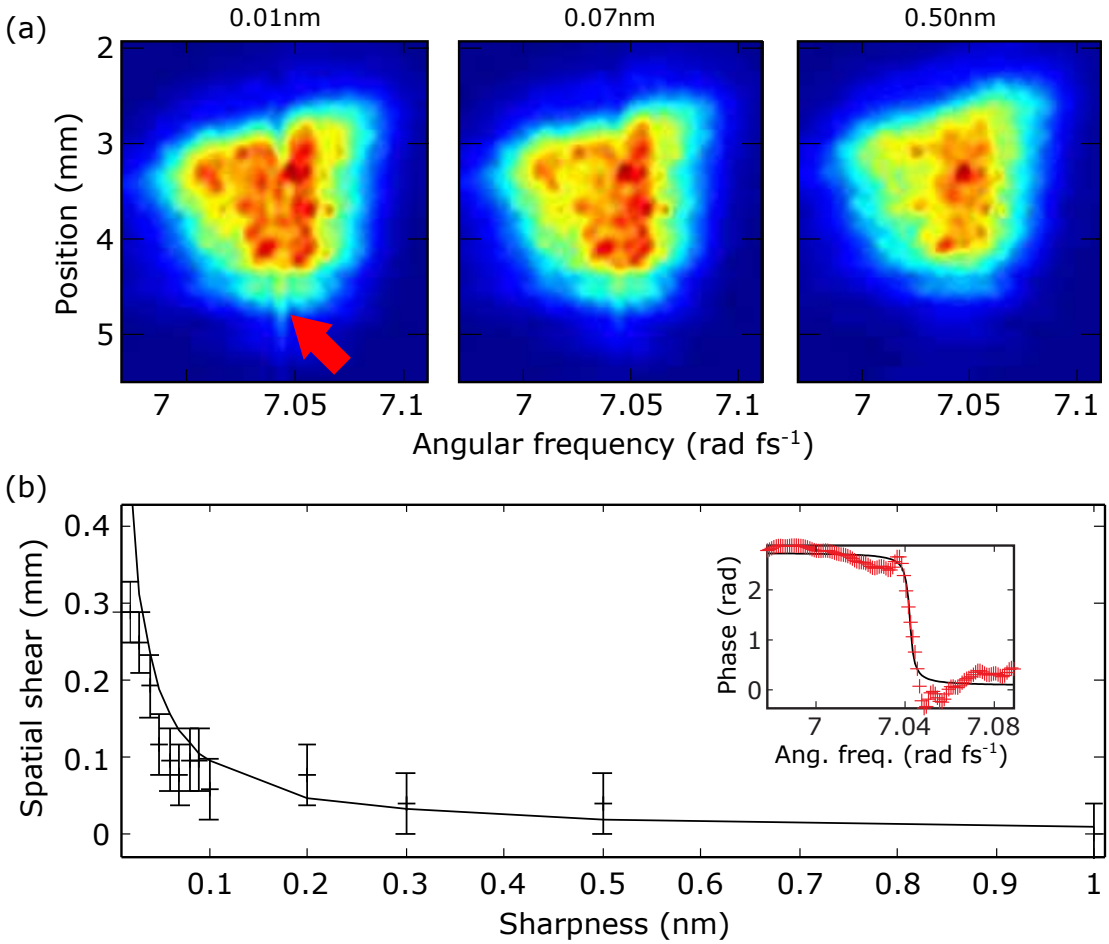

Figure 2.25: *Spatio-spectral coupling effects for π phase steps of varying sharpness.(a) Reconstructed spatio-spectral intensities of a series of π phase steps with sharpnesses as indicated. A spatial shift is observed at the step frequency that is more pronounced for sharper steps. (b) Observed lateral displacement of the notch (data points) together with a calculation derived from the measured group delay at the phase step and a 0.25 mm/ps spatio-temporal coupling speed (solid line).*

at a given position in the AOPDF. These two effects combine to lead to a natural spatial chirp, with a coupling speed as quantified above. To recapitulate, the birefringent walk-off concerns the phenomenon that the intensity distribution of a beam in an anisotropic crystal drifts away from the direction of the wave vector. The angle between the Poynting vector (which defines the direction of energy transport) and the k-vector is called the walk-off angle. Spatial walk-off occurs only for a beam with extraordinary polarization, which sees a refractive index n_e during its propagation that depends on the angle between **k** and the optical axes. This angle depends on the crystal and the parameters of the optical pulse; for the KDP crystal in this experiment,

at 268 nm, the walk-off angle is $\alpha \simeq 32$ mrad. The geometrical walk-off, meanwhile, concerns the fact that during Bragg diffraction the beam is deviated by an angle corresponding to the phase-matching condition. For this experiment, this deviation is θ = -5.2 mrad. It should be noted that both the geometric and birefringent walk-offs actually vary as a function of wavelength; however, this effect is negligible for the pulse bandwidth employed. Thus the spatio-temporal effect can simply be seen as a shift δx in the position of the diffracted beam that could be expressed as $\delta x = L \tan(\theta + \alpha)$, where L is the distance of propagation along the extraordinary axis. This experiment employs a crystal of length 75 mm such that the maximum shift is calculated as 2 mm. Considering the fact that the temporal window available at this wavelength is 7.7 ps, this implies an expected group-delay–dependent displacement of 0.260 ± 0.005 mm/ps, which is in very close agreement with our experimental measurements.

Solution

One possible solution to the existing coupling effect is to translate a lens before the AOPDF in order to bring the geometric plane of overlap of the spatially shifted output pulses into alignment with the Gaussian focal plane [100]. Another solution might be to extend the walk-off compensation methods developed in non-linear optics by using a double-pass setup or a second acousto-optic crystal [26]. It should be noted that the coupling speed depends on the parameters of the ultrafast pulses as well as the choice of crystal (indeed, the walk-off effects in TeO_2, which is used for AOPDFs in the IR wavelength range, are significantly less than in KDP); thus the calculation should be repeated along the lines above in order to make an informed choice of shaper in light of individual experimental tolerances for coupling effects.

2.4 Discussion and conclusion

In conclusion, using FTSSI technique, we have studied the spatio-spectral and spatio-temporal characteristics of the pulse shapes: a single transform-limited pulse with a variable delay, a train of pulses, chirped pulses and pulses with a π phase-step at the center of their spectrum. These pulse shapes are the most applied pulse shapes in ultrafast quantum control experiments. Our work represents the first comprehensive spatio-spectral or spatio-temporal study of the shaped pulses by an AOPDF pulse shaper. In each case, we have observed spatio-spectral (spatio-temporal) coupling in the reconstructed intensity. We have shown that the all effects are consistent with a

single effect that is group delay dependent position of the pulses [100] with coupling speed of 0.25 mm/ps. The birefringent and geometric walkoff effects are therefore confirmed as the single physical cause for the spatio-temporal coupling effect reported in the AOPDF pulse shaper. This coupling has important consequences for the application of AOPDF-shaped pulses to control experiments, since the displacement of the control pulses with a variation of pulse parameters may result in a worsened alignment with the target. The studies of Borzsonyi and his colleagues [99] showed an angular dispersion for the AOPDF in IR region. Because of employing a narrow spectral bandwidth, we have not observed such coupling. Moreover, it was because we have studied the coupling effects of a low repetition laser source. In more detail, working with high repetition source requires a high repetition acoustic wave. This causes thermal effects inside the crystal that can result in generation of angular dispersion.

As a conclusion, apart from group dependent spatial displacement of pulse no further spatio-temporal coupling effects were identified, and the AOPDF was otherwise found to reproduce the programmed pulse shapes faithfully. The results above highlight the need for experimentalists to pay close attention to these coupling issues during the design of control experiments based on an AOPDF pulse shaper. Such concerns have been studied extensively for the more widespread 4f-line shapers (in IR and visible regions), with coupling speed ranging from 0.083 mm/ps [59] through 0.145 mm/ps [24] to 0.595 mm/ps [11] already reported in the literature. The coupling speed reported here of 0.25 mm/ps is therefore non-negligible by comparison, albeit by taking into account the fact that KDF crystal has strong walk off effects in UV spectral region.

Chapter 3

Characterization and control of ultrashort pulses transmitted through scattering media

Ultrashort pulses have numerous applications in coherent control of molecular dynamics [2, 15, 148–151], time resolved spectroscopy [152], nonlinear microscopy [153], etc. Performing such experiments in the complex media such as biological tissues requires that the light maintains its initial spatio-temporal focused form. However, complex media strongly distort the initial spatio-temporal profile of the light.

Propagation of a quasi monochromatic laser light through a complex medium results in ballistic [154, 155] and multiply scattered components [156]. Ballistic photons are those that travel undeviated through the medium and deplete exponentially according to Beer's law [157]. Multiply scattered photons produce spatial speckle, which is due to the random constructive and destructive interference of light following different trajectories. Because of their random nature, the multiply scattered photons scramble the optical phase and energy of the transmitted light. Therefore, it is not straightforward to recover the optical information that is necessary for typical optical experiments, e.g. imaging, focusing, and transmitting ultrashort pulses. Numerous solutions to this problem have been proposed by discriminating against the scattered light and detection of the ballistic photons [158–164]. However, for a scattering medium with dimensions much larger than its transport mean free path l_t (the average distance traveled by light before it becomes diffuse), these techniques cannot be applied because the ballistic component is strongly attenuated.

Recently, Vellekoop and colleagues have demonstrated the possibility of spatial fo-

cusing [29, 165, 166] and hence imaging [167] through multiply scattering medium by controlling the spatial modes of the incident light using a spatial light modulator. This work, correction of the spatial distortion, has been later carried on by other groups using alternative techniques [168–172]. However, all these techniques have only addressed the use of the quasi monochromatic laser and no temporal correction has been reported.

Propagation of broadband ultrashort pulses through such thick samples results in additional large temporal spreading and irregular spiky intensity that gives rise to the spectral (temporal) speckle [173, 174]. As mentioned above, both temporal and spatial corrections are crucial for the applications. There exist related techniques for the spatio-temporal concentration in acoustic and GHz-electromagnetic regimes called time reversal methods [31, 175, 176]. However, owing in particular to the inability to measure electric fields directly in the temporal domain at higher frequencies, an optical domain time-reversal experiment remains elusive. We have solved this limitation: in a parallel work (different techniques but similar results), we [35] and two other groups [177, 178] have succeeded to spatio-temporally focus the ultrashort pulse at the rear surface of the scattering medium. For this goal, in our group in LCAR, we have applied FTSSI technique to measure the spatio-spectral phase of the output speckle and hence control them. Moreover, this measurement and characterization has resulted in other interesting results. Since studying the temporal behavior of the speckle field is one of a wide variety of methods for determination of the diffusion properties of the sample [179–189], we have demonstrated a simple technique of extraction of diffusion properties by using our well established FTSSI technique [34].

The goal of this chapter is to study the spatio-temporal characteristics of the femtosecond pulses transmitted through multiply scattering medium, extraction of the diffusion properties of such medium and finally exploiting such measurements to control the scattered light behind the medium. Therefore, it is organized as follows: Section 3.1 is a review of the present state of art in controlling of the transmitted light from scattering media. Section 3.2 is about the analytical description of the spatio-temporal focusing of the femtosecond pulses behind the multiply scattering medium via spectral shaping the input pulses. Moreover, it describes the numerical simulation that I have performed in order to show the possibility of such spatio-temporal focusing. Section 3.3 details the experimental setup that we have used to study and control spatio-temporal speckles. Section 3.4 shows the experimental results of characterization and control of the spatio-temporal speckles. Section 3.5 describes two

other ways of spatio-temporal controlling of the pulses and compares their results with ours. Finally, Section 3.6 concludes and shows the potential applications and future directions of our studies.

3.1 State of art and motivation

Studying the transmitted light through a sample (under study) can be the main means of retrieving its microscopic and macroscopic information. However, numerous media such as biological samples due to their inhomogeneous refractive index strongly scatter the incident light (continuous wave laser) and convert it to a high contrast, fine scale granular pattern which is known as speckle pattern [190]. This scattered light hinders the extraction of the necessary information (phase and intensity) of the input light which is highly important for relevant optical studies such as biomedical imaging [191] or laser therapy [192].

In the case of existence of the ballistic photons that occurs when the thickness of the sample is relatively small with respect to its transport mean free path ($L < l_t$), the obscurant issue of imaging through the biological samples may be solved by discriminating between the ballistic photons which possess the unscrambled optical information and the multiply scattered photons which are considered as a background noise (speckle pattern). Coherence tomography is a famous and widely applied example of discrimination techniques. In this technique the separation is based on time gating of the ballistic photons. In other words, it rejects the scattered light by selecting the signal based on its propagation time [27]. An other innovative technique of imaging is nonlinear microscopy where, as a result of low intensity of the scattered photons, they do not participate in the nonlinear optical processes and therefore are separated from the ballistic photons [28]. The propagation of the ballistic photons through scattered media is accompanied with some aberrations. The correction of such deformations may increase the imaging quality in the nonlinear microscopy. Rueckel and his colleagues were the first who applied adaptive optics which are frequently applied in astronomical observations [193] to correct the aberration of the emerged ballistic photons [194].

All aforementioned techniques become useless when the sample thickness gets several times larger than its transport mean free path ($L > 5l_t$). Because in this situation almost all ballistic photons are extinguished and the multiply scattered photons dominate the transmitted light. Controlling the light through multiply scattering

media was considered as a big challenge until the innovative work of Vellekoop and his colleagues who succeeded to focus the continuous-wave laser behind a thick multiply scattering medium by manipulating the degrees of freedom of the incident light wavefront [29]. Multiply scattering is a complex yet linear process and hence the transmission of light through such media can be treated by a complex transmission matrix T. The outgoing complex electric field E_m^{out} at a specific point m at the back of the sample can be expressed by

$$E_m^{out} = \sum_n^N T_{mn} E_n^{in} \tag{3.1}$$

where N is total number of input degrees of control (input spatial modes) and n is the label of input free mode. The complex electric field at the chosen m is the result of linear combination of the incident modes E_n^{in} multiplied by their corresponding elements of the transmission matrix T_{mn}. It is clear that because of the randomness of the transmission matrix the contribution of the free input modes are not in phase [see Fig. 3.1 (a)]. In order to have an enhanced E_m^{out}, since the matrix elements are fixed (transmission channels), one should manipulate the phase of the incident modes and force them to become in phase at the chosen target position. Vellekoop and his coworkers showed the experimental feasibility of such control by shaping the free input modes of the incident monochromatic laser wavefront by applying a Spatial Light Modulator (SLM). Figure 3.1 (d,e) shows the principle of their experiment. The optimal phase for each free input mode is determined by cycling its phase from 0 to 2π. Once the measurement is performed for all segments, the phase of the segments are set to their optimal values and thus the contributions from all segments interfered constructively and the target intensity is at the global maximum [see Fig. 3.1 (b)]. The degree of the brightness enhancement from such optimization algorithm is roughly equal to the degree of control of input modes:

$$\eta \approx \frac{\pi}{4} N. \tag{3.2}$$

Maximum brightness enhancement of $\eta = 1000$ was achieved in their work [see Fig. 3.1 (f,g)]. Higher degrees of enhancement become problematic because sample drifts over larger time scales that is required for higher degrees of control. In their work, the focusing took place behind the sample; however, in order to use such technique for deep tissue imaging and medical laser therapy, the focusing should occur inside the

sample. In a later work, they also showed the possibility of focusing the light inside the sample by implementing a fluorescent nanoscale probe in it [167]. Same group also illustrated the possibility of focusing the light behind the scattering medium (random photonic materials) by binary amplitude shaping of the input light [195]. In other words, they identified the input modes which give rise to fields that are out of phase with the total field at the intended output target and assign these a zero amplitude by means of the SLM, whereas the remaining segments maintain their original amplitude [see Fig. 3.1 (c)]. They obtained an intensity enhancement of around 80 at the output target position by amplitude shaping of approximately 900 input modes.
The optimization algorithm used by Vellekoop is equivalent of measuring the transmission matrix and compensating the phase mismatching introduced by the matrix elements by shaping the phase of the input transversal modes. A direct measurement of the full matrix is desirable in order to completely control light transmission and thus investigate all the statistical properties of the transmission matrix. Popoff and his colleagues for the first time measured the monochromatic transmission matrix of a complex medium in optics [169, 170]. In their work they gave four different phase values 0, $\pi/2$, π and $3\pi/2$ for an individual spatial mode n of the input light via SLM and detected the transmitted field modes by using a CCD camera. They calculated T_{mn} using the following equation

$$(I_m^0 - I_m^\pi)/4 + i(I_m^{3\pi/2} - I_m^{\pi/2})/4 = s_m T_{mn} \tag{3.3}$$

where s_m is the complex amplitude of the reference optical field in the mth output mode which is used to extract the phase value of the transmitted light. They calculated the transmission matrix by continuing the same procedure for all input modes. Using such technique, they achieved to measure the 60,000 elements which is not the sample's whole transmission matrix. The measured amount of the matrix elements depends on the number of the SLM pixels and the detection camera. The whole number of the channels of the scattering sample (matrix elements) is equal to $N_{whole} = M_s \times N_s$ where M_s is the number of existing input modes and N_s is the number of output modes. For an input monochromatic laser light centered at λ and with surface area of A, the number of free modes is given by $N_s = 2\pi A/\lambda^2$. For simplicity the same value is assumed for N_s; therefore, visible light has around 10 million transversal modes per square millimeter. Knowledge of the complete transmission matrix, or even a fraction of it, allows the light transmitted through the sample to be focused at a desired location without the need for further optimization. Moreover,

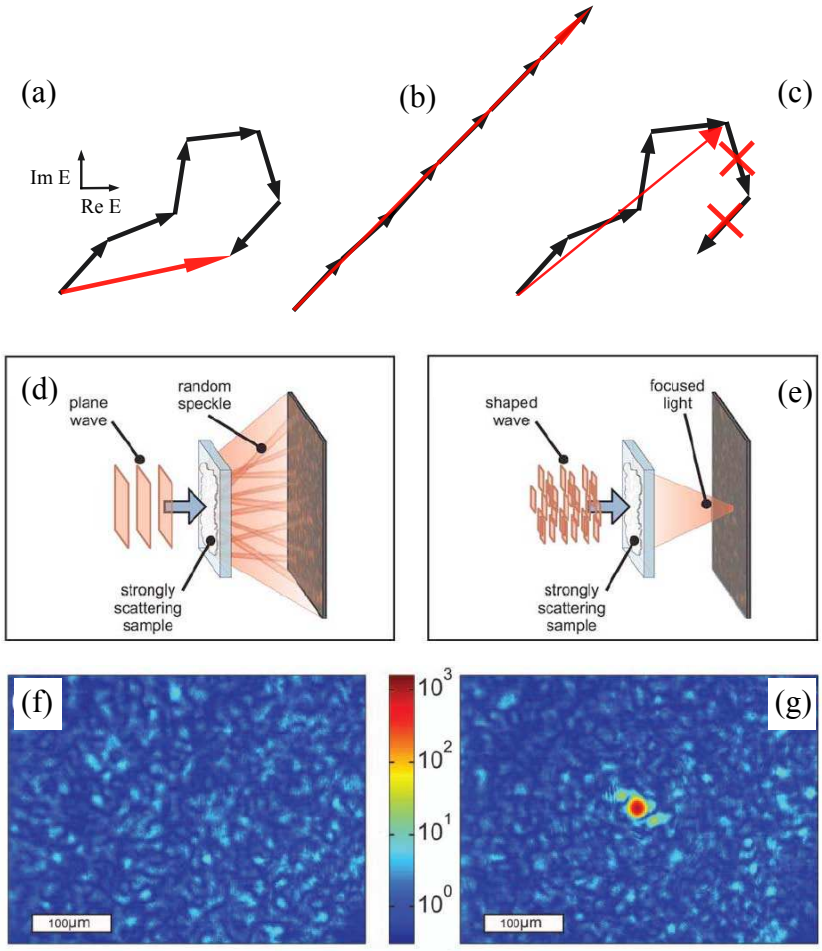

Figure 3.1: *Principle, design and result of wavefront shaping to obtain a spatial focusing behind a multiply scattering medium. Complex plane representation of the electric field at the target before optimization (a), after phase optimization (b) and after binary amplitude optimization (c). Small black vectors represent the electric field of each input channel as modified by traveling through the sample. The red vector is the total electric field at the target output channel. The phase optimization is done by changing the angle of the vectors and making them parallel while amplitude optimization is done by omitting the input channels that do not sum up constructively with the other vectors. (d) A plane wave is focused on a disordered medium, and a speckle pattern is transmitted. (e) The phase of the wavefront of the incident light is shaped so that scattering makes the light focus at a predefined target. (f) Spatial speckle pattern produced from transmission of continuous wave laser from a multiply scattering medium. (g) Transmission after spatial phase optimization to focus at a single target. The scattered light is focused to a spot that is 1000 times brighter than the original speckle pattern. This figure is adopted from [29].*

it also allows the statistical properties of the transmission matrix to be examined directly. Furthermore, Popoff and co-workers demonstrated the ability to image using a scattering medium with a known transmission matrix as a lens [168]. They projected

an image on their sample and made a phase-sensitive measurement of the transmitted light, which appeared totally uncorrelated to the original image. However, using the information in the transmission matrix, they were able to reconstruct the image.
The multiply scattering is a deterministic and time-reversible process. This means that if one measures the phase and amplitude of the scattered light and reproduces a back scattering phase-conjugated field, this field should be able to retrace its trajectory through the scattering medium and return the original input light field. It should be mentioned that the absorption of the light by the tissue breaks the time direction symmetry associated with that light component and hence reduce the efficiency of the optical phase conjugation process. Optical phase conjugation can be achieved by different techniques such as holography [196, 197], four-wave-mixing [198, 199] etc. In early sixties, scientists used this phase conjugation technique to correct the phase scattering due to the single scattering process induced by a ground glass slide [200]. However its application to suppress the turbidity of the biomedical samples was remained largely unexplored until the pioneering work of Yaqoob and his colleagues [172] who implemented it for the first time to correct the wavefronts in biological samples. They succeeded to transmit the phase conjugated beam which was obtained from photo refractive crystal during the holography process through a slice of chicken tissue and therefore focus the light on the same side of the medium from which the incident light comes. Phase conjugation technique introduced by Yaqoob does not require any learning algorithm and hence would be performed over shorter time scales, as is highly demanded for microscopy of live tissues. However, illuminating the photo refractive crystal took two minutes which is comparable with the aforementioned techniques. Later Cui and his colleagues introduced the digital phase conjugation technique that could work in shorter time scales [201]. To generate phase conjugate wave digitally, one simply needs a device which can be used both as a sensor and as an actuator. The piezo transducer employed in acoustic time reversal experiments is a good example [31]. However, such device does not currently exist for optical processing. Therefore, they implemented an equivalent system by combining a wavefront measurement device (sensor) with a spatial light modulator in an optical arrangement. In more detail, a reference wave with a flat wavefront interferes with the unknown scattered wave and form a hologram on the CCD camera. By using phase shifting holography [202], the phase and amplitude information of the scattered wave is determined. Then, the measured wavefront is digitally reversed by a computer and passed to the SLM. The reflection of the reference beam incident on the SLM is modulated

and counter-propagates with respect to the input wave, which is the phase conjugate of the input signal. Applying SLMs makes it possible to create phase-conjugate waves with great flexibility [i]. Therefore, it became a key technique in relevant imaging techniques [203–207].

All aforementioned studies were focused on quasi-monochromatic light which only allows spatial control over the scattered light. Because of their high peak power, femtosecond pulses are highly valuable in the community. The propagation of ultrashort optical pulses with a broad spectral bandwidth in a scattering medium results in temporal stretching of the pulse. The temporal stretching can be characterized by Thouless time τ_d which reveals the average temporal behavior of the transmitted pulse. From spectral point of view, the stretched pulse is characterized by two properties: the incident spectral bandwidth $\Delta\omega$ and spectral correlation length $\delta\omega$. The spectral components that stay within $\delta\omega$ will follow the same trajectories (channels) in the scattering media and hence form same spatial speckle while the spectral modes of the scattered field at two frequencies apart by more than $\delta\omega$ form independent decorrelated spatial patterns. It is shown that the intensity enhancement by optimization algorithm just takes place over the scale of $\delta\omega$ and when the frequency of the laser tuned by more than spectral correlation length the effect of optimization is lost [208]. The spectral correlation length which is considered as a smallest spectral feature of the spectral speckle is inversely proportional to the Thouless time of the sample $\delta\omega \propto 1/\tau_d$. This is because the spectral characteristics of the speckle patterns are related to the temporal patterns by Fourier transform. Therefore, in addition to spatial speckle one will also observe a temporal speckle [173, 174].

In the broadband regime one can measure the distorted amplitude and the phase at a target point behind the sample and control the input wave in a way that all the uncorrelated speckles add in phase at a specific time at the chosen target point. This may be done by phase conjugation of the phase of each spectral component of the measured polychromatic wave field and send it again through the medium. In this case all the speckles are phase matched and interfere constructively at the desired location and a spatio-temporally focused wave emerges from the complex medium. This happens owing to reciprocity. It was in the acoustic regime where for the first time Derode and his colleagues showed the possibility of such compensation called time reversal [30, 31]. In their study they sent a wave with initial duration of 1 μs

i. However precise pixel to pixel calibration between the CCD camera and the SLM should be performed which is not an easy task.

with a central frequency of 1.5 MHz using a transducer to the scattering medium which was a forest of steel rods immersed in a water tank. They employed a set of receivers on the other side of the medium to measure the field of the distorted wave. The measured signal that lasted 100 times of the duration of the initial wave was time reversed using the computer and sent back to the medium using the same receivers that act as emitters. The detected signal by the initial transducer was tightly focused in space an time. Figure 3.2 shows the principle of such time reversal experiment. In

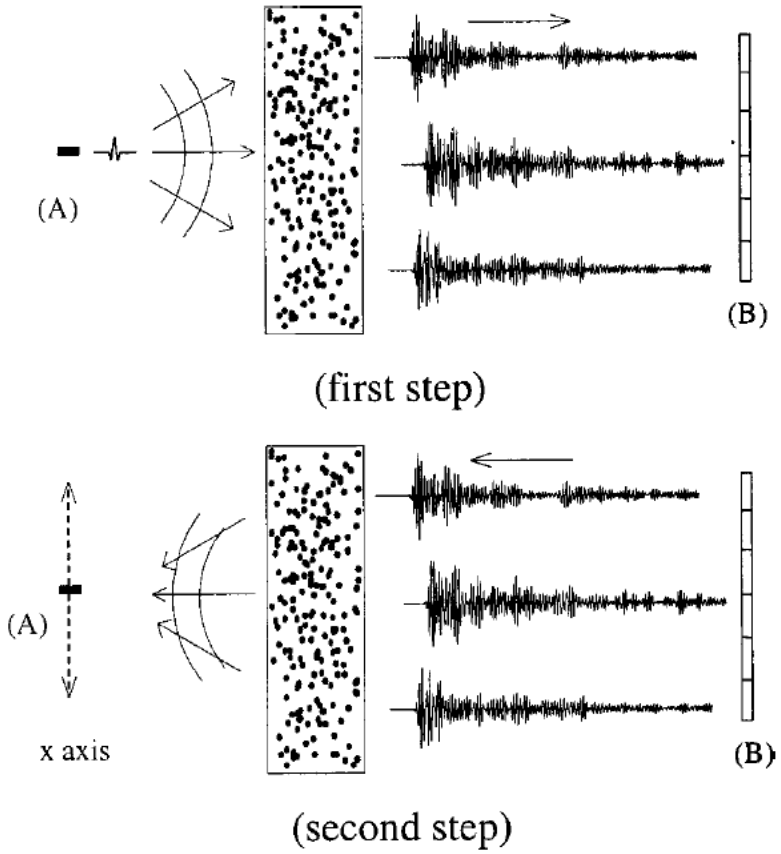

Figure 3.2: *Principle of time reversal in acoustic regime. In the first step a piezo transducer generates acoustic waves. The scattering medium distorts the emitted wave. An array of receivers at the back side of the medium record the distorted wave. In the second step the recorded wave is digitized and time reversed by a computer and sent back via the same array of receivers who act as a emitter to the scattering medium. The detected signal by the source is tightly focused in time and space. This figure is adopted from [209].*

such experiments the degree of intensity enhancement is

$$\eta = \Delta\omega/\delta\omega \times \Delta x/\delta x \tag{3.4}$$

where Δx is the array aperture and δx is the spatial correlation length. This shows that the extra dimension of control (frequency) drastically increases the possibilities of the signal enhancement at the chosen point. The other probable conclusion is that η increases as a function of square of sample thickness because $\delta\omega \propto 1/\tau_d$ and $\tau_d \propto L^2$. However, when the sample thickness becomes too large, temporal side lobes appear in the time reversed signal which may decrease the signal to noise ratio [209]. The reason is that as the sample gets thicker the probability that different photons follow the same path at part of their trajectory in the sample increases. This increases the temporal coherence length $\delta t \propto 1/\Delta\omega$ which can be interpreted as a reduction of the spectral bandwidth. Therefore, there is trade off between the spectral resolution and spectral bandwidth and always there is an ideal thickness at which one can obtain the best signal to noise ratio. The other advantage of using the broadband width pulses is that one can obtain the spatio-temporal focusing only by employing a single signal receiver on the back of the medium which of course reduces the signal to noise ratio by only manipulating the first coefficient of the Eq. 3.4 [210].

The spatial resolution of the obtained spatio-temporal focusing occurs on the range of spatial correlation length of the medium δx which evolves as a function of l_t/L. Therefore for a given sample the focusing gets tighter as the samples thickness increases. Researchers also demonstrated time reversal in the electromagnetic domain using modulators that conjugate only the signal bandwidth rather than the full carrier bandwidth [32, 33]. Time reversal remains elusive for higher frequencies and optical domain because it is not straight forward to measure and apply the time reversal of the pulse electric field in such domains. Understanding and correcting the spatio-temporal distortions of ultrashort pulses is crucial to perform a nonlinear microscopy and coherent control experiments in the scattering biological samples. No work to date has addressed the simultaneous correction of temporal and spatial distortions of the femtosecond pulses except our [61] and two other parallel works [177, 178]. In the following, I will first detail our work and then at the end of this chapter, I will briefly describe their studies and compare their results with ours.

3.2 Analytical description and numerical simulation of spatio-temporal control

3.2.1 Analytical description

Owing to the linearity of the scattering process, knowledge of the spectral phase facilitates active temporal focusing of the speckle via the open-loop feedback of the measured phase to a spectral pulse shaper placed before the sample. Our experiment relies on a spatially resolved phase measurement, as the lack of large-scale spatial homogeneity in the speckle field prevents the spatial integration typical of control experiments.

Multiple scattering is a complex yet linear process, therefore the evolution of the pulse electric field through the medium may be elucidated by a Green function formalism. For a given spectral component, and for a distribution of sources $E_S(r', \omega)$, the resulting field reads $E(\omega, r) = \iiint G_{\text{scatt}}(\omega, r, r')E_S(\omega, r')d^3r'$, where $G_{\text{scatt}}(\omega, r, r')$ is the Fourier component of the Green function between point r and r', in the presence of scattering. In our simple case where we enter with a focused beam commensurate with the correlation distance of the scatterers $E_{\text{in}}(\omega)$, the Green function reduces to $E_{\text{out}}(\omega, y) = H_{\text{scatt}}(\omega, y)H_{\text{shaper}}(\omega)E_{\text{in}}(\omega)$, where $H_{\text{scatt}}(\omega, y) = A_{\text{scatt}}(\omega, y)\exp[i\phi_{\text{scatt}}(\omega, y)]$ and $H_{\text{shaper}}(\omega) = A_{\text{shaper}}(\omega)\exp[i\phi_{\text{shaper}}(\omega)]$ are the medium and shaper transfer functions respectively, with both consisting of phase and amplitude contributions. The FTSSI measurement reveals the relative phase $\phi_{\text{scatt}}(\omega, y) - \phi_{\text{in}}(\omega)$ with the pulse shaper set to $H_{\text{shaper}}(\omega) = 1$. The coupling between spatial and spectral modes in the scatterer, and the concomitant inseparability of $H_{\text{scatt}}(\omega, y)$ into a product of spatial and spectral components, is the root of the exigence of a spatially resolved measurement for a spectral phase correction. In general, a complete reversal of the scattering process would therefore require a spatio-spectrally resolved shaping element covering all the contributing modes, rather than successive shapers controlling the spatial and spectral degrees of freedom independently. In our experiment, such an open-loop compensation of the spectral phase is performed. A position y_0 is selected and the transfer function $\phi_{\text{shaper}}(\omega) = -\phi_{\text{scatt}}(\omega, y_0)$ is applied to the pulse shaper. A successful phase compensation at y_0 is demonstrated by a further FTSSI measurement of $\phi_{\text{out}}(\omega, y_0) - \phi_{\text{in}}(\omega, y_0) = 0$. Furthermore, this flat output phase (and consequent temporal focus) is spatially localized as determined by the spatial phase correlation length. Therefore, a spatially resolved spectral shaper is not a

prerequisite for a degree of spatial control.

3.2.2 Numerical simulation

Before presenting the experimental results of the spatio-temporal focusing, I show the numerical simulation of such control which is based on aforementioned analytical description of the experiment. The difference is that, for simplicity, wavelength dependent transmission matrix $t(\omega)$ is applied instead of transfer function $H(\omega, y)$. Furthermore, one of the spatial dimensions x is neglected for the ease of simulation. The output electric field $E(\omega, y_m)$ at specific point y_m is given by

$$E(\omega, y_m) = \sum_{n}^{N} t_{mn}(\omega) E(\omega, y_n). \tag{3.5}$$

In the numerical simulation I follow the following steps:
1. Ultrashort pulse with spectral bandwidth relevant to the experiment is constructed. It possesses a Gaussian wavefront [see Fig. 3.3 (a)]. Its spatio-temporal intensity distribution is shown in Fig. 3.3 (b).
2. Random transmission matrix for each spectral component is constructed which reveals a 3D array with total elements of $N_{in} \times N_{out} \times N_{\omega}$ where Ns are the total number of input modes, output modes and spectral elements respectively. In this simulation, the spectral correlation length $\delta\omega$ is set to the minimum which means a single spectral pixel. This means that our simulation is not sensitive to the thickness of the sample.
3. The transmitted spatio-spectral complex electric field $E(\omega, y)$ is obtained from Eq. 3.5. Figure 3.3 (c) shows $|E(\omega, y)|^2$ which reveals the well known spatio-spectral speckle pattern. Spatio-temporal speckle shown in Fig. 3.3 (d) is reconstructed from Fourier transforming $E(\omega, y)$ along the spectral dimension. Since $\delta\omega \propto 1/\tau_d$ is equal to size of a pixel in spectral domain it reveals a temporally stretched pulse on the scale of temporal windows in the temporal domain.
4. In order to force all spectral components to be in phase at a specific time at a chosen point y_{m^*} (temporal compression), the spectral phase $\phi(\omega, y_{m^*})$ is measured [see Fig. 3.4 (a)] and its opposite $-\phi(\omega, y_{m^*})$ is multiplied with the initial electric field $E(\omega, y_n)exp[-\phi(\omega, y_{m^*})]$.
5. Shaped input pulse $E^{inshaped}(\omega, y_n) = E(\omega, y_n)exp[-\phi(\omega, y_{m^*})]$ is sent to the sam-

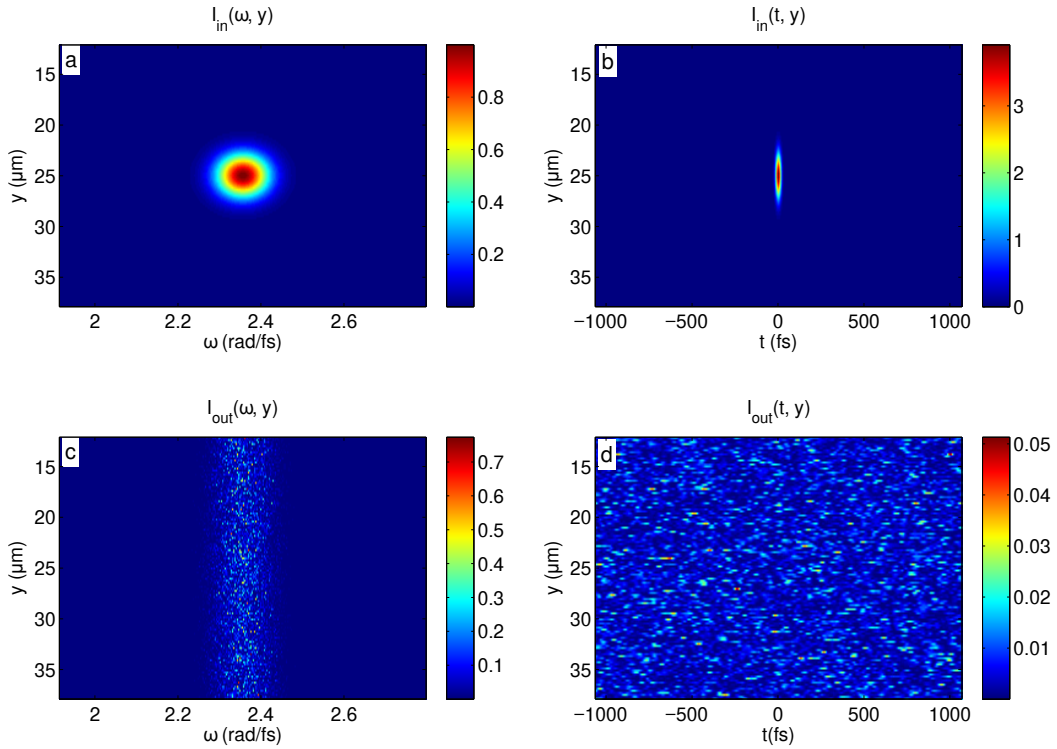

Figure 3.3: *Simulation of propagation of spatio-spectrally Gaussian pulse through a multiply scattering medium. Spatio-spectral $|E(\omega, y)|^2$ (a) and spatio-temporal $|E(t, y)|^2$ (b) intensity distribution of input pulse. Spatio-spectral (c) and spatio-temporal (d) speckle pattern. Spectral correlation length $\delta\omega$ is the size of spectral pixel (no spectral correlation is added to the simulation). Therefore, in temporal domain pulse is stretched to whole temporal window $\delta\omega \propto 1/\tau_d$.*

ple. The measured complex output electric field at the chosen output mode y_{m^*} reads

$$E^{outshaped}(\omega, y_{m^*}) = \sum_{n}^{N} t_{m^*n}(\omega) E^{inshaped}(\omega, y_n). \tag{3.6}$$

Figure 3.4 (b) depicts the measured spatio-spectral shaped output phase. The spectral phase is zero at the chosen point of y_{m^*} which means the pulse is temporally compressed. Figure 3.4 (c) is the 3D form of Fig. 3.3 (d) and its projections on the wall shows the existence of the spatial and spectral speckle. Figure 3.4 (d) shows the spatio-temporal shaped speckle. An intense peak emerges from the background with a contrast ratio of $\Delta\omega/\delta\omega$. This is the proof that spatio-temporal focusing can be experimentally performed by spectrally shaping the input pulse.

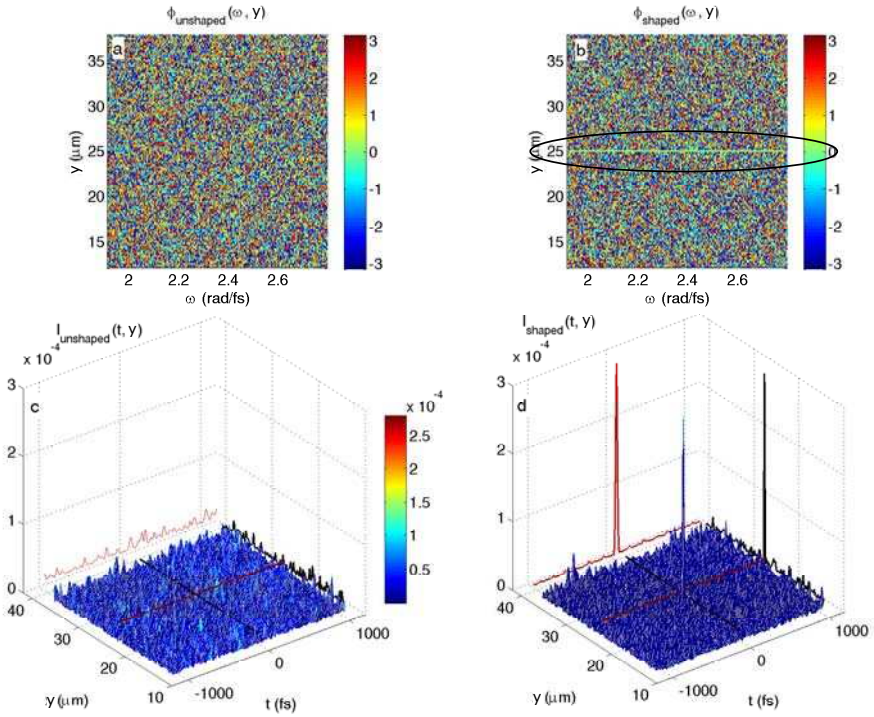

Figure 3.4: *Simulation of spatio-temporal focusing of the ultrashort pulses behind a multiply scattering medium via spectral pulse shaping. (a) Spatio-spectral unshaped speckle phase $\phi^{unshaped}(\omega, y)$. (b) Spatio-spectral shaped speckle phase $\phi^{shaped}(\omega, y)$. Zero spectral phase at a chosen position y_{m^*} is evident showing that spectral phase shaping is able to correct the temporal distortions of the pulse at a chosen point. Spatio-temporal intensities $|E^{out}(t, y)|^2$ (c) before and (d) after compensation of the phase at y_{m^*}. An intense peak emerges from the background with a contrast ratio of $\Delta\omega/\delta\omega$. One-dimensional 'lineouts' at the location of this peak (projections onto walls) in (c) shows the existence of spatial and temporal speckle while spatio-temporal focusing is observed in (d).*

3.3 Experimental setup

3.3.1 Sample preparation

The investigated scattering samples are a thick layer of ZnO powder, which is deposited homogeneously on a microscope slide by sedimentation [211]. The transport mean free path of the samples $l_t = 2.1 \pm 0.2$ μm was measured by Sylvain Gigan, our collaborator in Institut Langevin. It is determined by measuring the angularly integrated total transmission T_L as a function of sample thickness L and fitting it to a simple model [187], which relates T to L and l_t. All of the applied samples have thickness of $L \geq 9l_t$ and hence multiply scattering regime applies and virtually no ballistic light traverses the medium.

3.3.2 Fourier-Transform Spatio-Spectral Interferometry

As mentioned above we have applied FTSSI for the characterization and control of the speckle pattern. The experimental setup for the characterization is depicted in Fig. 3.5. The ultrashort source is a homemade mode-locked Ti:sapphire oscillator that delivers 5 nJ pulses at 793 nm at 80 MHz. The spectrum of the laser source with a Gaussian fit is depicted in Fig. 3.6. Its spectral bandwidth is 8.3 nm at full width at half maximum (FWHM). A SPIDER measurement of the source indicates a 120 fs pulse duration, which is close to Fourier-transform limit. To make an interferometer the oscillator beam is divided into sample and reference arms by a beam splitter with a ratio of 96:4, respectively. The former is focused on to the sample to a waist of 15 μm by means of a lens (L1) with a focal length of 75 mm. The sample transforms the ultrashort pulse into a complex spatio-temporal speckle. A second lens (L2) with a numerical aperture of 0.25 collects the scattered, transmitted light and images it with 14$\times$ magnification on to the entrance slit of a homemade spectrometer. The generated speckle at the rear side of the sample is diffused homogeneously in to 2π sr. Therefore, it is better to apply an imaging lens with larger numerical aperture to collect the maximum of diffused light (enhanced signal on the spectrometer). However, microscope objective lenses who benefit from a larger numerical aperture add an additional dispersion to the generated speckle field due to their applied thick optics. In our setup in order to prevent the unwanted dispersion, a thin high diameter lens with a short focal length is applied. The home-made imaging spectrometer which was designed by Austin *et al.*, our collaborators in Oxford university [146], consists of a CCD camera (SMX150) sensitive to visible and IR wavelengths, a grating with 1200 grooves/mm, and an entrance slit of 10 μm. Its spatial and spectral resolutions are 20 μm and 0.04 nm, respectively. Both spatial and spectral resolutions are measured by replacing the entrance spectrometer slit by a 10 μm pinhole and illuminating the spectrometer by a calibration lamp. Moreover, it is an aberration free spectrometer except for distortion which is removed during the space-frequency mapping process. For more explicit detail of the device I invite the readers to refer to section 2.3 of chapter 2. The magnification of L2 is chosen such that the grain size of the speckle pattern is larger than the spatial resolution of the spectrometer. We have taken care in placing the rear surface of the sample in the imaging plane, which we have located using a test image, since this affects the inferred spatial autocorrelation length. Specifically, the propagation of the speckle field after exiting the scattering sample causes an enlargement of the speckle grain size. The produced spatio-temporal speck-

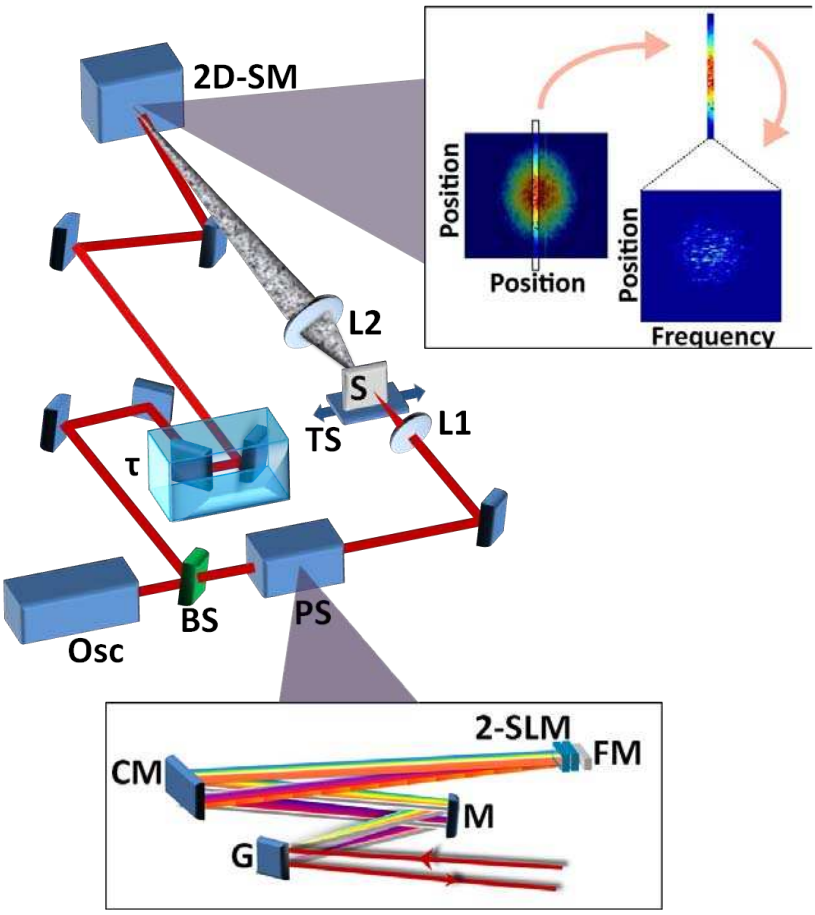

Figure 3.5: *Experimental setup. The laser oscillator beam (Osc) is divided into sample and reference arms by a beam splitter (BS). The sample arm is focused on to the sample (S) by lens L1. The sample is mounted on a translation stage (TS) moving perpendicular to the laser beam. Lens L2 images the transmitted-diffracted light on to the spectrometer slit (2D-SM). The reference arm is combined with the sample arm with an adjustable delay and angle at the entrance slit of the spectrometer. Upper inset figure demonstrates how the spectrometer performs a spatially resolved measurement of the spectral intensity along the entrance slit. In the control part, a pulse shaper (PS) is placed in the sample arm before the scattering sample. The spectral pulse shaper is a folded 4f line, and comprises a grating (G), cylindrical mirror (CM), plane mirror (M), folding mirror (FM) and spatial light modulator (SLM).*

les are stationary over the exposure time of the CCD camera, which is approximately 100 ms. The temporal stability of the samples can be calculated by recording the speckle of a monochromatic laser source as a function of time on a simple webcam and then measuring the bandwidth of the correlation function of a single speckle grain along the time axis. The reference arm is recombined with the sample arm with an adjustable relative angle and delay at the entrance of the spectrometer slit. The SSI

technique measures the relative spatio-spectral phase between an unknown pulse and the reference. In fact it directly measures the transfer function of sample plus the residual phase of the optics in the sample arm. Subtraction of the measured relative phases obtained from the case where the sample is removed from the interferometer arm and the case where the sample is in the arm allows the recovery of the sample phase (transfer function). The power ratio between the reference and the input sig-

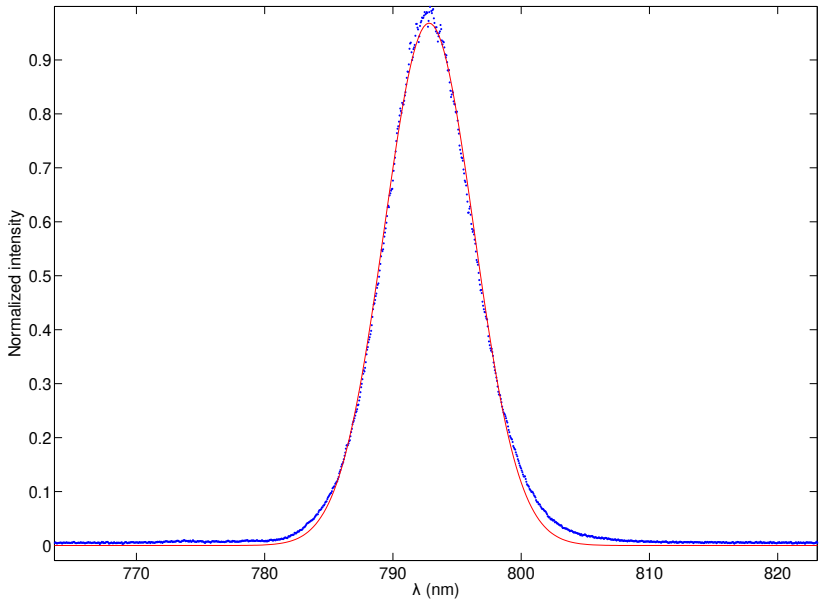

Figure 3.6: *Spectral intensity of the laser source. Dotted blue line is the measured spectral intensity by a calibrated spectrometer. Solid red line is the Gaussian fit with central wavelength of 792.8 nm and bandwidth of 8.3 nm at FWHM (corresponding to 110 fs Fourier-limited pulses).*

nal arm is adjusted in a way that offers approximately the same intensity for both arms on the spectrometer to obtain the maximum fringe visibility. The reference arm intensity on the entrance of the spectrometer is measured to be 5.5 W/cm^2. The uncertainty on the reference intensity has been estimated by computing the standard deviation of the inferred intensity over several accumulated images. These images are taken directly by blocking the sample arm and measuring the reference intensity on the spectrometer. Figure 3.7(a) depicts the recorded spatio-spectral distribution of the reference signal averaged over 5 accumulated images. Figure 3.7(b) shows the standard deviation of reference intensity obtained from 5 accumulated images. The camera noise is extracted from off-signal regions (red rectangle) of Fig. 3.7 while the laser fluctuation is measured from signal region (black rectangle). The signal-to-noise ratio at the peak of the signal is measured to be approximately 100. The

spatial intensity distribution of the reference arm is measured by integration along the spectral axis of the spatio-spectral intensity of Fig. 3.7 (a). It is approximately a Gaussian distribution. The spectral and spatial interference fringe carrier frequencies

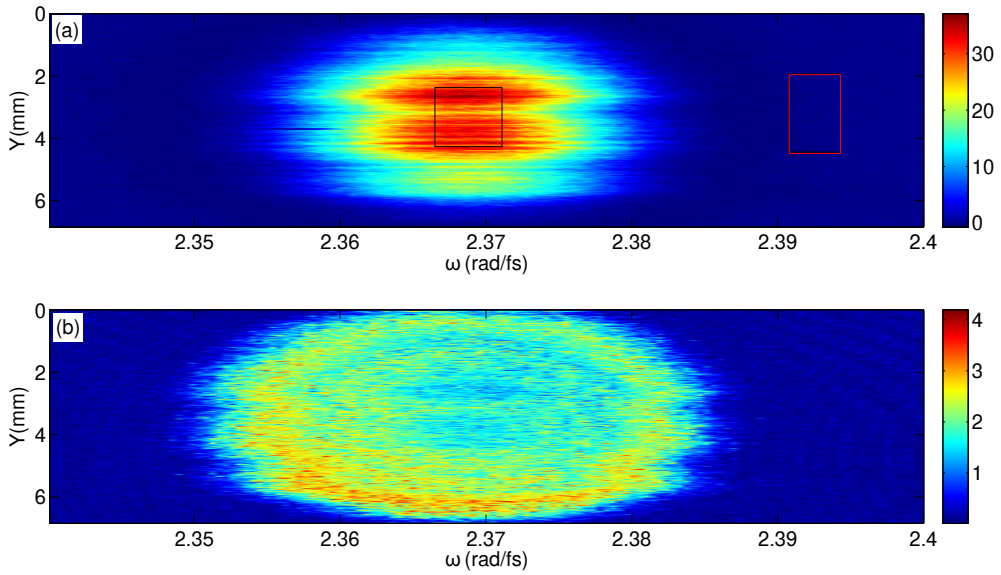

Figure 3.7: *Spatio-spectral intensity of the reference arm and its fluctuations. (a) Spatio-spectral intensity distribution of the reference arm, which is averaged over 5 accumulated images, is measured by the home-built spectrometer. Black rectangle shows the regions with 10% of the peak of the signal. Red rectangle shows the off-signal region. (b) Standard deviation of the inferred reference arm over 5 accumulated images. The uncertainty of the reference intensity is estimated by computing the standard deviation of the inferred intensity over 5 accumulated images. The camera noise is extracted from the off-signal regions of the figure while the laser fluctuation is measured from signal region. The signal-to-noise ratio at the peak of the signal is measured to be approximately 100.*

are determined by the relative delay τ and angle θ between two pulses, respectively. The relative spectral phase will additionally modulate the fringes. Hence this fringe pattern intensity can be expressed by the following equation:

$$I(\omega, y) = |E_r(\omega, y)|^2 + |E_s(\omega, y)|^2 + 2|E_r(\omega, y)||E_s(\omega, y)| \cos[\phi_r(\omega, y) - \phi_s(\omega, y) - \omega\tau - k_y y]. \tag{3.7}$$

Here y is the spatial coordinate and $k_y = |k| \sin\theta$ is the difference between the transverse components of the wavenumbers. E_r , E_s, ϕ_r , and ϕ_s are the spatio-spectral amplitude and phase of the reference and sample, respectively. The first and second terms are the reference and sample intensities, respectively, and the third term shows a coupling of the sample and reference amplitudes with their relative spatio-spectral phase. Figure 3.8 shows a typical interference pattern recorded by the spectrometer.

In order to reconstruct the spatio-temporal characteristics of the unknown pulse, the spatio-spectral phase of the sample is extracted via Fourier filtering [86], while the amplitude is directly obtained by measuring the sample intensity on the spectrometer when the reference arm is blocked. The magnitude of the fluctuations in the intensity of the sample arm is approximately 1%. The spatio-spectral interference pattern is first Fourier transformed along both spectral and spatial dimensions [Fig. 3.8 (b)]. Then one of the ac terms, corresponding to the cross-term in the above equation, is filtered out and inverse transformed [Fig. 3.8 (c)]. Thus, the complex spatio-spectral electric field of the transmitted light is reconstructed from the calculated spatio-spectral amplitude and phase [Fig. 3.8 (d)]. The full spatio-temporal electric field and intensity may thus be reconstructed by a further Fourier transform. Figure 3.8(b) also illustrates the way in which the use of a spatially resolved detector relaxes the required spectral resolution. Because we chose a predominantly spatial carrier, the interferometric sidebands were displaced predominantly along the wavenumber (vertical) axis. If we had used purely spectral interferometry, the sidebands would be displaced along the temporal (horizontal) axis. For the data shown in Fig. 3.8 (b), the temporal range would have been insufficient, forcing either an overlap with the baseband term or clipping of the energy at high time values.

The experimental setup used for the control part is same as the setup used for the characterization part except that a pulse shaper is implemented on the sample arm. The laser source is also replaced by an oscillator that provides broader spectral bandwidth and hence shorter pulses. It is because according to Eq. 3.4 spectrally broader pulses $\Delta\omega$ provide higher degrees of signal enhancement. The ultrafast source used for this experiment is an 80 MHz oscillator that delivers 4 nJ pulses at 800 nm with a spectral bandwidth of 80 nm and duration of 20 fs. The applied pulse shaper is able to shape phase and amplitude of the femtosecond pulses. It comprises a pair of liquid-crystal spatial light modulators (SLMs) in the Fourier plane of a folded double-pass 4f zero-dispersion line [59]. In the following, I give some brief information about the characteristics of our pulse shaper. However for more explicit information, I invite the readers to refer to first chapter of this manuscript or the PhD manuscript of Monmayrant [65]. The optical elements of the pulse shaper are separated by approximately 600 mm (cylindrical mirror with focal length of 600 mm). The gold-coated grating has 2000 lines/mm. The applied SLMs are 64 mm long consisting of 640 pixels. The pulse shaper with mentioned characteristics provides resolution of 0.06 nm/pixel at 800 nm. In order to optimize the trade-off between bandwidth and shaping resolution,

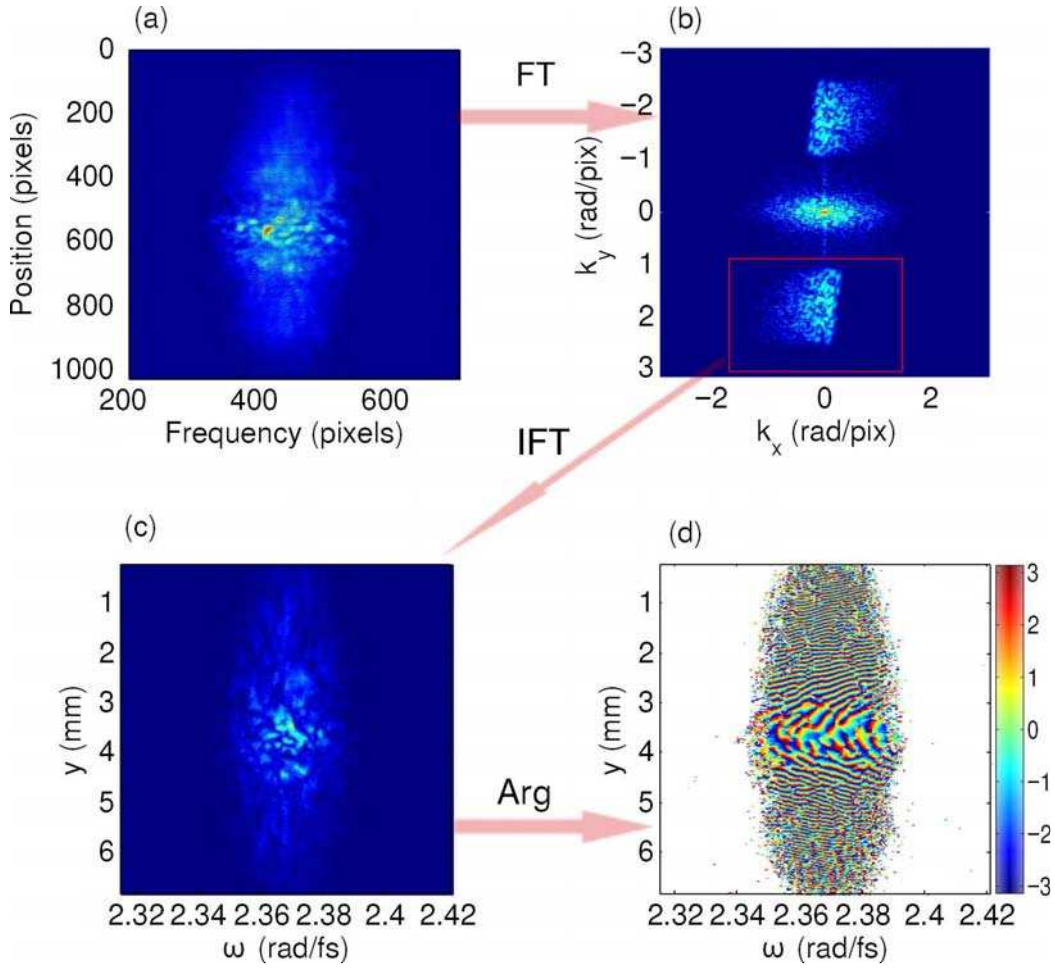

Figure 3.8: *Fourier filtering process. (a) Interference pattern of the reference and sample arm is detected by an imaging spectrometer. (b) A two-dimensional Fourier transform is performed. An ac term is filtered out within the Fourier domain. (c) An inverse two-dimensional Fourier transform of this term isolates the interferometric term. (d) The extracted spectral phase difference recovers the transfer function of the sample plus residual phase of the optics in the sample arm. The color is set to white where the signal amplitude is low and the extracted phase becomes meaningless.*

the 4f-line grating is chosen so as to overfill the SLMs; thus the output bears a clipped 30 nm hyper Gaussian spectrum and may be shaped within a 23 ps time window fixed by the set-up. The calibrations of the pulse shaper are done by using a commercial spectrometer which itself is calibrated by a calibration lamp. The calibration of the home-built spectrometer is also performed by the calibration lamp and hence there is no systematic error in our measurements. For typical measurements of the control part, the recorded signal by CCD camera of the spectrometer is average of 80×10^5 shots (acquisition time of 1 s). Same scattering sample (ZnO) is used with thickness

of $L = 35 \pm 5$ μm and with negligible absorption.

3.4 Experimental Measurements and results

3.4.1 Characterization of a multiply scattering sample

The propagation of light through a multiply scattering medium can be treated via the diffusion approximation in which the measurement of the transport mean free path l_t and diffusion constant D (the rate at which diffuse waves spread over the medium) are crucial for the characterization of the media. As it was mentioned, the temporal behavior of the output speckle field can be used for determination of the diffusion properties. One of the goals of this chapter is the measurement of the diffusion constant from the spatio-temporal speckle pattern.
In this part, I will show the experimental results of spatio-temporal characterization of the multiply scattered light transmitted through a turbid medium using FTSSI. This measurement is a prerequisite for controlling (spatio-temporal focusing) the transmitted light which will be detailed in Section 3.4.2. Furthermore in this part, I will show the simple method of extraction of the diffusion constant D through measurement of the Thouless time $\tau_d \approx L^2/\pi^2 D$ [184] where L is the sample thickness. The characteristic diffusion or Thouless time is the longtime decay rate of the energy density of diffuse light in the sample [212] which can be extracted from exponential decay of the measured transmitted intensity pattern.
This part consists of two subparts. In the first subpart, I measure the spatio-spectral and spatio-temporal behavior of the transmitted light at a single sample position. I also measure the spatio-spectral autocorrelation function of the reconstructed complex electric field that contains information about the dynamics of the diffusion process. In the second subpart, I average the transmitted intensity of the different sample positions to obtain the averaged transmission. The averaged behavior yields the characteristic diffusion time of the sample, by an exponential fitting to the intensity decay. I subsequently extract diffusion constant D from measured decay time. I then check the accuracy of this value by comparing it with D measured by contrast technique [179].

Single sample position measurement

This part is devoted to spatio-spectral and spatio-temporal measurements of the multiply scattering sample. Figure 3.9 shows the reconstructed intensity (a) and wrapped

phase (b) of the speckle pattern in the space and frequency domains. The precision of the phase at the peak of the signal is 0.1 rad. It is estimated by computing the standard deviation of the inferred sample phase over 5 accumulated images. Figure 3.10 shows the computed standard deviation of the inferred spectral phase of the sample arm. Furthermore, the precision of the sample amplitude and phase for the case where the sample is removed is also estimated by computing the standard deviation over 5 accumulated images. The signal to noise ratio of the sample amplitude at its peak value is approximately 100 and the relative phase error is approximately 0.05 rad. Figure 3.9(c) shows three sample spectral lineouts of the intensity. For different positions, the intensity of the transmitted pulse is distorted differently. The blue dashed line in Fig. 3.9(c) shows the intensity integrated along the spatial axis of the pattern which resembles the spectrum of the initial source. The spectral phase lineouts from the indicated positions of the speckle pattern are extracted Fig. 3.9(d). These figures indicate that each point on the speckle pattern possesses random spectral phase and intensity due to the multiply scattering phenomena. Furthermore, it shows that spatially averaging the phase and intensity (i.e. for a non-imaged measurement) will wash out useful spectral phase and amplitude information relevant for meaningful diagnosis of the scattering process or the pulse compression experiments.
The scattering process is dispersive. Therefore, different frequencies produce different speckle fields. As the frequency of the scattered laser light is scanned, the amount of frequency changes over which a new uncorrelated speckle field is produced, defines the bandwidth of that particular medium. In the temporal domain, this corresponds to the temporal intensity distribution of the scattered pulse. Intuitively, one can consider that some portions of the pulse are scattered into shorter or longer paths through the sample, producing a range of exit times. This motivates the measurement of the bandwidth via the spectral autocorrelation length. Figure 3.9(e) shows the calculated spatio-spectral correlation function of the complex electric field $E(\Omega, Y) = |\langle E_{out}(\omega, y) E^*_{out}(\omega + \Omega, y + Y)\rangle|$ for the sample with thickness of 20 μm. The spatial autocorrelation length on the CCD camera is 57 μm at FWHM, giving an idea of the averaged grain size of the speckle. The spectral bandwidth of 1.76 mrad/fs at FWHM is measured from which the diffusion constant D can be extracted [184].
The spatio-temporal transmitted intensity can be reconstructed from the Fourier transform of the spatio-spectral complex electric field along the frequency axis. Figure 3.11(a) shows the reconstructed spatially resolved temporal speckle pattern of the scattering sample. This complex structure rises from the interference of the

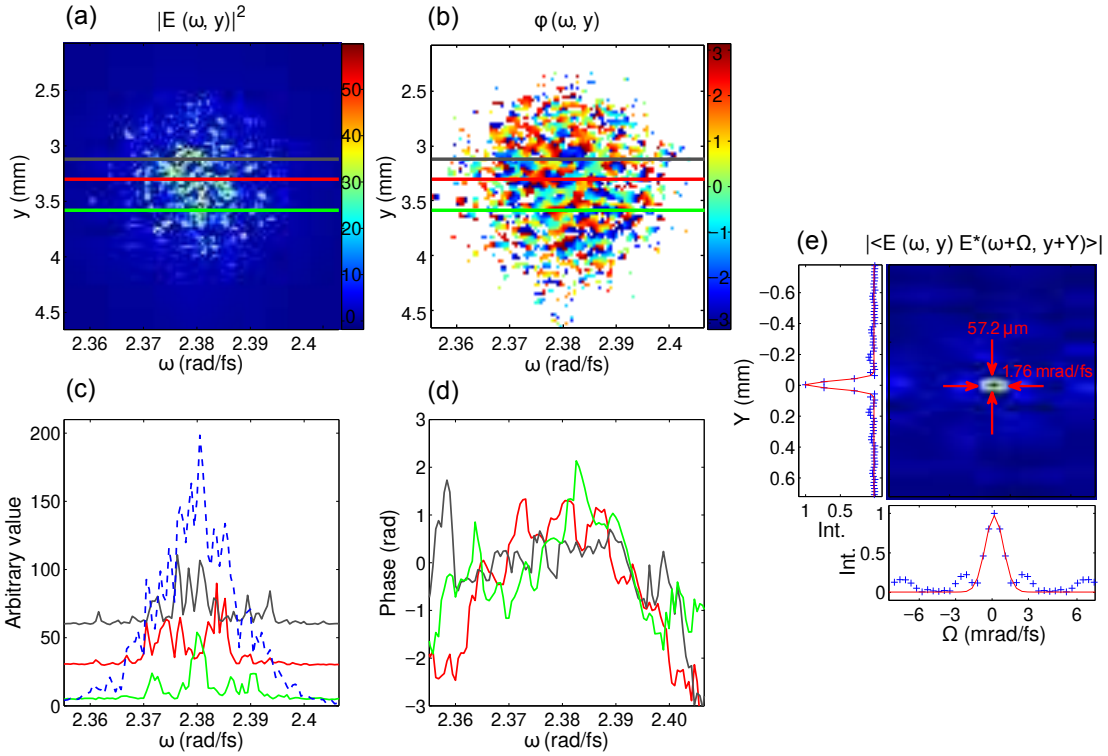

Figure 3.9: *Experimental reconstruction of the spatio-spectral electric field of the scattered-transmitted light from a thick scattering sample consisting of ZnO grains. (a) Spatio-spectral intensity $|E(\omega, y)|^2$ of the speckle. (b) Speckle spatio-spectral phase $\phi(\omega, y)$. (c) Solid lines: Spectral intensities at the different indicated positions of the speckle; blue dashed line: spatially integrated spectral intensity. (d) Spectral phases at different positions of the speckle. (e) Spatio-spectral correlation function $|\langle E_{out}(\omega, y) E^*_{out}(\omega + \Omega, y + Y)\rangle|$ demonstrating that the speckle is well resolved both spatially and spectrally. The spatial correlation length is related to the speckle grain size, while the spectral correlation length is the bandwidth of the medium, inversely proportional to the Thouless time.*

multiply scattered electric field which bears a resemblance to the complex structure of the Fig. 3.9(a) in spectral domain. Temporal profiles from different spatial positions of the speckle are plotted in Fig. 3.11(b). From these results one can measure the transmitted pulse duration at different positions of the speckle. I will show in next subsection that by measuring the spectral phase of a chosen point of the speckle and applying its inverse to the sample, one could observe a temporal focusing of the light at that point. Spatial resolution of the measurement is a prerequisite for this measurement, otherwise the real spectral phase information at the selected point will be washed out. The dashed blue line in Fig. 3.11(b) shows a spatial integration of the speckle field, which clearly demonstrates the temporal stretching of the pulse via

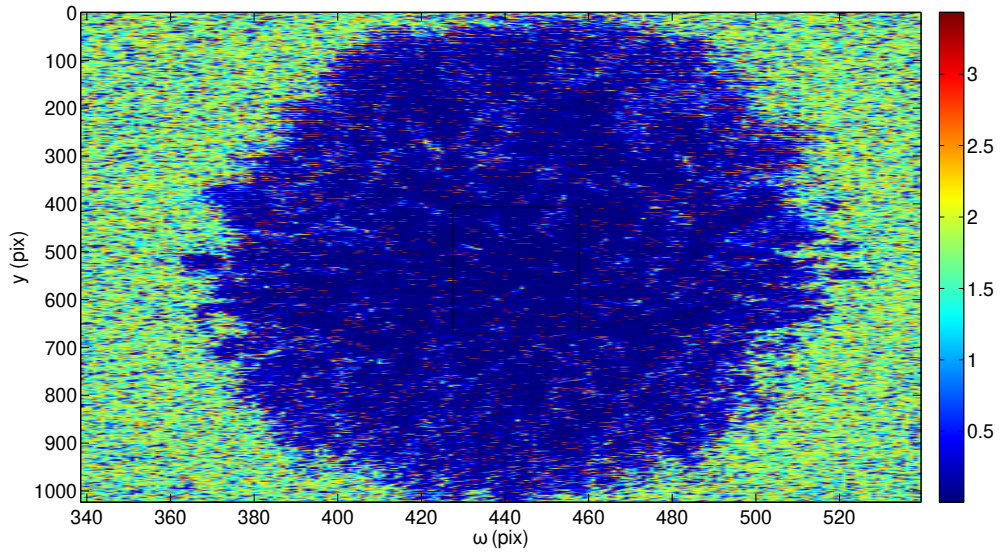

Figure 3.10: *Standard deviation of the inferred sample spatio-spectral phase. The magnitudes of the random errors is estimated by computing the standard deviation of the inferred sample phase over 5 accumulated images. The phase error is approximately 0.1 rad obtained from 10% of the peak of the signal (black rectangle).*

the multiple scattering events in the sample. In order to carry out a comprehensive study of speckle properties, such as vortices and singularities [213], a complete 3D measurement (i.e. both spatial dimensions with spectral resolution) is required. This can be accomplished by transversely scanning the position of the spectrometer slit relative to the beams (sample and reference) falling upon it.

Ensemble sample position measurement

Though the scattering process produces complex spatio-temporal intensities that vary in a complex manner as the details of the experimental alignment are varied, as explained above, the average temporal behaviour provides an insight into the properties of the sample. To achieve this, an ensemble-averaged measurement of the temporal profile is taken: the sample is mounted on a translation stage and the measurement is repeated over a pre-defined grid of sample positions, comprising 40 points spaced every 50 μm over a 2 mm range, and in a randomly determined order. The ensemble-average spatio-temporal intensity for 40 measurements is depicted in Fig. 3.12(a) and (c) respectively for 17$\pm$1 μm and 20$\pm$1 μm thick samples. The spatial integration of the position-averaged intensities yields the averaged transmission intensities, which are plotted in Fig. 3.12(b,d). This information may be considered as an ensemble average of the information contained in Fig. 3.11, since displacing the sample in the

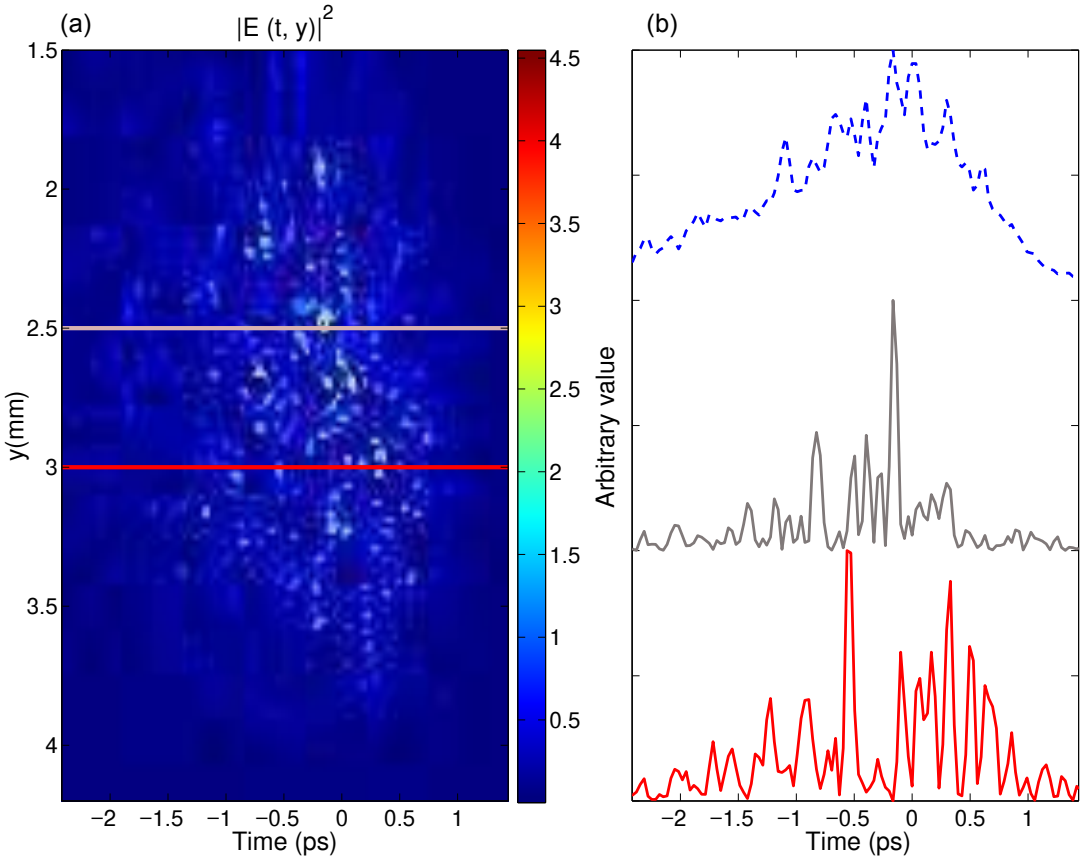

Figure 3.11: *Spatio-temporal intensity of the scattered, transmitted light from 19 μm thick sample. (a) Reconstructed spatio-temporal intensity $|E(t,y)|^2$ of the speckle from Fourier transform of the complex spatio-spectral electric field. (b) Solid lines: temporal intensities along the differently colored spatial slices of (a); Dashed line: spatially integrated temporal intensity.*

laser beam exposes an independent distribution of scatterers to the light field. Thus greater precision is obtained for the lifetime measurements, since the ensemble average washes out the random fluctuations of the speckle field whilst leaving the underlying statistical properties. By applying a negative exponential fit to the intensity decay, the characteristic diffuse times τ_d are extracted to be 1046±10 fs and 1233±10 fs for the 17 μm and 20 μm thick samples respectively. Inferred from $\tau_d \approx L^2/\pi^2 D$, the diffusion constant for the thin and thick samples are 28.5±4 m^2/s and 32±4 m^2/s respectively which shows that the results are self-consistent and also in good agreement with D=29 m^2/s obtained from contrast technique.

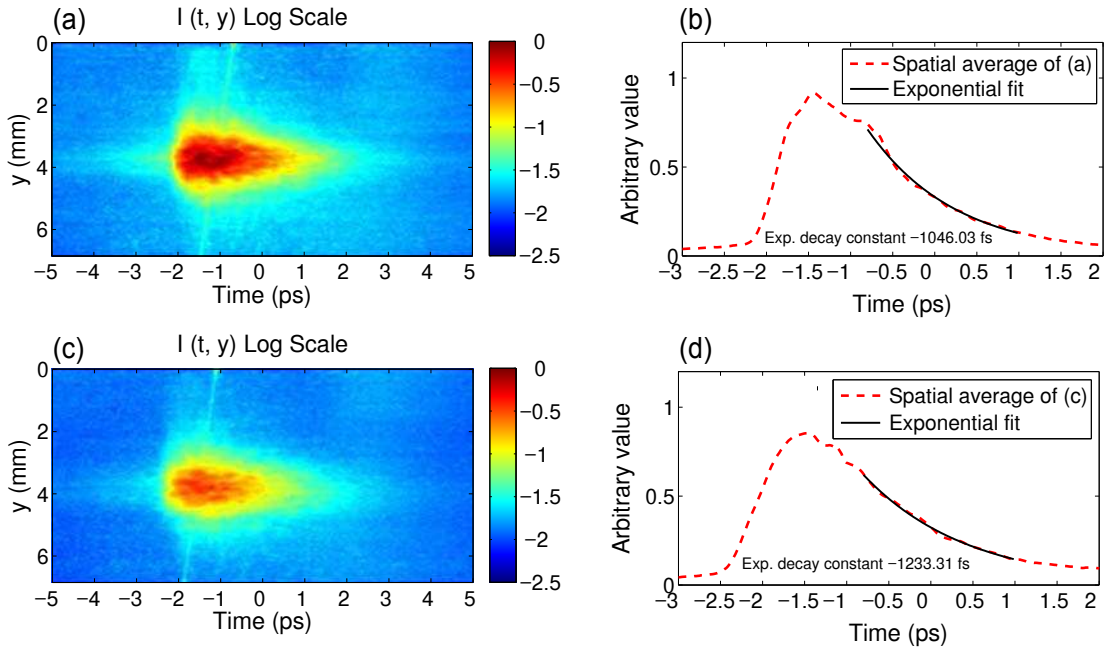

Figure 3.12: *Position averaged spatio-temporal intensity $I(t, y)$. (a) Ensemble-average of spatio-temporal intensity from forty different positions of the sample with thickness of 17 µm. (b) Spatially integrated ensemble-averaged spatio-temporal intensity of figure (a). An exponential fit of the intensity decay yields a sample decay time of 1046 fs. (c) Position average of the spatio-temporal intensity from forty different positions of the sample with thickness of 20 µm. (d) Spatially integrated ensemble-averaged spatio-temporal intensity of figure (c). The decay time of the sample is 1233 fs.*

3.4.2 Spatio-temporal control of the ultrashort pulses behind multiply scattering medium

As was mentioned in the analytical description, the prerequisite for the spatio-temporal control is the spatially resolved spectral phase measurement. In the previous part, I showed the possibility of performing such measurement using FTSSI technique. Here, in the control part, the difference of the experimental setup compared with the characterization part is the replacement of the laser source by a source with broader spectral bandwidth and addition of the pulse shaper on the sample arm. Therefore, in the measurement of the spatio-spectral electric field one would observe a minor modification which is due to the application of laser source with broader spectral bandwidth. Figure 3.13(a) shows the intensity and Fig. 3.13(b) shows the phase of a typical spatio-spectral speckle field $E_{out}(\omega, y)$ as measured by FTSSI. The spatio-spectral speckle is clearly demonstrated and the complex structure of $E_{out}(\omega, y)$ is fully resolved in both phase and intensity. This structure is also visible in the one-

dimensional spatial [Fig. 3.13 (a), red, solid] and spectral [Fig. 3.13 (a), green, solid] 'lineout' slices. The integrated projections of the speckle intensity [Fig. 3.13 (a), dotted lines], however, show that a spectrally unresolved speckle image, as measured on a camera, would yield a strongly reduced contrast, while a non-imaging spectral measurement would only yield the initial source spectrum (Hyper Gaussian profile). This further motivates the necessity of a spatially resolved phase measurement for the temporal focusing experiment described before. Meanwhile the spectral phase reveals a similar complex structure [Fig. 3.13 (b)]; as a consequence, it is clear that a spatially averaged phase measurement offers no utility for pulse recompression. A Fourier transform of the complex field along the spectral axis gives the spatially resolved temporal behavior of the speckle $E_{out}(t, y)$ [see Fig. 3.14(a)]. This spatio-temporal field exhibits the same complex speckle structure as before, as evinced by both the three-dimensional plot and the spatial (red) and temporal (black) lineouts projected onto the walls. The spatially (black) and temporally (red) integrated fields are plotted above; the former reveals the confinement time, which is fitted as approximately 2.5 ps, in good agreement with the spectral bandwidth measured from the autocorrelation function [Fig. 3.13 (c)]. For this function, the spatial and spectral correlation distances at the spectrometer were 50 μm (corresponding to 3.6 μm in the object plane) and 2.55 mrad/fs, respectively.

In order to spatio-temporally control the distorted pulses behind the sample, we choose a spatial slice y_0 from the measured complex spatio-spectral electric field. Then we program the inverse phase of the chosen slice to the pulse shaper. The input shaped pulse propagates through the sample and results in a new spatio-spectral speckle. A Fourier transform of the output shaped spatio-spectral electric field along the spectral axis is shown in Fig. 3.14 (b). Confirming the analytical hypotheses and numerical simulations, we can observe the emergence of an intense peak at the position of chosen spatial slice y_0 (an intense temporally focused and spatially localized pulse). The shaped pulse is found to have a full width of half-maximum duration of 59 fs (close to the transform-limited duration of 54 fs). The optimal phase is reached after two iterations of the feedback procedure. The peak temporal intensity has a contrast ratio of 15 relative to the average background before compensation, and the average background along y_0 is reduced by a factor of 2. As shown by the projected 'lineout' intensities, the temporal focus is spatially localized; the localization distance is 30 μm which is commensurate with the correlation distance of Fig. 3.13(c). The spatially integrated temporal field (Fig. 3.14, top, black), exhibits the redistribution of

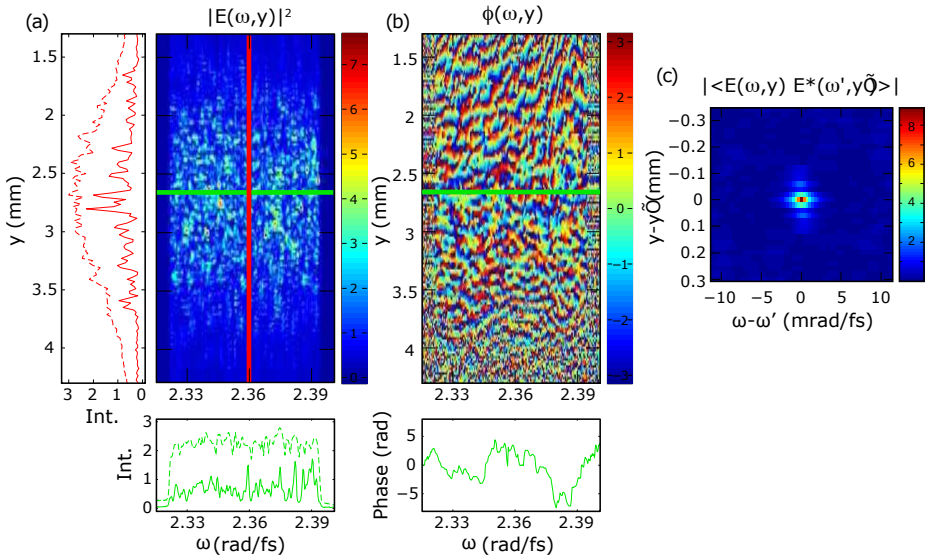

Figure 3.13: *Experimental reconstruction of the spatio-spectral speckle electric field $E_{out}(\omega, y)$ after propagation through a multiply scattering medium. (a) Speckle intensity $|E_{out}(\omega, y)|^2$, with respective projections onto the spatial (red) and spectral (green) axes—individual slices (solid lines) and integrated signals (dashed lines) are considered. (b) Speckle phase $\phi_{out}(\omega, y)$, along with a spectral phase measurement $\phi_{out}(\omega, y_0)$ localized along a single spatial slice. (c) Autocorrelation function $|\langle E_{out}(\omega, y) E^*_{out}(\omega', y')\rangle|$, demonstrating that the speckle is well resolved both spatially and spectrally. The spatial correlation length is related to the speckle grain size, while the spectral correlation length is the bandwidth of the medium, inversely proportional to the Thouless time.*

the temporal intensity after shaping that is the signature of a temporal focus. The temporally integrated field, however, is not altered (Fig. 3.14, top, red): the peak can be said to be spatially localized rather than focused. Due to the spatially localized nature of the phase compensation, the peak integrated temporal intensity is not significantly altered. As shown in time reversal and wavefront shaping experiments, another striking feature is that the more scattering the medium is, the more efficient the focusing will be. Indeed, the signal-to-noise ratio is governed by the ratio of the Thouless time of the medium over the initial duration of the pulse, i.e. the number of independent spectral degrees of freedom. Furthermore, in contrast with conventional phase compensation techniques, here all shaping imperfections affect the signal-to-noise ratio; the temporal duration and spatial localization are limited by the Fourier-limit duration and autocorrelation size of the speckle respectively [166].

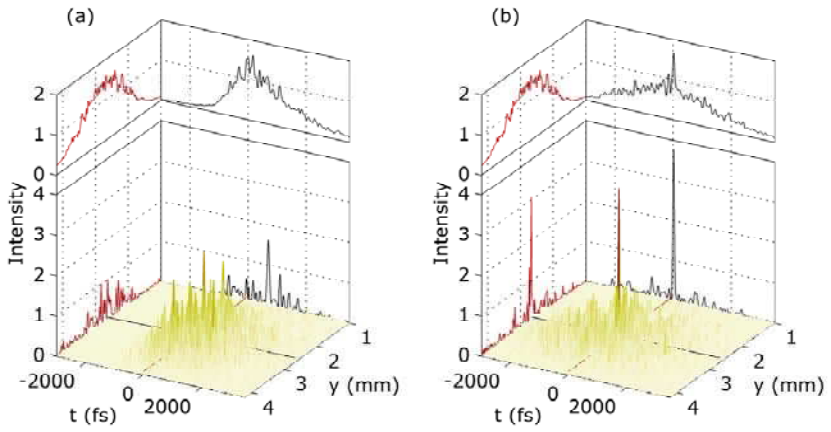

Figure 3.14: *Spatio-temporal focusing. Reconstructed spatio-temporal intensities* $|E_{out}(t, y)|^2$ *(a) before and (b) after compensation of the phase at y0 = 2.66 mm. An intense peak emerges from the background with a contrast ratio of 15. One-dimensional 'lineouts' at the location of this peak (projections onto walls) and integrated signal (top) show that the peak is focused in time (black) and localized in space (red). The temporal and spatial widths of the peak are the Fourier-limit pulse duration and the spatial phase correlation distance, respectively.*

3.5 Comparison between spatial shaping and spectral shaping

I have previously described our technique of focusing light pulses in space and time through a multiply scattering medium that is based on spectral shaping of the input pulses. At the same time Katz *et al.* [177] and Aulbach *et al.* [178] showed the possibility of obtaining similar results (spatio-temporal focusing) by spatially shaping the input pulses. Before comparing their results with ours, I describe the principle of their works. Both groups, as in the work of Vellekoop [29], adaptively optimized the wavefront phase of the input pulse using a two dimensional SLM. The only difference between both demonstrations is the detection technique of the signature tightened spatio-temporal signal.

Katz *et al.* applied a two-photon fluorescent material (2PF) placed behind the scattering medium which was imaged by an electron-multiplying charge-coupled device (EMCCD). They maximized a nonlinear two photon signal at a selected point of the out speckle instead of maximizing the optical intensity. Because of the nonlinearity of 2PF process it is sensitive to both the spatial and the temporal form of the exciting field. Therefore, they used a practical technique of simultaneous measurement of the

pulse focusing along space and time domains.

Detection in the work of Aulbach *et al.* was done by heterodyne interferometry. In other words, a pinhole was applied to choose a output speckle grain. The speckle grain was overlapped with a frequency shifted reference pulse and sent to a photo-detector enabling heterodyne detection of the transmitted pulses [214]. Figure 3.15 (a),(b) shows the spatio-temporal speckle pattern before and after compensation. By using a learning optimization algorithm, distorted pulse in space and time is corrected and forms a spatio-temporal focus. In both experiments spatial control alone was sufficient for simultaneously correcting both spatial and temporal distortions in scattering media. This is because the scatterer couples the spatial and temporal degrees of freedom. In more detail, the electric field of a specific output mode is a superposition of the pulse responses from each input mode. The impulse response corresponding to a pair of input-to-output mode has a random structure shown in Fig. 3.15 (c). Therefore a superposition of whole random impulses responses results in a temporal speckle. Using a SLM and shifting the optical phases of corresponding impulse responses, researchers forced the uncorrelated contributions to become correlated and reinforced each other at the specified position in space and time. The spatial focusing was limited to the spatial correlation area which is only dependent to the scatterer. The ratio between the time integrated intensity of the pulse (energy) at the focusing position and the energy of non optimized pulse at the same position can be interpreted as spatial focusing. In more detail, this means that overall more light is transmitted into the detected channel. Katz obtained two-photon enhancement of 800 or 20-fold gain of the speckle intensity.

There are two major differences between our results which is based on spectral shaping and those works. Spectral shaping manipulates the arriving time of the different frequency modes at a single speckle grain without manipulating the transmission channels. Therefore temporal speckle is temporally recompressed to its Fourier limit and no energy enhancement occurs (the ratio of temporal integration of optimized pulse to unoptimized at the location of enhancement). This can be interpreted as temporal focusing and spatial localization. In spatial shaping both energy enhancement and temporal recompression happens which can be considered as spatio-temporal focusing. This ability to temporally recompress the pulse without spatial redistribution of energy may have important applications for the nonlinear imaging of biological samples, where a rise in fluence may result in the onset of thermally induced damage. The next major difference is about the duration of the optimization process. Since

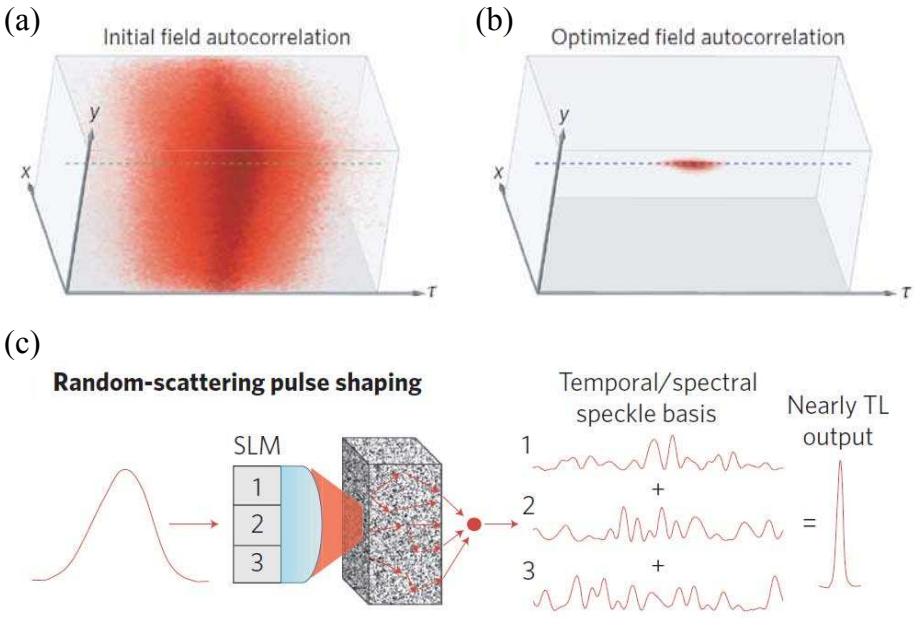

Figure 3.15: *Principle of spatio-temporal focusing using an optimization algorithm. (a) and (b) show the spatio-temporal speckle before and after compensation respectively. Optimization results in a spatial focusing and temporal recompression of the pulse at intended point behind the sample. (c) For each pair of input and output modes there exists a channel with specific impulse response. The impulse responses corresponding to each of input modes are randomized and their linear contribution in a single output mode results in a temporally randomized pattern. Controlling the phase of each impulse response yields a temporally and spatially focused pulse at the intended output mode. This figure is adopted from Ref [177].*

spatial shaping is based on learning algorithm and the response time of the SLMs are currently slow, this process takes longer time than our technique which is based on a single measurement and optimization (open loop control). This can be considered as an important advantage for our technique when the optimization should take place in the dynamic media.

3.6 Conclusion and future directions

In conclusion, we have characterized the speckle spatio-temporal electric field of a multiply scattered ultrafast pulse. We have also extracted the diffusion properties of the scattering sample from the inferred electric field. Furthermore, we have implemented an open-loop correction of the spectral phase in order to produce a naturally Fourier and diffraction-limited pulse after the medium at a chosen position. The results demonstrate the benefits of a spatially resolved measurement: typical control

experiments consider a spatial average, but for such systems that lack large-scale correlations such averaged measurements are valueless. Moreover, we have demonstrated that these correlations permit spatial control without spatial resolution in the spectral pulse-shaper. Our study branches out previous spatial-speckle shaping techniques to the temporal domain and bridges the gap with time-reversal experiments in acoustics and electromagnetism. This capacity to recover a short pulse on a selected spatial speckle point has important potential applications for quantum control and photonics, as well as for the fundamental studies of complex media. It suggests that ultrafast diagnostic techniques including nonlinear microscopy and time-resolved spectroscopy may be performed deep within or beyond biological tissue, beyond the range of ballistic photons. Moreover, our characterization technique can be applied in studying of the whole speckle properties, such as vortices and singularities [215]. This requires a complete three-dimensional (3D) measurement (i.e., both spatial dimensions with spectral resolution) which can be accomplished by transversely scanning the position of the spectrometer slit relative to the beams (sample and reference) falling upon it. One of future directions of our studies is studying the effect of scattering media on entangled photons. Specifically one may exploit the spatial and spectral coupling effect of the scatterer and convert the spectral entanglement to spatial entanglement. The other major direction is to perform a time reversal at optical frequencies that makes the control faster, and more simple. There have been several theoretical proposals for achieving time reversal at optical frequencies. Spectral phase conjugation using four wave mixing [198] or spectrally resolved holography [216] are good potential candidates for this goal. Recently several theoretical works demonstrated the possibility of time-reversing optical pulses using various methods such as dynamic modulation of a zero gap periodic system [217] or manipulating the refractive index of dielectric photonic crystals [218].

Conclusion

During my thesis in the CAR laboratory, I have studied the full spatio-spectral characterization of pulse shapers and their application in controlling spatio-temporal scattered light.
Shaped femtosecond pulses are in widespread demand among the quantum control community. During the last two decades, different techniques of pulse shaping have been developed; however all these techniques suffer from space-time couplings. In order to apply such pulse shapers in the community, their relevant coupling effects should be completely characterized. The limitations of the pulse shapers based on 4f zero-dispersion line have been widely studied and documented; however, the Acousto-Optic Programmable dispersive filter (AOPDF) pulse shaper, an alternative method of pulse shaping, is less well characterized.
During my thesis, I have comprehensively studied and characterized the space-time couplings within the UV-AOPDF pulse shaper using Fourier Transform Spatio-Spectral Interferometry. FTSSI is a strong referenced interferometric technique which reveals the full transfer function of the pulse shaper. Using this device, I have found that the different programmed pulse shapes, which are commonly used in coherent control experiments, are highly reliable (perfect consistency between the programmed and measured pulse shapes). Furthermore, I have found that all shaped pulses suffer from a single spatio-temporal coupling which is group dependent spatial displacement. The physical mechanism behind this single spatio-spectral coupling was found to be the combination of geometrical and birefringent walk-off effects.
Our results were the first to demonstrate, quantify and explain a parallel effect in this alternative device.

From a control perspective, this manuscript shows the ability of spatio-temporal refocusing of a broadband pulse that has been strongly distorted by a random, multiply scattering medium. The measurement and consequently control of the complex elec-

tric field of the optical frequencies is a challenging task. We have overcome this challenge and have performed such corrections for the first time.
I have demonstrated this via a spatially resolved measurement of the spectral phase of the distorted pulse followed by open-loop feedback to a pulse shaper. The measurement was done by the FTSSI technique and as a result of the linearity of the scattering process, the pre-compensation formed a spatially localized flat output spectral phase and hence a short pulse. Furthermore, by using FTSSI technique, I have spatio-spectrally characterized the speckle pattern and extract the diffusion properties of the medium from this measured speckle.
An extension of our 2D to 3D measurements, which is feasible by scanning the spectrometer slit, can be regarded as a strong tool for studying of the whole speckle properties, such as vortices and singularities. Furthermore, the ability to recover the ultrashort pulses, temporal shape (the transform limited duration) at a desired position can smooth the way for performing coherent control, time resolved spectroscopy and nonlinear microscopy experiments within or beyond biological samples, beyond the range of ballistic photons. Since the scattering medium couples the spatial and spectral modes of the light, an other interesting future direction would be to study the effect of such a medium on entangled photons. In more detail, due to such couplings, one would expect to be able to convert the spectral entanglement to a spatial one.

Appendix A

Résumé en français

A.1 Introduction

Les principales évolutions qui ont conduit à notre compréhension de la lumière et des phénomènes optiques, a eu lieu il y a longtemps. Avant la découverte du laser, il semblait peu probable que d'importants changements se produiraient. L'arrivée du laser a marqué un nouveau départ : La publication de plus de 5000 articles dans les dix premiers ans après sa découverte est une preuve de son effet révolutionnaire sur la science fondamentale. En dehors de leurs applications dans la recherche fondamentale, les lasers sont aujourd'hui présents partout dans notre vie et la croissance de leurs applications ne semble pas s'arrêter. Ce qui rend la source laser unique, c'est sa cohérence, sa directivité et monochromaticité (ou alternativement courte durée).
La durée courte (correspondant à une large bande spectrale) est la propriété principale des lasers femtosecondes. Ce ci a permis d'ouvrir de nouvelles frontières dans la recherche fondamentale et pour les applications. Par exemple, grâce à leur durée ultracourte, le laser femtoseconde permet d'avoir accès à la dynamique électronique des molécules à l'aide de ce qu'on appelle les techniques pompe-sondes [1] et en modifiant les paramètres du laser de contrôler cette dynamique. C'est le domaine du contrôle cohérent [2]. Leur grande largeur spectrale a été mis à profit de façon tout à fait original en métrologie des fréquences ce qui a donné le prix Nobel de physique à J.L. Hall et T.W. Hansch [3–7]. La seconde propriété des lasers femtosecondes est la concentration de l'énergie du laser sur des temps courts (femtoseconde) permettant en focalisant de tel laser d'atteindre des densités de puissance extrêmes. Cependant, une tâche difficile est la caractérisation d'impulsions femtosecondes

sachant que les détecteurs existants ont au mieux un temps de réponse de quelques picosecondes. Pour palier à cette question différentes techniques basées sur des processus non-linéaires ont été mis en œuvre. Les exemples incluent SPIDER [8] et FROG [9] des techniques qui sont maintenant disponibles dans le commerce dans divers domaines spectraux.
En générale, toutes les méthodes de caractérisation d'impulsions reconstruisent l'ensemble du domaine temporel électrique ou de l'intensité des impulsions (en moyenne sur le profil spatial) sans fournir d'informations sur leurs caractéristiques spatiales. Le champ électrique reconstruit ne tient pas compte du couplage spatio-temporel. Lorsque les effets de couplage spatio-temporel sont présents, chaque position dans l'espace sur le long du front d'onde d'impulsion aura ses propres propriétés temporelles spécifiques. Ces couplages, qui sont dus à l'importante largeur spectrale des impulsions, sont généralement introduits pendant la propagation dans les différents éléments optiques. Ces couplages peuvent brouiller la résolution temporelle, réduire l'intensité et modifier par exemple les résultats d'une expérience de contrôle. Cependant le couplage entre l'espace et du temps peut être exploité à des fins spécifiques par exemple pour élargir la bande spectrale d'impulsions en utilisant des techniques de conversions optiques non linéaires [10]. Afin de bien comprendre et de contrôler ces couplages spatio-temporels, une étude systématique et une caractérisation de ces couplages et leurs sources sont nécessaires. C'est l'objet d'une partie de ma thèse. Cela peut se faire soit par une extension des techniques conventionnelles de la caractérisation temporelle dans le domaine spatial ou par l'invention de nouveaux instruments indépendants. Nous avons choisi d'utiliser la technique basée sur l'interférométrie spatio-spectrale par transformée de Fourier [Fourier Transform Spatio-Spectral Interferometry(FTSSI)] en raison de ses nombreux avantages qui seront détaillés dans ce manuscrit [11]. Il existe d'autres techniques pour la caractérisation de tels couplages comme par exemple, SEA-SPIDER et SEA-TADPOLE. Nous dresserons une vue d'ensemble des avantages et inconvénients de ces techniques.

Sur l'échelle de la femtoseconde, de nombreuses interactions dépendent de la forme temporelle particulière de l'onde appliquée. Ainsi pour le contrôle cohérent [12–15], la compression d'impulsion [16], la microscopie non linéaire multidimensionnelle [17], les communications optiques [18] ou la factorisation des nombres [19–21], il est souhaitable et nécessaire de modifier les impulsions de la source d'une manière bien

définie afin d'atteindre le but souhaité. Alors que façonnage des impulsions nanosecondes et picosecondes peut se faire directement dans le domaine temporel à l'aide de commutateur rapide comme les modulateurs électro-optiques, pour le façonnage des impulsions femtosecondes, on doit recourir à des techniques indirectes tout optiques travaillant dans le domaine spectral. De ce fait les dispositifs de façonnages sont des sources importantes de couplage spatio-temporel. Une étude de ces couplages est donc nécessaire. Des études approfondies de façonneurs d'impulsions basées sur ligne 4f configuration ont été effectuées par plusieurs groupes [11, 22–26]. Cependant, aucune étude complète du façonneur d'impulsions basées sur la techniques Acousto-Optic programmable Dispersive Filter (AOPDF), n'avait été faite et c'est l'objet d'une partie des résultats de cette thèse. Ces façonneurs présentent l'avantage d'une large gamme d'accordabilité, très utile dans les expériences de contrôle cohérent. Cette thèse produit une étude détaillée de la caractérisation spatio-temporelle complète de l'UV-AOPDF au moyen de la technique FTSSI.

La mise en œuvre de l'utilisation des propriétés formidables des lasers femtosecondes est mise à mal dans les échantillons biomédicaux en raison de leur index de réfraction inhomogène. En d'autres termes, le profil spatial et temporel des impulsions incidentes est fortement perturbé lors de la propagation à travers l'échantillon. Différentes techniques ont été développées pour corriger les distorsions spatiales des lasers continus tant dans des échantillons minces [27, 28] que dans des échantillons épais [29].
En régime pulsé, le contrôle ou en d'autres termes la correction du profil spatial et temporel a été démontré dans le domaine des ondes acoustiques en utilisant des expériences de retournement temporel (time reversal) [30–33]. Cependant, en raison de la difficulté à mesurer le champ électrique complexe dans le domaine des fréquences optiques, ces techniques sont restées inaccessibles jusqu'à notre travail. Durant cette thèse, nous avons caractérisé l'amplitude et la phase spectrales des impulsions en sotie d'échantillon permettant d'effectuer des expériences de retournement temporel dans le domaine optique [34, 35]. Comme le milieu diffusant couple les domaines spatial et temporel, nous avons obtenu à la fois une concentration spatiale et temporelle de l'impulsion par seulement la mise en forme phase spectrale des impulsions d'entrée. C'est l'objet du troisième chapitre du manuscrit.

Ce manuscrit est organisé comme suit:

- Le premier chapitre (dispositifs expérimentaux) présente brièvement la source laser et les appareils expérimentaux, y compris la mesure des impulsions femtosecondes et techniques de façonnage que j'ai fréquemment utilisé au cours de ma période de doctorat en LCAR.

- Le deuxième chapitre (couplage spatio-temporel) est consacré à une caractérisation complète des effets de couplage espace-temps produit par le façonneur d'impulsion UV-AOPDF. D'abord, il commence par une description mathématique des couplages entre espace et temps. Puis il passe en revue l'état actuel de l'art des techniques de caractérisations spatio-temporelles. Enfin, il présente les résultats expérimentaux concernant la caractérisation complète de couplage spatio-temporel d'impulsions UV façonnées par AOPDF et l'origine physique de ces couplages spatio-temporels.

- Le troisième chapitre porte sur la caractérisation spatio-temporelle et le contrôle des impulsions femtosecondes transmises par un milieu diffusant. Tout d'abord l'état actuel des expériences de contrôle de speckle est présenté. Puis, une analyse et une description numérique du contrôle via une mise en forme spectrale des impulsions d'entrée est développée. Ensuite, le dispositif expérimental que nous avons utilisé pour étudier et contrôler la lumière transmis est décrit en détail. Enfin, je présente les résultats expérimentaux, notamment la caractérisation spatio-temporelle des impulsions transmises et, plus important, le contrôle spatio-temporel des impulsions transmises par le milieu diffusant.

A.2 Couplage spatio-temporel de UV-AOPDF

Quand il existe une interdépendance entre les coordonnées spatiale (angulaire) et spectrale (temporelle) des impulsions ultracourtes, elles sont désignées comme des impulsions spatio-temporellement couplées. Ces couplages, qui sont visibles à cause de la largeur spectrale des impulsions ultracourtes, sont introduits au cours de la propagation dans des éléments optiques tels que des réseaux de diffraction, des prismes et de l'air. Ces couplages diminuent souvent la résolution temporelle, réduisent l'intensité et provoquent un large éventail d'autres problèmes. Par conséquent, afin de bien les comprendre et les maîtriser, nous avons entrepris de les caractériser et d'identifier leur origine.

Les façonneurs d'impulsions [57] induisent eux aussi un couplage saptio-temporel

qui peut etre gênant pour certaines expériences de contrôle cohérent. Des études approfondies des façonneurs d'impulsions basées sur ligne en 4f ont déjà été entrepris et il est maintenant bien connu à la fois expérimentalement et théoriquement que les impulsions façonnées de sortie de tels dispositifs sont spatio-temporellement couplées [11, 22–26]. Et leurs impacts sur les expériences ont été démontrés [66, 67]. En revanche, les façonneurs d'impulsion AOPDF qui ont de nombreuses applications dans les systèmes de CPA [97] et des expériences de contrôle [98], ont été moins bien caractérisés [26, 99–101]. Le chapitre 2 de ce manuscript est consacré aux effets de couplage spatio-temporel dans l'utilisation des façonneurs d'impulsions basés sur un cristal acousto-optique utilisable dans l'UV (AOPDF).

Un exemple de ces couplages est représenté sur la Fig. A.1 (a), où la position centrale du faisceau est mesurée en fonction du délai temporel programmé avec le Dazzler (AOPDF). Le faisceau se déplace de façon linéaire avec une vitesse du couplage de 0.249 mm/ps. La Fig. A.1 (b) est un second exemple qui montre l'effet de programmation d'un saut de phase pi. Celui-ci entraine un décalage spatial local de l'impulsion à la position correspondant à la fréquence du saut de phase. J'ai montré que ces effets sont attribuables à un seul mécanisme: un déplacement de l'impulsion mise en forme du au retard de groupe. Ces effets de " Walkoff " biréfringents et géométriques sont la cause physique de l'effet de couplage spatio-temporel indiqué dans ce façonneur d'impulsions. Nous avons démontré un excellent accord quantitatif entre les vitesses de couplage mesurées et calculées.

A.3 Caractérisation et Contrôle spatio-temporel des speckles

Les impulsions ultracourtes ont de nombreuses applications pour le contrôle cohérent [2, 15, 148–151], la spectroscopie résolue en temps [152], la microscopie non linéaire [153], etc. Travailler en milieu complexe nécessite de contrôle le profil spatio-temporel des impulsions. Or, il est bien connu que les milieux fortement diffusants déforment le profil spatio-temporel initial de la lumière.
En se propageant au travers d'un milieu diffusant épais, une onde monochromatique peu s'analyser par une partie balistique [154, 155] et une partie multiplement diffusée [156]. Les photons balistiques sont ceux qui voyagent à travers le milieu sans être déviés. Ils suivent une évolution exponentielle selon la loi de Beer [157]. Les

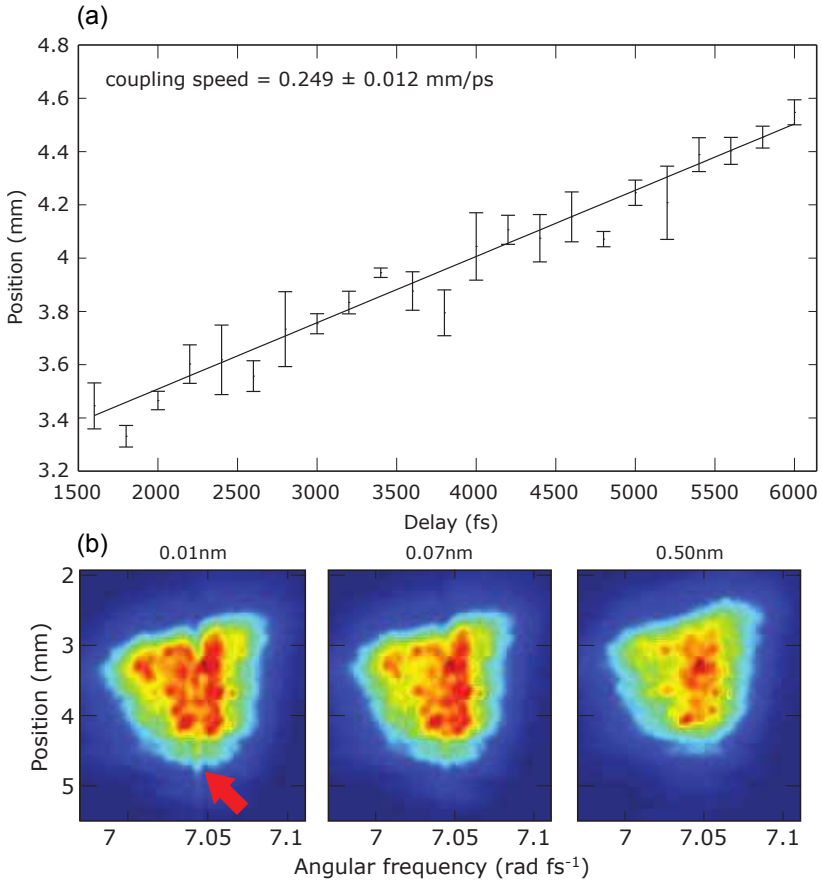

Figure A.1: *Les exemples de couplages spatio-temporels dans un AOPDF. (a) La position centrale du faisceau est mesurée en fonction du délai programmé avec le Dazzler (AOPDF). Le faisceau se déplace de façon linéaire avec une vitesse de couplage de 0.249 mm/ps. (b) Effet de programmation d'un saut de phase π. Celui-ci entraîne un décalage spatial local de l'impulsion à la position correspondant à la fréquence du saut de phase.*

photons multiplement diffusés donnent naissance à des figures de speckle spatial, dû à l'interférence constructive et destructive aléatoire des photons suivant des trajectoires différentes. A cause de leur caractère aléatoire, les photons multi-diffusés brouillent la phase optique de la lumière transmise. On parle de perte de cohérence. Ceci limite les potentialités d'imagerie, de focalisation, et de transmission des impulsions ultracourtes. De nombreuses solutions à ce problème ont été proposées en particulier autour de la détection des photons balistiques [158–164]. Cependant, pour un milieu diffusant avec des dimensions caractéristiques plus grandes que son libre parcours moyen l_t (la distance moyenne parcourue par la lumière avant d'être diffusée), ces techniques ne peuvent pas être utilisées parce que la composante balistique est fortement atténuée.

Récemment, Vellekoop et ses collègues ont démontré la possibilité de focalisation

spatiale [29, 165, 166] et donc d'imagerie [167] à travers de milieu diffusant en contrôlant les modes spatiaux de la lumière incidente en utilisant un modulateur spatial de lumière. La correction de la distorsion spatiale a été ensuite effectuée par d'autres groupes en utilisant des techniques alternatives [168–172]. Cependant, toutes ces techniques utilisent un laser quasi monochromatique et aucune correction temporelle n'a été rapportée.

La propagation des impulsions ultracourtes avec une large bande spectrale à travers des échantillons épais entraîne un étalement temporel additionnel et une modification du profil d'intensité qui donne lieu au speckle spectral (temporel) [173, 174]. Il est cependant possible de corriger ces effets inhérents à la propagation.

Il existe des techniques liées au contrôle dans le régime acoustique et électromagnétique GHz appelées méthodes de retournement temporel [31, 175, 176]. Cependant, notamment en raison de l'impossibilité de mesurer directement le profil temporel du champ dans le domaine optique, le retournement temporel dans le domaine optique reste difficile. Dans un travail parallèle (techniques différentes, mais des résultats similaires), notre groupe [35] et deux autres groupes [177, 178] ont réussi à contrôle spatio-temporellement l'impulsion ultracourte à la surface arrière d'un milieu diffusant. Pour atteindre cet objectif, nous avons appliqué la technique FTSSI afin de mesurer la phase spatio-spectrale du speckle permettant par une boucle de rétroaction sur un façonneur d'impulsions dans le domaine spectral de la contrôler. Cette mesure a permis de plus d'étudier le comportement temporel du champ de speckle, proposant ainsi une nouvelle technique de caractérisation temporelle de lumière multi-diffusée et par conséquent une nouvelle méthode pour la détermination des propriétés de diffusion de l'échantillon [179–189]. En effet nous avons démontré une technique simple d'extraction des propriétés de diffusion en utilisant notre technique bien établie FTSSI [34].

L'objectif de ce chapitre est d'étudier les caractéristiques spatio-temporelles des impulsions femtosecondes transmises par le milieu diffusant, l'extraction des propriétés de diffusion de ce milieu et, enfin, l'exploitation de ces mesures pour contrôler la lumière diffusée derrière l'échantillon.

Resultats et discussion

Dans l'expérience, une impulsion ultracourte est divisée en deux parties [voir la Fig. A.2]. Une partie du faisceau passe à travers un façonneur d'impulsion et est focalisée sur un échantillon multi-diffusant. La propagation de l'impulsion laser dans

l'échantillon (une couche épaisse de poudre de ZnO déposée de manière homogène sur une lame de microscope) donne lieu à un speckle spatio-temporel. Le speckle spatio-temporel est imagé sur la fente d'entrée d'un spectromètre d'imagerie en 2D [146]. L'autre partie du faisceau agit comme un référence et est recombinée avec l'impulsion qui a traversé l'échantillon à la fente d'entrée du spectromètre. L'angle entre les deux faisceaux ainsi que le delai entre les deux impulsions sont ajustables pour permettre d'optimiser la figure d'interférences ainsi obtenue. La technique SSI effectue une mesure relative de la phase spectrale entre l'impulsion de référence et l'impulsion multi-diffusée que l'on souhaite caractériser. L'amplitude et la phase de l'impulsion

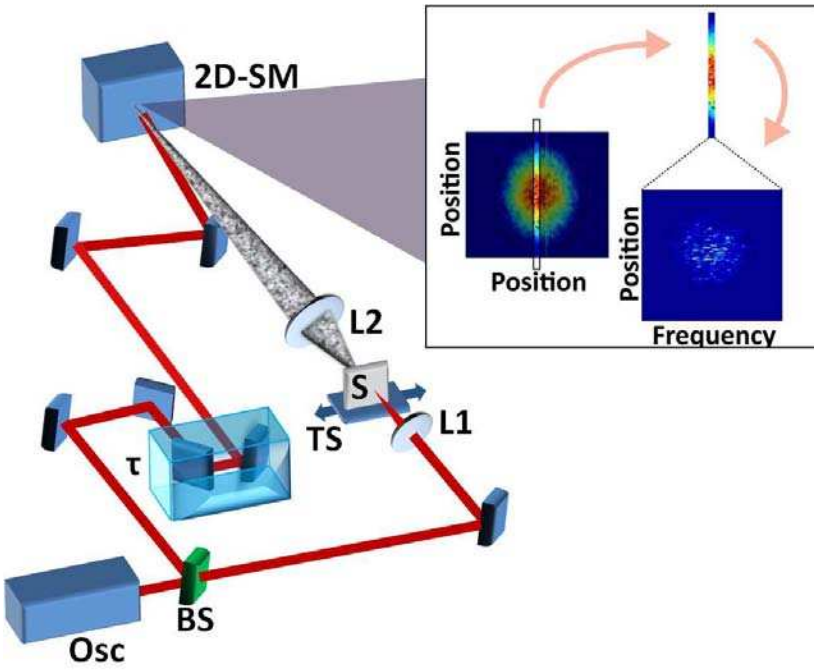

Figure A.2: *Dispositif expérimental. Le faisceau de l'oscillateur laser (OSC) est divisé en deux bras pour l'échantillon et pour la référence par une lame séparatrice (BS). Le bras de l'échantillon passe à travers un façonneur d'impulsion (PS) et est focalisé sur un échantillon multi-diffusant (s) par la lentille L1. La propagation de l'impulsion laser dans l'échantillon donne lieu à un speckle spatio-temporel. L'échantillon est monté sur une table de translation (TS) se déplaçant perpendiculairement par rapport au faisceau laser. Le speckle spatio-temporel est imagé sur la fente d'entrée d'un spectromètre d'imagerie 2D par la deuxième lentille (L2). L'autre partie du faisceau agit comme une référence et est recombinée avec l'impulsion qui a traversé l'échantillon, sur la fente d'entrée du spectromètre. L'angle entre les deux faisceaux ainsi que le délai entre les deux impulsions sont ajustables pour permettre d'optimiser la figure d'interférences ainsi obtenue. L'encart montre comment le spectromètre effectue une mesure d'intensité spectrale avec une résolution spatiale le long de la fente d'entrée.*

inconnue est extraite de l'interférogramme par filtrage de Fourier [86]. La figure A.3

montre l'intensité reconstruite (a) et la phase développée (b) du speckle dans les domaines spatial et spectral. Ces figures indiquent que chaque point du motif de speckle possède une phase spectrale et une intensité aléatoire en raison des phénomènes de diffusion multiple.

L'intensité spatio-temporelle transmise peut être reconstruite à partir de la trans-

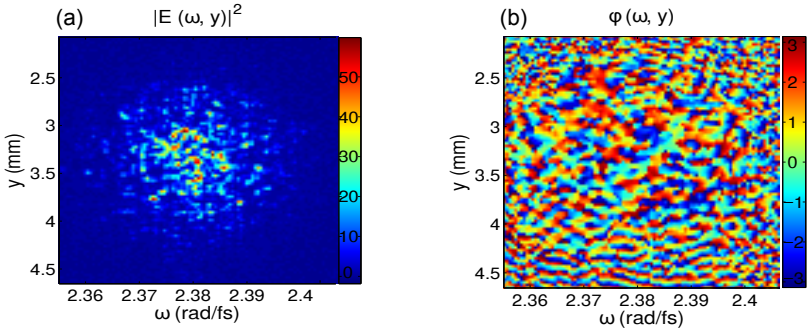

Figure A.3: *Reconstruction expérimentale du champ électrique spatio-spectral de la lumière diffusée pour un échantillon épais. (a) L'intensité spatio-spectrale* $|E(\omega, y)|^2$ *de speckle. (b) Phase spatio-spectrale de speckle* $\phi(\omega, y)$.

formée de Fourier du champ électrique complexe spatio-spectral le long de l'axe des fréquences. Le comportement moyen temporel fournit un aperçu des propriétés de l'échantillon. Pour ce faire, une mesure moyennée de l'ensemble du profil temporel est prise. La moyenne de l'intensité spatio-temporelle pour 40 mesures est représentée sur la Fig. A.4 (a). L'intégration spatiale de l'intensité qui moyennée sur la position donne l'intensité moyenne de transmission, est représentée sur la Fig. A.4 (b). Les moyennes permettent de s'affranchir des fluctuations aléatoires du champ de speckle laissant apparaître les propriétés statistiques de l'échantillon. En appliquant un fit exponentiel négatif sur l'intensité décroissante, le temps de Thouless est extrait à 1046 fs. La Fig. A.5 (a) montre le speckle spatio-temporel reconstruit de l'échantillon diffusant. La correction de la phase en un point choisi du motif à l'aide d'un façonneur d'impulsion conduit à une impulsion temporellement concentrée et spatialement localisée qui se dégage de l'arrière-plan du motif de speckle [Voir la Fig. A.5 (b)]. L'intensité du pic temporel est améliorée d'un facteur 15 par rapport au fond moyenné avant compensation. La durée temporelle de l'impulsion focalisée est de 59 fs, ce qui est proche de la durée limitéepar transformée de Fourier de 54 fs.

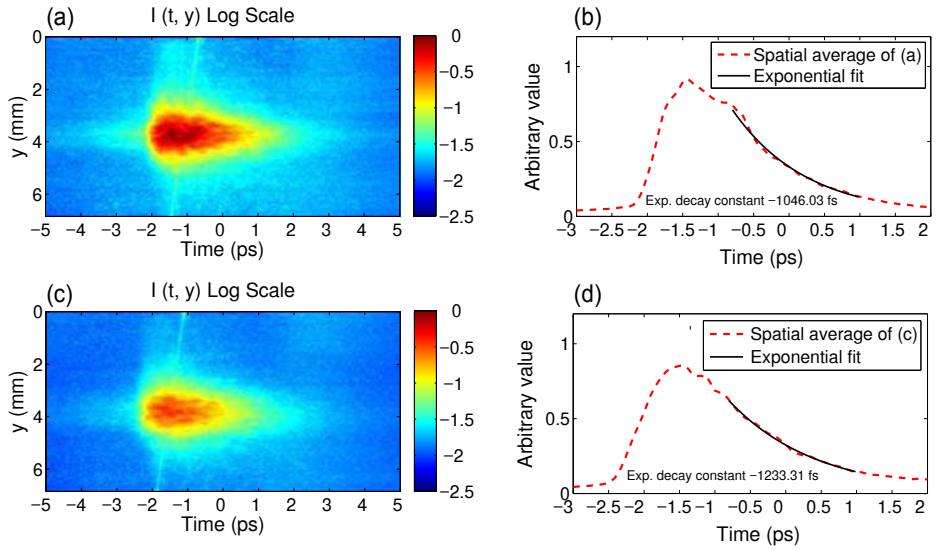

Figure A.4: *Intensité spatio-temporelle moyennée sur different position de l'échantillon. (a) Moyenne de l'intensité pour 41 positions de l'échantillon. (b) Intégration de l'intensité moyennée de Fig (a) sur la coordonnée spatiale. Le temps Thouless est extrait grâce à un fit exponentiel negatif et vaut 1046 fs.*

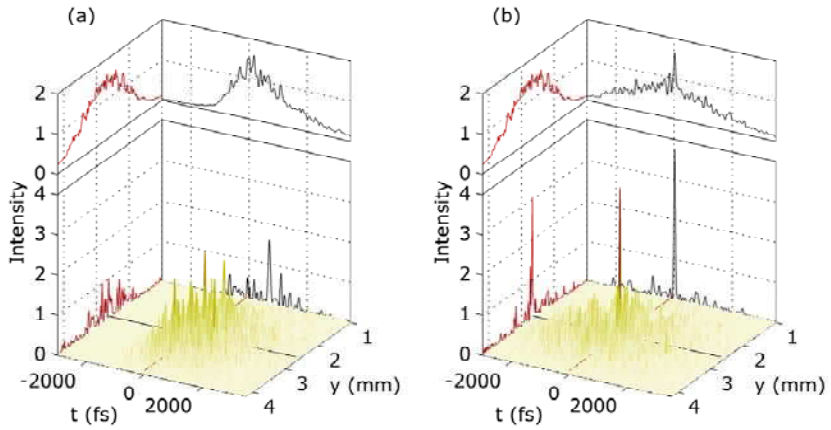

Figure A.5: *Focalisation spatio-temporelle. Intensité spatio-temporelle reconstruite $|E_{out}(t,y)|^2$ avant la compensation de la phase spectrale (a). La correction de la phase en un point choisi du motif à l'aide d'un façonneur d'impulsion conduit à une impulsion temporellement concentrée et spatialement localisée qui se dégage de l'arrière-plan du motif de speckle (b). L'intensité du pic temporel est améliorée d'un facteur 15 par rapport au fond moyenné avant compensation. La durée temporelle de l'impulsion focalisée est de 59 fs, ce qui est proche de la durée limitée par transformée de Fourier de 54 fs.*

A.4 Conclusion

Au cours des deux dernières décennies, différentes techniques de façonnages d'impulsions ont été développées, mais ces techniques souffrent de couplages spatio-temporels qui doivent être caractérisés afin de pouvoir utiliser toutes les potentialités des impulsions façonnées. Les limites des façonneurs d'impulsions basées sur le principe de la ligne à dispersion nulle ont été largement étudiés et documentés, mais ce n'est pas le cas des couplages induits par les filtres acousto-optiques programmables (AOPDF), une autre méthode de façonnage d'impulsion.

Au cours de ma thèse, j'ai étudié en détail et caractérisé le couplage spatio-temporel introduit par le façonneur d'impulsions UV-AOPDF à l'aide des techniques d'interférométrie spatio-spectrale par transformée de Fourier (FTSSI). FTSSI est une technique robuste d'interférométrie à référence qui révèle la fonction de transfert complète du façonneur d'impulsion. En utilisant ce dispositif, j'ai trouvé que les différentes formes d'impulsions façonnées, qui sont couramment utilisées dans des expériences de contrôle cohérents, sont parfaitement reproduites (cohérence parfaite entre les formes d'impulsion programmées et mesurées). Par ailleurs, j'ai constaté que toutes les impulsions façonnées souffrent d'un couplage spatio-temporel qui est un simple décalage spatial. Le mécanisme physique induisant ce couplage est la combinaison de walk-off biréfringent et géométriques. Nos résultats ont été les premiers à démontrer, quantifier et expliquer cet effet.

La seconde partie de ma thèse reprend l'utilisation de la technique FTSSI mais pour l'appliquer à la mesure d'impulsion façonnée naturellement par un échantillon multi-diffusant. En effet la traversée d'un milieu complexe induite le couplage des composantes spectrales et spatiales de manière complexe. J'ai démontré ainsi que par une mesure spatialement résolue de la phase spectrale de l'impulsion déformée suivie d'une correction en boucle ouverte à l'aide d'un façonneur d'impulsions, on pouvait focalisée temporellement et localisée spatialement une impulsion sortant d'un milieu complexe. Le processus de diffusion étant un processus linéaire, la correction par un façonneur passif a permis d'obtenir une phase spectrale plate pour un point de speckle donné donnant lieu à une impulsion courte à cet endroit de l'espace. En outre, en utilisant la technique FTSSI, j'ai caractérisé le speckle et pu extraire les propriétés de diffusion du milieu induisant ce speckle.
Une extension de mesure de 2D vers 3D, réalisable par balayage de la fente du spec-

tromètre, peut être considérée comme un outil puissant pour l'étude de l'ensemble de propriétés de speckle, telles que des vortex et des singularités. De plus, la capacité à récupérer des impulsions ultracourtes, en un point de speckle donné est un premier pas important pour la réalisation d'expérience de contrôle cohérent dans les milieux complexes comme par exemple au sein d'échantillons biologiques, et ce ci au-delà de la gamme des photons balistiques. Comme le milieu diffusant couple les modes spatiaux et spectraux de la lumière, une autre orientation possible serait d'étudier l'effet d'un tel milieu sur les photons intriqués ce ci permettrait de convertir une intrication spatiale en une intrication spectrale.
L'ensemble de ces voies semble très prometteuse à l'avenir et confirme que mes travaux de thèse apportent des outils qui pourront être utiles pour des travaux de recherche sur des milieux complexes ouvrant ainsi tout un champ de recherche.

Bibliography

[1] A. Zewail, Femtochemistry: ultrafast dynamics of the chemical bond, vol. 1 (World Scientific Pub Co Inc, 1994).

[2] H. Rabitz, R. de Vivie-Riedle, M. Motzkus, and K. Kompa, "Whither the future of controlling quantum phenomena?" Science **288**, 824–828 (2000).

[3] K. M. Evenson, J. S. Wells, F. R. Petersen, B. L. Danielson, G. W. Day, R. L. Barger, and J. L. Hall, "Speed of light from direct frequency and wavelength measurements of the methane-stabilized laser," Phys. Rev. Lett. **29**, 1346–1349 (1972).

[4] A. Brillet and J. L. Hall, "Improved laser test of the isotropy of space," Phys. Rev. Lett. **42**, 549–552 (1979).

[5] D. A. Jennings, C. R. Pollock, F. R. Petersen, R. E. Drullinger, K. M. Evenson, J. S. Wells, J. L. Hall, and H. P. Layer, "Direct frequency measurement of the I2-stabilized He-Ne 473-THz (633-nm) laser," Opt. Lett. **8**, 136–138 (1983).

[6] J. L. Hall and T. W. Hänsch, "External dye-laser frequency stabilizer," Opt. Lett. **9**, 502–504 (1984).

[7] D. J. Jones, S. A. Diddams, J. K. Ranka, A. Stentz, R. S. Windeler, J. L. Hall, and S. T. Cundiff, "Carrier-envelope phase control of femtosecond mode-locked lasers and direct optical frequency synthesis," Science **288**, 635–639 (2000).

[8] C. Iaconis and I. Walmsley, "Spectral phase interferometry for direct electric-field reconstruction of ultrashort optical pulses," Opt. Lett. **23**, 792–794 (1998).

[9] D. Kane and R. Trebino, "Characterization of arbitrary femtosecond pulses using frequency-resolved optical gating," Quantum Electronics, IEEE Journal of **29**, 571 –579 (1993).

[10] A. V. Smith, "Group-velocity-matched three-wave mixing in birefringent crystals," Opt. Lett. **26**, 719–721 (2001).

[11] T. Tanabe, H. Tanabe, Y. Teramura, and F. Kannari, "Spatiotemporal measurements based on spatial spectral interferometry for ultrashort optical pulses shaped by a fourier pulse shaper," J. Opt. Soc. Am. B **19**, 2795–2802 (2002).

[12] M. Dantus and V. V. Lozovoy, "Experimental coherent laser control of physicochemical processes," Chemical Reviews **104**, 1813–1860 (2004). PMID: 15080713.

[13] D. Goswami, "Optical pulse shaping approaches to coherent control," Physics Reports **374**, 385 – 481 (2003).

[14] K. Ohmori, "Wave-packet and coherent control dynamics," Annual Review of Physical Chemistry **60**, 487–511 (2009). PMID: 19335221.

[15] Y. Silberberg, "Quantum coherent control for nonlinear spectroscopy and microscopy," Annual Review of Physical Chemistry **60**, 277–292 (2009). PMID: 18999997.

[16] Z. Jiang, S. Yang, D. Leaird, and A. Weiner, "Fully dispersion-compensated 500 fs pulse transmission over 50 km single-mode fiber," Optics letters **30**, 1449–1451 (2005).

[17] S.-H. Shim and M. T. Zanni, "How to turn your pump-probe instrument into a multidimensional spectrometer: 2D IR and Vis spectroscopies via pulse shaping," Phys. Chem. Chem. Phys. **11**, 748–761 (2009).

[18] H. Sardesai, C. Chang, and A. Weiner, "A femtosecond code-division multiple-access communication system test bed," Lightwave Technology, Journal of **16**, 1953–1964 (1998).

[19] D. Bigourd, B. Chatel, W. P. Schleich, and B. Girard, "Factorization of numbers with the temporal talbot effect: Optical implementation by a sequence of shaped ultrashort pulses," Phys. Rev. Lett. **100**, 030202 (2008).

[20] S. Weber, B. Chatel, and B. Girard, "Factoring numbers with interfering random waves," EPL (Europhysics Letters) **83**, 34008 (2008).

[21] S. Woelk, W. Merkel, W. Schleich, I. Averbukh, and B. Girard, "Factorization of numbers with gauss sums: I. mathematical background," New Journal of Physics **13**, 103007 (2011).

[22] M. Danailov and I. Christov, "Time-space shaping of light pulses by fourier optical processing," Journal of Modern Optics **36**, 725–731 (1989).

[23] M. M. Wefers and K. A. Nelson, "Analysis of programmable ultrashort waveform generation using liquid-crystal spatial light modulators," J. Opt. Soc. Am. B **12**, 1343–1362 (1995).

[24] M. Wefers and K. Nelson, "Space-time profiles of shaped ultrafast optical waveforms," Quantum Electronics, IEEE Journal of **32**, 161 –172 (1996).

[25] C. Dorrer and F. Salin, "Phase amplitude coupling in spectral phase modulation," Selected Topics in Quantum Electronics, IEEE Journal of **4**, 342 –345 (1998).

[26] D. Brinks, R. Hildner, F. D. Stefani, and N. F. van Hulst, "Beating spatio-temporal coupling: implications for pulse shaping and coherent control experiments," Opt. Express **19**, 26486–26499 (2011).

[27] D. Huang, E. Swanson, C. Lin, J. Schuman, W. Stinson, W. Chang, M. Hee, T. Flotte, K. Gregory, C. Puliafito et al., "Optical coherence tomography," Science **254**, 1178–1181 (1991).

[28] F. Helmchen and W. Denk, "Deep tissue two-photon microscopy," Nature methods **2**, 932–940 (2005).

[29] I. M. Vellekoop and A. P. Mosk, "Focusing coherent light through opaque strongly scattering media," Opt. Lett. **32**, 2309–2311 (2007).

[30] A. Derode, P. Roux, and M. Fink, "Robust acoustic time reversal with high-order multiple scattering," Phys. Rev. Lett. **75**, 4206–4209 (1995).

[31] M. Fink, "Time reversed acoustics," Physics Today **50**, 34 (1997).

[32] G. Lerosey, J. de Rosny, A. Tourin, A. Derode, G. Montaldo, and M. Fink, "Time reversal of electromagnetic waves," Phys. Rev. Lett. **92**, 193904 (2004).

[33] G. Lerosey, J. de Rosny, A. Tourin, A. Derode, and M. Fink, "Time reversal of wideband microwaves," Applied Physics Letters **88**, 154101 (2006).

[34] A. Tajalli, D. J. McCabe, D. R. Austin, I. A. Walmsley, and B. Chatel, "Characterization of the femtosecond speckle field of a multiply scattering medium via spatio-spectral interferometry," J. Opt. Soc. Am. B **29**, 1146–1151 (2012).

[35] D. J. McCabe, A. Tajalli, D. R. Austin, P. Bondareff, I. A. Walmsley, S. Gigan, and B. Chatel, "Spatio-temporal focusing of an ultrafast pulse through a multiply scattering medium," Nature. Commun. **2**, 447 (2011).

[36] S. Backus, C. Durfee III, M. Murnane, and H. Kapteyn, "High power ultrafast lasers," Review of scientific instruments **69**, 1207 (1998).

[37] D. Strickland and G. Mourou, "Compression of amplified chirped optical pulses," Optics Communications **56**, 219 – 221 (1985).

[38] O. Martinez, "Design of high-power ultrashort pulse amplifiers by expansion and recompression," Quantum Electronics, IEEE Journal of **23**, 1385 – 1387 (1987).

[39] O. Martinez, "3000 times grating compressor with positive group velocity dispersion: Application to fiber compensation in 1.3-1.6 μm region," Quantum Electronics, IEEE Journal of pp. 59 – 64 (1987).

[40] Pierre and Tournois, "Acousto-optic programmable dispersive filter for adaptive compensation of group delay time dispersion in laser systems," Optics Communications **140**, 245 – 249 (1997).

[41] K. Wynne, G. D. Reid, and R. M. Hochstrasser, "Regenerative amplification of 30-fs pulses in Ti:sapphire at 5 kHz," Opt. Lett. **19**, 895–897 (1994).

[42] C. L. Blanc, G. Grillon, J. P. Chambaret, A. Migus, and A. Antonetti, "Compact and efficient multipass Ti:sapphire system for femtosecond chirped-pulse amplification at the terawatt level," Opt. Lett. **18**, 140–142 (1993).

[43] E. Treacy, "Optical pulse compression with diffraction gratings," Quantum Electronics, IEEE Journal of **5**, 454 – 458 (1969).

[44] V. Blanchet, "Femtosecond spectroscopy and coherent control in alkalines," Ph.D. thesis, Université Paul Sabatier, Toulouse (1996).

[45] Y. Nabekawa, K. Kondo, N. Sarukura, K. Sajiki, and S. Watanabe, "Terawatt KrF/Ti:sapphire hybrid laser system," Opt. Lett. **18**, 1922–1924 (1993).

[46] J. Ringling, O. Kittelmann, F. Noack, G. Korn, and J. Squier, "Tunable femtosecond pulses in the near vacuum ultraviolet generated by frequency conversion of amplified Ti:sapphire laser pulses," Opt. Lett. **18**, 2035–2037 (1993).

[47] S. Backus, J. Peatross, Z. Zeek, A. Rundquist, G. Taft, M. M. Murnane, and H. C. Kapteyn, "16-fs, 1- μJ ultraviolet pulses generated by third-harmonic conversion in air," Opt. Lett. **21**, 665–667 (1996).

[48] C. G. Durfee III, S. Backus, H. C. Kapteyn, and M. M. Murnane, "Intense 8-fs pulse generation in the deep ultraviolet," Opt. Lett. **24**, 697–699 (1999).

[49] T. Fuji, T. Horio, and T. Suzuki, "Generation of 12 fs deep-ultraviolet pulses by four-wave mixing through filamentation in neon gas," Opt. Lett. **32**, 2481–2483 (2007).

[50] U. Graf, M. Fieß, M. Schultze, R. Kienberger, F. Krausz, and E. Goulielmakis, "Intense few-cycle light pulses in the deep ultraviolet," Opt. Express **16**, 18956–18963 (2008).

[51] F. Reiter, U. Graf, M. Schultze, W. Schweinberger, H. Schröder, N. Karpowicz, A. M. Azzeer, R. Kienberger, F. Krausz, and E. Goulielmakis, "Generation of sub-3 fs pulses in the deep ultraviolet," Opt. Lett. **35**, 2248–2250 (2010).

[52] T. Nagy and P. Simon, "Generation of 200-μJ, sub-25-fs deep-UV pulses using a noble-gas-filled hollow fiber," Opt. Lett. **34**, 2300–2302 (2009).

[53] M. Ghotbi, P. Trabs, and M. Beutler, "Generation of high-energy, sub-20-fs pulses in the deep ultraviolet by using spectral broadening during filamentation in argon," Opt. Lett. **36**, 463–465 (2011).

[54] P. Baum, S. Lochbrunner, and E. Riedle, "Tunable sub-10-fs ultraviolet pulses generated by achromatic frequency doubling," Opt. Lett. **29**, 1686–1688 (2004).

[55] A. E. Jailaubekov and S. E. Bradforth, "Tunable 30-femtosecond pulses across the deep ultraviolet," Applied Physics Letters **87**, 021107 (2005).

[56] S. A. Trushin, K. Kosma, W. Fuß, and W. E. Schmid, "Sub-10-fs supercontinuum radiation generated by filamentation of few-cycle 800 nm pulses in argon," Opt. Lett. **32**, 2432–2434 (2007).

[57] A. M. Weiner, "Femtosecond pulse shaping using spatial light modulators," Review of Scientific Instruments **71**, 1929–1960 (2000).

[58] A. Monmayrant, S. Weber, and B. Chatel, "A newcomer's guide to ultrashort pulse shaping and characterization," J. Phys. B **43**, 103001 (2010).

[59] A. Monmayrant and B. Chatel, "New phase and amplitude high resolution pulse shaper," Review of Scientific Instruments **75**, 2668–2671 (2004).

[60] S. Coudreau, D. Kaplan, and P. Tournois, "Ultraviolet acousto-optic programmable dispersive filter laser pulse shaping in KDP," Opt. Lett. **31**, 1899–1901 (2006).

[61] D. J. McCabe, D. R. Austin, A. Tajalli, S. Weber, I. A. Walmsley, and B. Chatel, "Space–time coupling of shaped ultrafast ultraviolet pulses from an acousto-optic programmable dispersive filter," J. Opt. Soc. Am. B **28**, 58–64 (2011).

[62] C. Froehly, B. Colombeau, and M. Vampouille, "II Shaping and Analysis of Picosecond Light Pulses," (Elsevier, 1983), pp. 63 – 153.

[63] A. M. Weiner, J. P. Heritage, and E. M. Kirschner, "High-resolution femtosecond pulse shaping," J. Opt. Soc. Am. B **5**, 1563–1572 (1988).

[64] T. Brixner and G. Gerber, "Femtosecond polarization pulse shaping," Opt. Lett. **26**, 557–559 (2001).

[65] A. Monmayrant, "Façonnage et caractérisation d'impulsions ultracourtes. Contrôle cohérent de systèmes simples." Ph.D. thesis, Université Paul Sabatier (2005).

[66] B. J. Sussman, R. Lausten, and A. Stolow, "Focusing of light following a 4-f pulse shaper: Considerations for quantum control," Phys. Rev. A **77**, 043416 (2008).

[67] F. Frei, A. Galler, and T. Feurer, "Space-time coupling in femtosecond pulse shaping and its effects on coherent control," The Journal of Chemical Physics **130**, 034302 (2009).

[68] R. Szipöcs, K. Ferencz, C. Spielmann, and F. Krausz, "Chirped multilayer coatings for broadband dispersion control in femtosecond lasers," Opt. Lett. **19**, 201–203 (1994).

[69] F. Verluise, V. Laude, J.-P. Huignard, P. Tournois, and A. Migus, "Arbitrary dispersion control of ultrashort optical pulses with acoustic waves," J. Opt. Soc. Am. B **17**, 138–145 (2000).

[70] D. Kaplan and P. Tournois, "Theory and performance of the acousto optic programmable dispersive filter used for femtosecond laser pulse shaping," J. Phys. IV France **12**, 69–75 (2002).

[71] P. Tournois, "Design of acousto-optic programmable filters in mercury halides for mid-infrared laser pulse shaping," Optics Communications **281**, 4054 – 4056 (2008).

[72] V. Voloshinov and N. Gupta, "Ultraviolet-Visible Imaging Acousto-Optic Tunable Filters in KDP," Appl. Opt. **43**, 3901–3909 (2004).

[73] S. Weber, "Façonnage d'impulsions femtosecondes dans l'ultraviolet. Factorisation de grands nombres. Contrôle cohérent de systèmes atomiques et moléculaires." Ph.D. thesis, Université Paul Sabatier, Toulouse (2010).

[74] S. Weber, M. Barthélemy, and B. Chatel, "Direct shaping of tunable UV ultra-short pulses," Applied Physics B: Lasers and Optics **98**, 323–326 (2010).

[75] I. A. Walmsley and C. Dorrer, "Characterization of ultrashort electromagnetic pulses," Adv. Opt. Photon. **1**, 308–437 (2009).

[76] J. A. Armstrong, "Measurement of picosecond laser pulse widths," Applied Physics Letters **10**, 16–18 (1967).

[77] K. Sala, G. Kenney-Wallace, and G. Hall, "CW autocorrelation measurements of picosecond laser pulses," Quantum Electronics, IEEE Journal of **16**, 990 – 996 (1980).

[78] J. C. M. Diels, J. J. Fontaine, I. C. McMichael, and F. Simoni, "Control and measurement of ultrashort pulse shapes (in amplitude and phase) with femtosecond accuracy," Appl. Opt. **24**, 1270–1282 (1985).

[79] C. Ventalon, J. Fraser, J. Likforman, D. Villeneuve, P. Corkum, and M. Joffre, "Generation and complete characterization of intense mid-infrared ultrashort pulses," JOSA B **23**, 332–340 (2006).

[80] K. Naganuma, K. Mogi, and H. Yamada, "General method for ultrashort light pulse chirp measurement," Quantum Electronics, IEEE Journal of **25**, 1225–1233 (1989).

[81] J. Chung and A. Weiner, "Ambiguity of ultrashort pulse shapes retrieved from the intensity autocorrelation and the power spectrum," Selected Topics in Quantum Electronics, IEEE Journal of **7**, 656–666 (2001).

[82] E. B. Treacy, "Measurement of picosecond pulse substructure using compression techniques," Applied Physics Letters **14**, 112–114 (1969).

[83] C. Froehly, A. Lacourt, and J. C. Viénot, "Time impulse response and time frequency response of optical pupils. Experimental confirmations and applications," Nouvelle Revue d'Optique **4**, 183 (1973).

[84] L. Lepetit, G. Chériaux, and M. Joffre, "Linear techniques of phase measurement by femtosecond spectral interferometry for applications in spectroscopy," J. Opt. Soc. Am. B **12**, 2467–2474 (1995).

[85] F. Reynaud, F. Salin, and A. Barthelemy, "Measurement of phase shifts introduced by nonlinear optical phenomena on subpicosecond pulses," Opt. Lett. **14**, 275–277 (1989).

[86] M. Takeda, H. Ina, and S. Kobayashi, "Fourier-transform method of fringe-pattern analysis for computer-based topography and interferometry," J. Opt. Soc. Am. **72**, 156–160 (1982).

[87] C. Dorrer and M. Joffre, "Characterization of the spectral phase of ultrashort light pulses," Comptes Rendus de l'Académie des Sciences-Series IV-Physics **2**, 1415–1426 (2001).

[88] K. Naganuma and Y. Sakai, "Interferometric measurement of wavelength dispersion on femtosecond laser cavities," Opt. Lett. **19**, 487–489 (1994).

[89] V. Wong and I. A. Walmsley, "Linear filter analysis of methods for ultrashort-pulse-shape measurements," J. Opt. Soc. Am. B **12**, 1491–1499 (1995).

[90] R. Trebino, Frequency-resolved optical gating: the measurement of ultrashort laser pulses, vol. 1 (Springer, 2000).

[91] D. Kane, "Recent progress toward real-time measurement of ultrashort laser pulses," Quantum Electronics, IEEE Journal of **35**, 421 –431 (1999).

[92] D. Kane, "Real-time measurement of ultrashort laser pulses using principal component generalized projections," Selected Topics in Quantum Electronics, IEEE Journal of **4**, 278 –284 (1998).

[93] W. Bates, "A wavefront shearing interferometer," Proceedings of the Physical Society **59**, 940–950 (1947).

[94] M. Murty., "The use of a single plane parallel plate as a lateral shearing interferometer with a visible gas laser source," Appl. Opt **3**, 531 (1964).

[95] S. P. Gorza, A. S. Radunsky, P. Wasylczyk, and I. A. Walmsley, "Tailoring the phase-matching function for ultrashort pulse characterization by spectral shearing interferometry," J. Opt. Soc. Am. B **24**, 2064–2074 (2007).

[96] A. S. Radunsky, I. A. Walmsley, S. P. Gorza, and P. Wasylczyk, "Compact spectral shearing interferometer for ultrashort pulse characterization," Opt. Lett. **32**, 181–183 (2007).

[97] J. Seres, A. Müller, E. Seres, K. O'Keeffe, M. Lenner, R. F. Herzog, D. Kaplan, C. Spielmann, and F. Krausz, "Sub-10-fs, terawatt-scale Ti:sapphire laser system," Opt. Lett. **28**, 1832–1834 (2003).

[98] N. T. Form, R. Burbidge, J. Ramon, and B. J. Whitaker, "Parameterization of an acousto-optic programmable dispersive filter for closed-loop learning experiments," Journal of Modern Optics **55**, 197–209 (2008).

[99] A. Börzsönyi, M. Mero, A. P. Kovács, M. P. Kalashnikov, and K. Osvay, "Measurement Of The Spectral Phase Shift And The Residual Angular Dispersion Of An AOPDF," AIP Conference Proceedings **1228**, 138–143 (2010).

[100] N. Krebs, R. A. Probst, and E. Riedle, "Sub-20 fs pulses shaped directly in the UV by an acousto-optic programmable dispersive filter," Opt. Express **18**, 6164–6171 (2010).

[101] K. Osvay, M. Mero, A. Börzsönyi, A. Kovács, and M. Kalashnikov, "Spectral phase shift and residual angular dispersion of an acousto-optic programmable dispersive filter," Applied Physics B: Lasers and Optics **107**, 1–6 (2011).

[102] R. L. Fork, O. E. Martinez, and J. P. Gordon, "Negative dispersion using pairs of prisms," Opt. Lett. **9**, 150–152 (1984).

[103] O. E. Martinez, J. P. Gordon, and R. L. Fork, "Negative group-velocity dispersion using refraction," J. Opt. Soc. Am. A **1**, 1003–1006 (1984).

[104] J. P. Gordon and R. L. Fork, "Optical resonator with negative dispersion," Opt. Lett. **9**, 153–155 (1984).

[105] X. Gu, S. Akturk, and R. Trebino, "Spatial chirp in ultrafast optics," Optics Communications **242**, 599 – 604 (2004).

[106] S. Akturk, X. Gu, P. Bowlan, and R. Trebino, "Spatio-temporal couplings in ultrashort laser pulses," Journal of Optics **12**, 093001 (2010).

[107] S. Akturk, X. Gu, P. Gabolde, and R. Trebino, "The general theory of first-order spatio-temporal distortions of gaussian pulses and beams," Opt. Express **13**, 8642–8661 (2005).

[108] P. Gabolde, D. Lee, S. Akturk, and R. Trebino, "Describing first-order spatio-temporal distortions in ultrashort pulses using normalized parameters," Opt. Express **15**, 242–251 (2007).

[109] S. Akturk, X. Gu, E. Zeek, and R. Trebino, "Pulse-front tilt caused by spatial and temporal chirp," Opt. Express **12**, 4399–4410 (2004).

[110] Z. Bor, Z. Gogolak, and G. Szabo, "Femtosecond-resolution pulse-front distortion measurement by time-of-flight interferometry," Opt. Lett. **14**, 862–864 (1989).

[111] Z. Bor, "Distortion of femtosecond laser pulses in lenses and lens systems," Journal of Modern Optics **35**, 1907–1918 (1988).

[112] Z. Bor and Z. Horváth, "Distortion of femtosecond pulses in lenses. wave optical description," Optics Communications **94**, 249 – 258 (1992).

[113] Z. Horváth and Z. Bor, "Focusing of femtosecond pulses having gaussian spatial distribution," Optics Communications **100**, 6 – 12 (1993).

[114] M. Kempe and W. Rudolph, "Femtosecond pulses in the focal region of lenses," Phys. Rev. A **48**, 4721–4729 (1993).

[115] A. Federico and O. Martinez, "Distortion of femtosecond pulses due to chromatic aberration in lenses," Optics Communications **91**, 104 – 110 (1992).

[116] M. Kempe, U. Stamm, B. Wilhelmi, and W. Rudolph, "Spatial and temporal transformation of femtosecond laser pulses by lenses and lens systems," J. Opt. Soc. Am. B **9**, 1158–1165 (1992).

[117] B. Platt, "History and principles of Shack-Hartmann wavefront sensing," J. Refractive Surg **17**, 573–577 (2001).

[118] J. Hartmann, "Bemerkungen uber den bau und die justirung von spektrographen," Z Instrumentenkd **20**, 47 (1900).

[119] C. P. Hauri, J. Biegert, U. Keller, B. Schaefer, K. Mann, and G. Marowski, "Validity of wavefront reconstruction and propagation of ultrabroadband pulses measured with a Hartmann-Shack sensor," Opt. Lett. **30**, 1563–1565 (2005).

[120] E. Rubino, D. Faccio, L. Tartara, P. K. Bates, O. Chalus, M. Clerici, F. Bonaretti, J. Biegert, and P. D. Trapani, "Spatiotemporal amplitude and phase retrieval of space-time coupled ultrashort pulses using the Shackled-FROG technique," Opt. Lett. **34**, 3854–3856 (2009).

[121] D. Dutton, A. Cornejo, and M. Latta, "A semiautomatic method for interpreting shearing interferograms," Appl. Opt. **7**, 125–131 (1968).

[122] R. N. Smartt and W. H. Steel, "Theory and application of point-diffraction interferometers," Japanese Journal of Applied Physics **14S1**, 351–356 (1975).

[123] G. Pretzler, A. Kasper, and K. Witte, "Angular chirp and tilted light pulses in CPA lasers," Applied Physics B: Lasers and Optics **70**, 1–9 (2000).

[124] P. Gabolde and R. Trebino, "Self-referenced measurement of the complete electric field of ultrashort pulses," Opt. Express **12**, 4423–4429 (2004).

[125] G. Paez, M. Strojnik, and G. G. Torales, "Vectorial shearing interferometer," Appl. Opt. **39**, 5172–5178 (2000).

[126] P. Hariharan and D. Sen, "Radial shearing interferometer," Journal of Scientific Instruments **38**, 428 (1961).

[127] C. Dorrer and I. A. Walmsley, "Simple linear technique for the measurement of space-time coupling in ultrashort optical pulses," Opt. Lett. **27**, 1947–1949 (2002).

[128] C. Dorrer, E. M. Kosik, and I. A. Walmsley, "Direct space time-characterization of the electric fields of ultrashort optical pulses," Opt. Lett. **27**, 548–550 (2002).

[129] C. Dorrer, E. Kosik, and I. Walmsley, "Spatio-temporal characterization of the electric field of ultrashort optical pulses using two-dimensional shearing interferometry," Applied Physics B: Lasers and Optics **74**, 209–217 (2002).

[130] Z. Sacks, G. Mourou, and R. Danielius, "Adjusting pulse-front tilt and pulse duration by use of a single-shot autocorrelator," Opt. Lett. **26**, 462–464 (2001).

[131] M. Raghuramaiah, A. Sharma, P. Naik, and P. Gupta, "Simultaneous measurement of pulse-front tilt and pulse duration of a femtosecond laser beam," Optics Communications **223**, 163 – 168 (2003).

[132] D. J. Kane and R. Trebino, "Single-shot measurement of the intensity and phase of an arbitrary ultrashort pulse by using frequency-resolved optical gating," Opt. Lett. **18**, 823–825 (1993).

[133] S. Akturk, M. Kimmel, P. O'Shea, and R. Trebino, "Measuring spatial chirp in ultrashort pulses using single-shot frequency-resolved optical gating," Opt. Express **11**, 68–78 (2003).

[134] P. O'Shea, M. Kimmel, X. Gu, and R. Trebino, "Highly simplified device for ultrashort-pulse measurement," Opt. Lett. **26**, 932–934 (2001).

[135] S. Akturk, M. Kimmel, P. O'Shea, and R. Trebino, "Measuring pulse-front tilt in ultrashort pulses using GRENOUILLE," Opt. Express **11**, 491–501 (2003).

[136] J. Jasapara and W. Rudolph, "Characterization of sub-10-fs pulse focusing with high-numerical-aperture microscope objectives," Opt. Lett. **24**, 777–779 (1999).

[137] W. AMIR, C. G. DURFEE, D. N. SCHAFER, E. A. GIBSON, L. KOST, E. PRZEKWAS, R. JIMENEZ, and J. A. SQUIER, "Linear spatio-temporal characterization of a UV microscope objective for nonlinear imaging and spectroscopy by using two-dimensional spectral interferometry," Journal of Microscopy **230**, 4–8 (2008).

[138] T. A. Planchon, W. Amir, C. Childress, J. A. Squier, and C. G. Durfee, "Measurement of pump-induced transient lensing in a cryogenically-cooled high average power Ti:sapphire amplifier," Opt. Express **16**, 18557–18564 (2008).

[139] P. Bowlan, P. Gabolde, and R. Trebino, "Directly measuring the spatio-temporal electric field of focusing ultrashort pulses," Opt. Express **15**, 10219–10230 (2007).

[140] P. Bowlan, P. Gabolde, M. A. Coughlan, R. Trebino, and R. J. Levis, "Measuring the spatiotemporal electric field of ultrashort pulses with high spatial and spectral resolution," J. Opt. Soc. Am. B **25**, 81–92 (2008).

[141] E. M. Kosik, A. S. Radunsky, I. A. Walmsley, and C. Dorrer, "Interferometric technique for measuring broadband ultrashort pulses at the sampling limit," Opt. Lett. **30**, 326–328 (2005).

[142] P. Gabolde and R. Trebino, "Single-shot measurement of the full spatio-temporal field of ultrashort pulses with multi-spectral digital holography," Opt. Express **14**, 11460–11467 (2006).

[143] P. Gabolde and R. Trebino, "Single-frame measurement of the complete spatiotemporal intensity and phase of ultrashort laser pulses using wavelength-multiplexed digital holography," J. Opt. Soc. Am. B **25**, 25–33 (2008).

[144] A. B. Shafer, "Correcting for Astigmatism in the Czerny-Turner Spectrometer and Spectrograph," Appl. Opt. **6**, 159–160 (1967).

[145] J. Murphy L. Dalton, "Astigmatism Compensation in the Czerny-Turner Spectrometer," Appl. Opt. **5**, 1121–1123 (1966).

[146] D. R. Austin, T. Witting, and I. A. Walmsley, "Broadband astigmatism-free Czerny-Turner imaging spectrometer using spherical mirrors," Appl. Opt. **48**, 3846–3853 (2009).

[147] D. R. Austin, T. Witting, and I. A. Walmsley, "High precision self-referenced phase retrieval of complex pulses with multiple-shearing spectral interferometry," J. Opt. Soc. Am. B **26**, 1818–1830 (2009).

[148] A. Assion, T. Baumert, M. Bergt, T. Brixner, B. Kiefer, V. Seyfried, M. Strehle, and G. Gerber, "Control of chemical reactions by feedback-optimized phase-shaped femtosecond laser pulses," Science **282**, 919–922 (1998).

[149] W. S. Warren, H. Rabitz, and M. Dahleh, "Coherent control of quantum dynamics: The dream is alive," Science **259**, 1581–1589 (1993).

[150] N. Dudovich, D. Oron, and Y. Silberberg, "Coherent transient enhancement of optically induced resonant transitions," Phys. Rev. Lett. **88**, 123004 (2002).

[151] J. Degert, W. Wohlleben, B. Chatel, M. Motzkus, and B. Girard, "Realization of a Time-Domain Fresnel Lens with Coherent Control," Phys. Rev. Lett. **89**, 203003 (2002).

[152] A. H. Zewail, "Femtochemistry:Atomic-Scale Dynamics of the Chemical Bond," The Journal of Physical Chemistry A **104**, 5660–5694 (2000).

[153] W. Zipfel, R. Williams, and W. Webb, "Nonlinear magic: multiphoton microscopy in the biosciences," Nature biotechnology **21**, 1369–1377 (2003).

[154] K. M. Yoo and R. R. Alfano, "Time-resolved coherent and incoherent components of forward light-scattering in random-media," Opt. Lett. **15**, 320–322 (1990).

[155] L. Feng, K. M. Yoo, and R. R. Alfano, "Transmitted photon intensity through biological tissues within various time windows," Opt. Lett. **19**, 740–742 (1994).

[156] J. W. Goodman, "Some fundamental properties of speckle," J. Opt. Soc. Am. **66**, 1145–1150 (1976).

[157] S. Farsiu, J. Christofferson, B. Eriksson, P. Milanfar, B. Friedlander, A. Shakouri, and R. Nowak, "Statistical detection and imaging of objects hidden in turbid media using ballistic photons," Appl. Opt. **46**, 5805–5822 (2007).

[158] J. M. Schmitt, A. H. Gandjbakhche, and R. F. Bonner, "Use of polarized-light to discriminate short-path photons in a multiply scattering medium," Appl. Opt. **31**, 6535–6546 (1992).

[159] O. Emile, F. Bretenaker, and A. LeFloch, "Rotating polarization imaging in turbid media," Opt. Lett. **21**, 1706–1708 (1996).

[160] H. Ramachandran and A. Narayanan, "Two-dimensional imaging through turbid media using a continuous wave light source," Opt. Commun. **154**, 255–260 (1998).

[161] H. Ramachandran and S. Mujumdar, "Imaging through turbid media using polarization modulation: dependence on scattering anisotropy," Opt. Commun. **241**, 1–9 (2004).

[162] D. S. Dilworth, E. N. Leith, and J. L. Lopez, "3-dimensional confocal imaging of objects embedded within thick diffusing media," Appl. Opt. **30**, 1796–1803 (1991).

[163] M. S. Patterson, J. D. Moulton, B. C. Wilson, K. W. Berndt, and J. R. Lakowicz, "Frequency-domain reflectance for the determination of the scattering and absorption properties of tissue," Appl. Opt. **30**, 4474–4476 (1991).

[164] L. Wang, P. P. Ho, C. Liu, G. Zhang, and R. R. Alfano, "Ballistic 2-D Imaging through Scattering Walls Using an Ultrafast Optical Kerr Gate," Science **253**, 769–771 (1991).

[165] I. M. Vellekoop and A. P. Mosk, "Universal optimal transmission of light through disordered materials," Phys. Rev. Lett. **101**, 120601 (2008).

[166] I. Vellekoop, A. Lagendijk, and A. Mosk, "Exploiting disorder for perfect focusing," Nature Photonics **4**, 320–322 (2010).

[167] I. M. Vellekoop and C. M. Aegerter, "Scattered light fluorescence microscopy: imaging through turbid layers," Opt. Lett. **35**, 1245–1247 (2010).

[168] S. Popoff, G. Lerosey, M. Fink, A. Boccara, and S. Gigan, "Image transmission through an opaque material," Nature Communications **1**, 81 (2010).

[169] S. M. Popoff, G. Lerosey, R. Carminati, M. Fink, A. C. Boccara, and S. Gigan, "Measuring the transmission matrix in optics: An approach to the study and control of light propagation in disordered media," Phys. Rev. Lett. **104**, 100601 (2010).

[170] S. M. Popoff, G. Lerosey, M. Fink, A. C. Boccara, and S. Gigan, "Controlling light through optical disordered media: transmission matrix approach," New Journal of Physics **13**, 123021 (2011).

[171] T. Čižmàr, M. Mazilu, and K. Dholakia, "In situ wavefront correction and its application to micromanipulation," Nature Photonics **4**, 388–394 (2010).

[172] Z. Yaqoob, D. Psaltis, M. S. Feld, and C. H. Yang, "Optical phase conjugation for turbidity suppression in biological samples," Nature. Photon. **2**, 110–115 (2008).

[173] M. Tomita and T. Matsumoto, "Observation and formulation of 2-dimensional speckle in the space and the time domains," J. Opt. Soc. Am. B **12**, 170–174 (1995).

[174] W. J. Liu, R. X. Gao, and S. L. Qu, "Measurements of femtosecond temporal speckle field of a random medium," Chinese. Phys. B **19**, 024204 (2010).

[175] G. Lerosey, J. de Rosny, A. Tourin, and M. Fink, "Focusing beyond the diffraction limit with far-field time reversal," Science **315**, 1120–1122 (2007).

[176] A. Derode, A. Tourin, J. de Rosny, M. Tanter, S. Yon, and M. Fink, "Taking advantage of multiple scattering to communicate with time-reversal antennas," Phys. Rev. Lett. **90**, 014301 (2003).

[177] O. Katz, E. Small, Y. Bromberg, and Y. Silberberg, "Focusing and compression of ultrashort pulses through scattering media," Nature. Photon. **5**, 372–377 (2011).

[178] J. Aulbach, B. Gjonaj, P. M. Johnson, A. P. Mosk, and A. Lagendijk, "Control of light transmission through opaque scattering media in space and time," Phys. Rev. Lett. **106**, 103901 (2011).

[179] N. Curry, P. Bondareff, M. Leclercq, N. F. van Hulst, R. Sapienza, S. Gigan, and S. Grésillon, "Direct determination of diffusion properties of random media from speckle contrast," Opt. Lett. **36**, 3332–3334 (2011).

[180] P. E. Wolf, G. Maret, E. Akkermans, and R. Maynard, "Optical Coherent Backscattering by Random-Media- an Experimental-Study," J. Phys. (Paris) **49**, 63–75 (1988).

[181] A. Z. Genack, "Optical-transmission in disordered media," Phys. Rev. Lett. **58**, 2043–2046 (1987).

[182] D. S. Wiersma, A. Muzzi, M. Colocci, and R. Righini, "Time-resolved experiments on light diffusion in anisotropic random media," Phys. Rev. E **62**, 6681–6687 (2000).

[183] W. Cai, B. B. Das, F. Liu, M. Zevallos, M. Lax, and R. R. Alfano, "Time-resolved optical diffusion tomographic image reconstruction in highly scattering turbid media," Proc. Natl. Acad. Sci. U. S. A. **93**, 13561–13564 (1996).

[184] I. M. Vellekoop, P. Lodahl, and A. Lagendijk, "Determination of the diffusion constant using phase-sensitive measurements," Phys. Rev. E **71**, 056604 (2005).

[185] S. Faez, P. M. Johnson, and A. Lagendijk, "Varying the effective refractive index to measure optical transport in random media," Phys. Rev. Lett. **103**, 53903 (2009).

[186] M. P. Vanalbada, B. A. Vantiggelen, A. Lagendijk, and A. Tip, "Speed of propagation of classical waves in strongly scattering media," Phys. Rev. Lett. **66**, 3132–3135 (1991).

[187] R. Sapienza, P. D. Garcia, J. Bertolotti, M. D. Martin, A. Blanco, L. Vina, C. Lopez, and D. S. Wiersma, "Observation of resonant behavior in the energy velocity of diffused light," Phys. Rev. Lett. **99**, 233902 (2007).

[188] C. A. Thompson, K. J. Webb, and A. M. Weiner, "Diffusive media characterization with laser speckle," Appl. Opt. **36**, 3726–3734 (1997).

[189] J. D. McKinney, M. A. Webster, K. J. Webb, and A. M. Weiner, "Characterization and imaging in optically scattering media by use of laser speckle and a variable-coherence source," Opt. Lett. **25**, 4–6 (2000).

[190] J. Goodman, Speckle phenomena in optics: theory and applications (Roberts & Co, 2007).

[191] A. P. Gibson, J. C. Hebden, and S. R. Arridge, "Recent advances in diffuse optical imaging," Physics in Medicine and Biology **50**, R1 (2005).

[192] L. Kennedy, L. Bickford, N. Lewinski, A. Coughlin, Y. Hu, E. Day, J. West, and R. Drezek, "A new era for cancer treatment: Gold-nanoparticle-mediated thermal therapies," Small **7**, 169–183 (2011).

[193] W. B. Bridges, P. T. Brunner, S. P. Lazzara, T. A. Nussmeier, T. R. O'Meara, J. A. Sanguinet, and J. W. P. Brown, "Coherent optical adaptive techniques," Appl. Opt. **13**, 291–300 (1974).

[194] M. Rueckel, J. Mack-Bucher, and W. Denk, "Adaptive wavefront correction in two-photon microscopy using coherence-gated wavefront sensing," Proceedings of the National Academy of Sciences **103**, 17137–17142 (2006).

[195] D. Akbulut, T. J. Huisman, E. G. van Putten, W. L. Vos, and A. P. Mosk, "Focusing light through random photonic media by binary amplitude modulation," Opt. Express **19**, 4017–4029 (2011).

[196] D. Gabor, "A new microscopic principle," Nature **161**, 777–778 (1948).

[197] W. Lukosz, "Equivalent-lens theory of holographic imaging," JOSA **58**, 1084–1091 (1968).

[198] A. Yariv, "Phase conjugate optics and real-time holography," Quantum Electronics, IEEE Journal of **14**, 650–660 (1978).

[199] F. Charra and J. Nunzi, "Nondegenerate multiwave mixing in polydiacetylene: phase conjugation with frequency conversion," JOSA B **8**, 570–577 (1991).

[200] E. N. LEITH and J. UPATNIEKS, "Holographic imagery through diffusing media," J. Opt. Soc. Am. **56**, 523–523 (1966).

[201] M. Cui and C. Yang, "Implementation of a digital optical phase conjugation system and its application to study the robustness of turbidity suppression by phase conjugation," Opt. Express **18**, 3444–3455 (2010).

[202] I. Yamaguchi and T. Zhang, "Phase-shifting digital holography," Optics Letters **22**, 1268–1270 (1997).

[203] C.-L. Hsieh, Y. Pu, R. Grange, and D. Psaltis, "Digital phase conjugation of second harmonic radiation emitted by nanoparticles in turbid media," Opt. Express **18**, 12283–12290 (2010).

[204] C.-L. Hsieh, Y. Pu, R. Grange, G. Laporte, and D. Psaltis, "Imaging through turbid layers by scanning the phase conjugated second harmonic radiation from a nanoparticle," Opt. Express **18**, 20723–20731 (2010).

[205] R. Grange, T. Lanvin, C.-L. Hsieh, Y. Pu, and D. Psaltis, "Imaging with second-harmonic radiation probes in living tissue," Biomed. Opt. Express **2**, 2532–2539 (2011).

[206] X. Yang, C.-L. Hsieh, Y. Pu, and D. Psaltis, "Three-dimensional scanning microscopy through thin turbid media," Opt. Express **20**, 2500–2506 (2012).

[207] I. N. Papadopoulos, S. Farahi, C. Moser, and D. Psaltis, "Focusing and scanning light through a multimode optical fiber using digital phase conjugation," Opt. Express **20**, 10583–10590 (2012).

[208] F. van Beijnum, E. G. van Putten, A. Lagendijk, and A. P. Mosk, "Frequency bandwidth of light focused through turbid media," Opt. Lett. **36**, 373–375 (2011).

[209] A. Derode, A. Tourin, and M. Fink, "Random multiple scattering of ultrasound. II. Is time reversal a self-averaging process?" Phys. Rev. E **64**, 036606 (2001).

[210] C. Draeger and M. Fink, "One-Channel Time Reversal of Elastic Waves in a Chaotic 2D-Silicon Cavity," Phys. Rev. Lett. **79**, 407–410 (1997).

[211] C. Lopez, P. D. Garcia, R. Sapienza, and A. Blanco, "Photonic glass: A novel random material for light," Adv. Mater. **19**, 2597–2602 (2007).

[212] D. J. Thouless, "Maximum metallic resistance in thin wires," Phys. Rev. Lett. **39**, 1167 (1977).

[213] M. V. Berry, "Disruption of wavefronts: Statistics of dislocations in incoherent gaussian random waves," J. Phys. A **11**, 27–37 (1978).

[214] M. Sandtke, R. J. P. Engelen, H. Schoenmaker, I. Attema, H. Dekker, I. Cerjak, J. P. Korterik, F. B. Segerink, and L. Kuipers, "Novel instrument for surface plasmon polariton tracking in space and time," Review of Scientific Instruments **79**, 013704 (2008).

[215] K. O'Holleran, M. R. Dennis, and M. J. Padgett, "Topology of light's darkness," Phys. Rev. Lett. **102**, 143902 (2009).

[216] A. Weiner, D. Leaird, D. Reitze, and E. Paek, "Femtosecond spectral holography," Quantum Electronics, IEEE Journal of **28**, 2251–2261 (1992).

[217] Y. Sivan and J. B. Pendry, "Time reversal in dynamically tuned zero-gap periodic systems," Phys. Rev. Lett. **106**, 193902 (2011).

[218] M. F. Yanik and S. Fan, "Time reversal of light with linear optics and modulators," Phys. Rev. Lett. **93**, 173903 (2004).

Résumé

Cette thèse porte sur une série d'études technologiques et d'applications physiques dans les domaines de la dynamique ultrarapide et contrôle cohérent. Du point de vue technologique, nous avons effectué une étude approfondie de couplage spatio-temporel induit par l'interaction de l'onde optique avec une onde acoustique au sein d'un cristal non linéaire pour le façonnage de l'impulsion laser ultra courte. Cette étude a été menée en utilisant des techniques interférométriques. Ces effets bien connus dans les façonneurs d'impulsions utilisant une ligne 4f n'avaient jamais été mesurés dans ce type façonneur. Nos résultats ont été les premiers à les démontrer, les quantifier et les expliquer. Du point de vue du contrôle, nous avons mis en évidence des résultats très intéressants concernant la refocalisation temporelle d'une impulsion large bande fortement perturbée par un milieu multi-diffusif (i.e. l'analogue temporel de speckle spatiale). Pour cela nous avons développé une mesure résolue spatialement de la phase spectrale de l'impulsion déformée suivie par une rétroaction en boucle ouverte permettant la correction en temps réelle de la phase grâce à un façonneur d'impulsions: en raison de la linéarité du processus de diffusion, cette compensation a permis de réaliser la recompression d'une impulsion laser en sortie de l'échantillon en un point donné (localisation spatiale) . Cela a suscité beaucoup d'intérêts parmi les collègues pour diverses applications telles que l'imagerie biologique ou pour des développements utilisant l'optique quantique.

Mots clés: Impulsions femtosecondes, Mise en forme d'impulsions, Ultraviolet, Caractérisation spatio-temporelle, Impulsions à dérive de fréquence, Speckle spatio-temporel, Echantillon multi-diffusant, Couplage spatio-temporel, AOPDF, Contrôle spatio-temporel.

Abstract

This PhD thesis concerns a range of technological studies and physical applications within the fields of ultrafast science and coherent control. From the technological point of view, we have performed a comprehensive study of space-time coupling within the 'Dazzler' AOPDF pulse shaper using interferometric techniques. For a while such limitations of '4f' zero-dispersion line pulse shapers have been widely documented; our results were the first to demonstrate, quantify and explain a parallel effect in this alternative device. From a control perspective, we have demonstrated exciting results about temporal refocusing of a broadband pulse that has been strongly distorted by a random, multiply scattering medium (i.e. the temporal analogue of the spatial speckle pattern). For this purpose a spatially resolved measurement of the spectral phase of the distorted pulse followed by open-loop feedback to a pulse shaper were implemented: as a result of the linearity of the scattering process, this pre-compensation has led to a spatially localized flat output spectral phase and hence a short pulse. This has already stimulated much interest amongst colleagues for diverse applications such as biological imaging or quantum optics studies.

Key words: Femtosecond pulses, Pulse shaping, Ultraviolet, Spatio-temporal Characterization, Chirped pulses, Spatio-spectral speckle, Multiply scattering medium, Spatio-temporal coupling, AOPDF, Spatio-temporal control.